

SAFE-UP

D3.6 Vehicle demonstrator for trajectory planning and control for combined automatic emergency braking and steering manoeuvres including system for VRU detection, motion planning and trajectory control to enhance real world performance update

Primary Author(s)	Christian Löffler, Timm Gloger Robert Bosch GmbH Robin Smit TNO Carina Vogl CARIAD SE Leon Tolksdorf TH Ingolstadt Manuel Muñoz Sánchez TU Eindhoven Volker Labenski AUDI AG
Related Work Package	WP3
Version/Status	1.1 final version
Issue date	16/12/22
Deliverable type	Demonstrator
Dissemination Level	PU
Project Acronym	SAFE-UP
Project Title	proactive SAFETy systems and tools for a constantly UPgrading road environment
Project Website	www.safeup.eu
Project Coordinator	Núria Parera Applus IDIADA
Grant Agreement No.	861570



This project has received funding from the European Union's Horizon 2020 research and innovation programme under Grant Agreement 861570.

Co-Authors

Name	Organisation
Yannick Fischer	Robert Bosch GmbH
Chris van der Ploeg	TNO
Kristin Blum	CARIAD SE
Johann Stoll	CARIAD SE

Document Distribution

Version	Date	Distributed to
1.1	19.12.2022	Coordination Team
1.1	22.12.2022	Submission in the EC System
1.1	06.03.2023	Approved by the EC



Copyright statement

The work described in this document has been conducted within the SAFE-UP project. This document reflects only the views of the SAFE-UP Consortium. The European Union is not responsible for any use that may be made of the information it contains.

This document and its content are the property of the SAFE-UP Consortium. All rights relevant to this document are determined by the applicable laws. Access to this document does not grant any right or license on the document or its contents. This document or its contents are not to be used or treated in any manner inconsistent with the rights or interests of the SAFE-UP Consortium or the Partners detriment and are not to be disclosed externally without prior written consent from the SAFE-UP Partners.

Each SAFE-UP Partner may use this document in conformity with the SAFE-UP Consortium Grant Agreement provisions.



Executive summary

This Deliverable falls under the SAFE-UP Project Work Package 3 “Active safety systems for vehicle-VRU interaction” and specifically under the Task 3.4 “Advanced intervention functions to avoid critical events”. It is a purely technical document that targets to support the efficient monitoring of the technical developments for Demonstrator 3 “Vehicle demonstrator for trajectory planning and control for combined automatic emergency braking and steering maneuvers including system for VRU detection, motion planning and trajectory control to enhance real world performance”.

The present document is the second of two deliverables related to Demo 3 and focuses on the final scenario selection, the description of the development and integration of the Demo 3 algorithms and simulations of the effects of adverse weather conditions on the Demo 3 intervention strategies.

This report organizes as follows: an overview of the hardware and software architecture is presented in Section 2. Section 3 describes the scenario selection and Section 4 reports on the final state of the developed system and algorithms. Test results of individual subsystems are presented in Section 5. Section 6 presents the simulations with focus on adverse weather conditions. Conclusions of the reported research and next steps within the SAFE-UP project are given in Section 6.



Table of Contents

1.	Introduction.....	14
2.	Architecture.....	15
2.1	<i>Demonstrator hardware architecture</i>	<i>15</i>
2.2	<i>Demonstrator software architecture</i>	<i>15</i>
3.	Scenario selection.....	16
3.1	<i>Scenario selection method.....</i>	<i>17</i>
3.2	<i>Selected scenarios for Demo 3.....</i>	<i>24</i>
3.3	<i>Applicability for future scenarios for Demo 3.....</i>	<i>30</i>
4.	Demo 3 development	31
4.1	<i>Overall demonstrator scope</i>	<i>31</i>
4.2	<i>Demonstrator subsystems.....</i>	<i>32</i>
5.	Demo 3 test results	51
5.1	<i>Test results Path Planning</i>	<i>52</i>
5.2	<i>Test results VRU Intent & Trajectory Prediction</i>	<i>55</i>
5.3	<i>Test results AES Trajectory Generation</i>	<i>56</i>
6.	Simulations with focus on adverse weather conditions	61
6.1	<i>Velocity analysis for passenger car conflicts with pedestrians and cyclists.....</i>	<i>61</i>
6.2	<i>Scenario selection for simulations with focus on adverse weather conditions</i>	<i>66</i>
6.3	<i>Description of simulation setup</i>	<i>75</i>
6.4	<i>Results.....</i>	<i>79</i>
6.5	<i>Open points</i>	<i>115</i>
6.6	<i>Trajectory analysis for passenger car conflicts with pedestrians with adverse weather conditions.....</i>	<i>115</i>
7.	Conclusions and next steps	125
	References	126



List of figures

Figure 1: Demo 3 integration platform. A Bosch development vehicle featuring a radar/video sensor set and steering and braking interfaces with enhanced dynamics.....	15
Figure 2: High level interaction layouts between functionalities (light blue) and inputs needed from other work packages (grey block).....	16
Figure 3: Scenario selection methodology overview.	17
Figure 4: Visualization of parameter variations: pedestrian.	19
Figure 5: Visualization of parameter variations: bicyclist.....	20
Figure 6: Simulation assumptions for the assessment of the accident avoidance potential of an AES maneuver.	20
Figure 7: Prediction error determination.	21
Figure 8: Enlargement of VRU dimension by prediction uncertainty.	22
Figure 9: Logical view of the simulation workflow.....	22
Figure 10: selection of AES accident clusters.	24
Figure 11: General hierarchical abstraction scheme of automated vehicles adopted from (Laurène Claussmann, 2020), where the generation block contains the path and trajectory generation.....	31
Figure 12: Overview of the VRU Intent & Trajectory Prediction subsystem.....	36
Figure 13: Validation loss achieved by different architectures.....	37
Figure 14: Overview of the Trajectory Generation (inter-)dependencies.....	38
Figure 15: Schematic of the AES trajectory generation algorithm.	39
Figure 16: Structure of the inner solution part: A constrained flatness-based trajectory generator using the SSVF.....	41
Figure 17: AEB deceleration model.	44
Figure 18: Dependence of dtb and τ_b on the vehicle velocity.	45
Figure 19: Overview of the Safety Decision (inter)dependencies.	47



Figure 20: Maneuver scheduling logic of the subsystem safety decision. 47

Figure 21: The Demo 3 team on the Bosch test track. 51

Figure 22: Impressions from system testing during a Demo 3 integration workshop. 52

Figure 23: Reference path, proposed trajectories and driven path for sampling based path planner benchmark..... 53

Figure 24: Reference path, proposed trajectories and driven path for MPC based path planner benchmark..... 53

Figure 25: Variables of interest (KPIs) for the sampling based planner..... 54

Figure 26: Variables of interest (KPIs) for the MPC based planner. 54

Figure 27: FDE mean and standard deviation of predictions when using lower-fidelity object tracking (left) and high-fidelity tracking (right)..... 55

Figure 28: Example of the AES trajectory sampling by means of the simulation results..... 57

Figure 29: Planned and measured constrained state and input trajectories for a driven AES maneuver..... 59

Figure 30: P conflict scenarios definition for PC turning..... 62

Figure 31: Passenger car speed information for P-CLwoSO at TTC=2.5s..... 63

Figure 32: Pedestrian walking speed information for P-CLwoSO at TTC=2.5s..... 63

Figure 33: B conflict scenarios definition for PC moves forward and bicyclist crossing. 64

Figure 34: Passenger car speed information for B-CR at TTC=2.5s. 65

Figure 35: Bicyclist riding speed information for B-CR at TTC=2.5s..... 66

Figure 36: Selected configurations for crossing scenarios..... 67

Figure 37: Extracted velocities for the simulation based on median velocities. 68

Figure 38: Extracted velocities for the simulation focusing on the sensor range..... 68

Figure 39: Extracted velocities for the simulation focusing on the sensor opening angle. ... 69

Figure 40: Selected configurations for the longitudinal scenario..... 69



Figure 41: Resulting FoVs from the second measurement campaign, which are sensor-specific and depend on the methodology from (SAFE-UP, Deliverable report D3.5, 2022). 73

Figure 42: Decision tree for an emergency brake or an emergency steering as an intervention function. 75

Figure 43: Positioning of the sensors in the IPG vehicle. 76

Figure 44: Adapted FoVs integrated into CarMaker. 76

Figure 45: Setup how the occlusion scenarios are modelled in CarMaker. 77

Figure 46: Definition of the different width, which are required for evasive steering. 78

Figure 47: Numbers of simulated cases. 79

Figure 48: Intervention type per scenario. 80

Figure 49: Number of collisions per scenario. 80

Figure 50: Number of collisions per scenario depending on intervention type. 81

Figure 51: Number of collisions depending on rain rate (0mm/h, 16mm/h, 66mm/h, and 96mm/h)..... 81

Figure 52: CPFA – Percentage of collisions depending on detection type and rain rate. 82

Figure 53: CPFA – T_{brake} and T_{steer} depending on initial velocity V_x 83

Figure 54: CPFA – $T_{detected}$ per V_x depending on detection type and rain rate. 83

Figure 55: Detection characteristics based on detection type and velocities shown at first entry point into the FoV. 84

Figure 56: CPFA – $T_{detected}$ and $T_{intervention}$ depending on detection type and rain rate. 85

Figure 57: CPFA – Collision speed depending on detection type and rain rate. 85

Figure 58: CPFA – Break intervention – collision speed and T_{delta} depending on detection type, rain rate and V_x 86

Figure 59: CPFAO – Percentage of collisions depending on detection type and rain rate. . 87

Figure 60: CPFAO – T_{brake} and T_{steer} depending on initial velocity V_x 87



Figure 61: CPFAO – $T_{detected}$ per V_x depending on detection type and rain rate. 88

Figure 62: CPFAO – comparison $T_{detected}$ camera and radar with influencing obstruction. 89

Figure 63: CPFAO – Delta $T_{detected}$ and $T_{intervention}$ depending on detection type and rain rate. 90

Figure 64: CPFAO – Collision speed depending on detection type and rain rate. 90

Figure 65: CPFAO – Break intervention – collision speed and T_{delta} depending on detection type, rain rate and V_x 91

Figure 66: CPNA – Percentage of collisions depending on detection type and rain rate. 92

Figure 67: CPNA - T_{brake} and T_{steer} depending on initial velocity V_x 93

Figure 68: CPNA – $T_{detected}$ per V_x depending on detection type and rain rate. 93

Figure 69: CPNA - FoV entering points of targets. 94

Figure 70: CPNA – Delta $T_{detected}$ and $T_{intervention}$ depending on detection type and rain rate. 95

Figure 71: CPNA – Collision speed depending on detection type and rain rate. 96

Figure 72: CPNA – Brake intervention – collision speed and T_{delta} depending on detection type, rain rate and V_x 97

Figure 73: CPNAO – Percentage of collisions depending on detection type and rain rate. . 98

Figure 74: CPNAO – T_{brake} and T_{steer} depending on initial velocity V_x 98

Figure 75: CPNAO – $T_{detected}$ per V_x depending on detection type and rain rate. 99

Figure 76: CPNAO – comparison $T_{detected}$ camera and radar with influencing obstruction, rain rate 0mm/h. 100

Figure 77: CPNAO – Delta $T_{detected}$ and $T_{intervention}$ depending on detection type and rain rate. 101

Figure 78: CPNAO – Collision speed depending on detection type and rain rate. 102

Figure 79: CPNAO – Break intervention – collision speed and T_{delta} depending on detection type, rain rate and V_x 103



Figure 80: CPLA – Percentage of collisions depending on detection type and rain rate. .. 104

Figure 81: CPLA – T_{brake} and T_{steer} depending on initial velocity V_x 105

Figure 82: CPLA – $T_{detected}$ per V_x depending on detection type and rain rate. 105

Figure 83: CPLA – Delta $T_{detected}$ and $T_{intervention}$ depending on detection type and rain rate..... 106

Figure 84: CPLA – Collision speed depending on detection type and rain rate. 107

Figure 85: CPLA – Break intervention – collision speed and T_{delta} depending on detection type, rain rate and V_x 108

Figure 86: CPTA – Percentage of collisions depending on detection type and rain rate. .. 109

Figure 87: CPTA – T_{brake} and T_{steer} depending on initial velocity V_x and target direction. 110

Figure 88: CPTA – $T_{detected}$ per V_x depending on detection type and rain rate..... 111

Figure 89: CPTA – Delta $T_{detected}$ and $T_{intervention}$ depending on detection type and rain rate..... 111

Figure 90: CPTA – Collision speed depending on detection type and rain rate. 112

Figure 91: CPTA – Break intervention – collision speed and T_{delta} depending on detection type, rain rate and V_x 112

Figure 92: Scenario overview including rain rate, share of collisions, detection influence and causation (only additional causes in comparison to lower rain rates are given – except for *). 113

Figure 93: Conflict Scenario P-CLwoSO (SAFE-UP, Deliverable report D2.6, 2021). 116

Figure 94: Example Case for P-CLwoSO in GIDAS..... 117

Figure 95: Example Case of P-CLwoSO out of GIDAS in TRAVIS..... 118

Figure 96: All cases of P-CLwoSO out of GIDAS in TRAVIS..... 119

Figure 97: All cases of P-CLwoSO out of GIDAS in TRAVIS with Field of View (FoV) of Radar and Camera at 16 mm/h amount of rain. 120

Figure 98: Proportion of Participants in FoV for Sensor Set, Radar or Camera for Scenario P-CLwoSO from $TTC=5$ s to $TTC=0$ s..... 121



Figure 99: Detail of Passenger Car, Sensor set and Trajectories in TRAVIS..... 122

Figure 100: TTC of an accident and average minimum TTC of a maneuver..... 123

Figure 101: Distribution of average minimum TTC of a critical situation (left) and violin diagram for critical situation P-CLwoSO. 124

Figure 102: share of pedestrians in the FoV for different rain intensities and violin diagram of the min. TTC from accident variations. 124



List of tables

Table 1: Parameter variations: pedestrian.....	18
Table 2: Parameter variations: bicyclist.....	19
Table 3: relevant velocity range selection based on accidentology data.....	23
Table 4: AES accident clusters: pedestrian.....	26
Table 5: AES accident clusters: bicycle.....	26
Table 6: AES relevant and feasible accident clusters: pedestrian.....	27
Table 7: AES relevant and feasible accident clusters: bicyclist.....	28
Table 8: The dependence of trajectory generation on maneuver state.....	49
Table 9: FDE mean and standard deviation of some prediction horizons when using lower-fidelity object tracking and high-fidelity tracking.....	56
Table 10: Passenger car conflicts with pedestrians information.....	63
Table 11: Passenger car conflicts with bicyclists information.....	66
Table 12: Test matrix from EuroNCAP for Car-to-Pedestrian Scenarios (EuroNCAP, 2022).	70
Table 13: Simulated configurations, which are harmonized with EuroNCAP test cases.....	72
Table 14: Selected friction coefficients for the tested rain intensities.....	73



List of abbreviations

Abbreviation	Meaning
AEB	Autonomous emergency braking
AES	Autonomous emergency steering
B-CLwoSO	Bicyclist crossing left without sight obstruction
B-CLwSO	Bicyclist crossing left with sight obstruction
B-CRwoSO	Bicyclist crossing right without sight obstruction
B-CRwSO	Bicyclist crossing right with sight obstruction
CPFA	Car-to-Pedestrian Farside Adult
CPLA	Car-to-Pedestrian Longitudinal Adult
CPNA	Car-to-Pedestrian Nearside Adult
CPNCO	Car-to-Pedestrian Nearside Child Obstructed
CPRA	Car-to-Pedestrian Reverse Adult
CPRC	Car-to-Pedestrian Reverse Child
CPTA	Car-to-Pedestrian Turning Adult
EPS	Electronic Power Steering
ESC	Electronic Stability Control
FDE	Final Displacement Error
FoV	Field-of-View
GIDAS	German In-Depth Accident Study
GNSS	Global navigation satellite system
INS	Inertial Navigation System
KPI	Key Performance Indicator
KSI	Killed or severely injured
LSTM	Long short-term memory
MPC	Model predictive control
P	Pedestrian
PC	Passenger Car
P-CLwoSO	Pedestrian crossing left without sight obstruction
P-CLwSO	Pedestrian crossing left with sight obstruction
PCM	Pre-crash matrix



P-CRwoSO	Pedestrian crossing right without sight obstruction
P-CRwSO	Pedestrian crossing right with sight obstruction
PI	Proportional-Integral
ROS	Robot Operating System
RTK	Real time kinematics
RU	Road user
SISO	Single-Input-Single-Output
SSVF	Switched state variable filter
TTC	Time to collision
VRU	Vulnerable road user



1. Introduction

This deliverable reports on the final development status of WP3 Demo 3. The scope of Demo 3 is to develop advanced vehicle dynamics intervention functions to avoid or mitigate critical events. The demonstrator includes a vehicle with algorithms for VRU motion prediction, path and trajectory planning, estimation of risk when following a planned trajectory and trajectory control algorithms for both emergency braking and steering.

The purpose of this document is the official description of the Demo 3 final demonstrator. It is therefore working as a technical document describing the work of the system developers throughout the process, as well as the related work that will be performed in T3.6 focusing on technical verification. This final version of the deliverable consists of two main parts. The first part (Sections 2 to 5) focuses on the vehicle demonstrator and reports on the final scenario selection and the developed Demo 3 algorithms supported by qualitative test results demonstrating selected aspects of the different subsystems performance. The second part (Section 6) reports on simulations of the effects of adverse weather conditions on the Demo 3 intervention strategies. These results directly link the Demo 2 results quantifying the effects of adverse weather conditions to their impact using the Demo 3 intervention strategies.



2. Architecture

2.1 Demonstrator hardware architecture

A Bosch development vehicle as depicted in Figure 1 is used as Demo 3 integration platform. The vehicle contains several sensors and actuators with enhanced interfaces as well as a computing platform utilizing the Robot Operating System (ROS) as middleware to facilitate communication between different subsystems.

A detailed description of the Demo 3 hardware architecture and technical specification can be found in the deliverable report (SAFE-UP, Deliverable report D3.9, 2022).



Figure 1: Demo 3 integration platform. A Bosch development vehicle featuring a radar/video sensor set and steering and braking interfaces with enhanced dynamics.

2.2 Demonstrator software architecture

The software for Demo 3 consists of several functionalities developed by different partners. Figure 2 shows the high-level interactions between the functionalities developed by the partners for Demo 3. These functionalities are implemented in the ROS2 (Robot Operating System) framework, which acts as a middleware and facilitates communication between the functionalities. Within the ROS framework, the functionalities are implemented as separate executables (nodes), and these nodes communicate with each other via broadcast messaging, using a publisher-subscriber pattern.



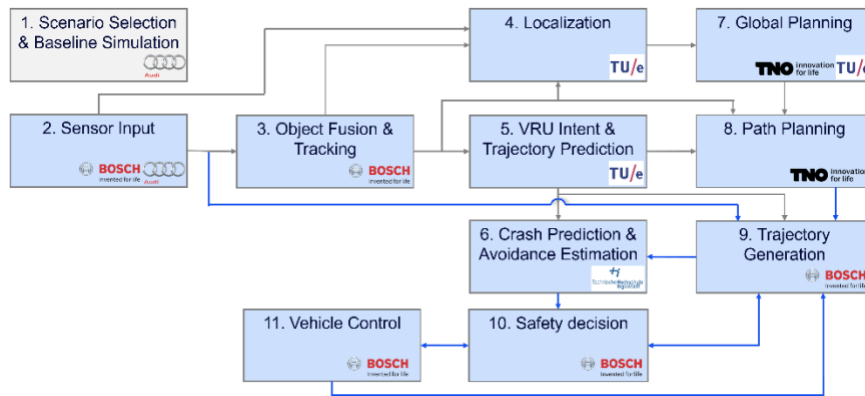


Figure 2: High level interaction layouts between functionalities (light blue) and inputs needed from other work packages (grey block).

Compared to the Demo 3 status previously reported in deliverable D3.3 (SAFE-UP, Deliverable report D3.3, 2022), only a few changes regarding the inter-node messaging have been made. These changes (highlighted in Figure 2) concerned the information needed for the generation of trajectories (by the Trajectory Generation subsystem) and selection of trajectories (by the Safety Decision subsystem).

A detailed description of the initially planned Demo 3 software architecture and the corresponding technical specifications can be found in the deliverable report (SAFE-UP, Deliverable report D3.9, 2022).

3. Scenario selection

With the main goal of developing advanced active safety systems including autonomous emergency steering (AES) as a novelty, special focus is given in understanding the potential field of effect of such a system, especially in comparison to current state-of-the-art active safety systems. Therefore, a simulative analysis to quantify a theoretical field of effect is performed.

The goal of the following Demo 3 scenario selection process is to identify scenarios that cannot be avoided by state-of-the-art active safety systems and have the theoretical potential to be avoided by AES. These scenarios are then used to steer Demo 3 development towards a real-world safety benefit by directly addressing accident types that are not yet covered by any active safety system (SAFE-UP, Deliverable report D3.3, 2022).

An initial scenario selection process based on an exemplary Pre-Crash-Matrix (PCM) accident data set (Schubert, Liers, & Petzold, 2016) solely for crossing pedestrian cases can be found in the previous version of this deliverable report (SAFE-UP, Deliverable report D3.3, 2022). The representativeness of these results is limited, as PCM cases are only a subset of the German In-Depth Accident Study (GIDAS) dataset and no further weighting was



performed. In order to extend the scenario selection process to match the overall project scope, the report at hand focuses on a holistic scenario selection process considering all relevant SAFE-UP scenario clusters identified in the deliverable report D2.6 (SAFE-UP, Deliverable report D2.6, 2021). To ensure that all potential cases are covered, a full-factorial simulation experiment serves as the basis for the scenario selection. The relevant Demo 3 scenarios are then selected based on a filtering process considering both accidentology relevance and technical feasibility.

3.1 Scenario selection method

The scenario selection method is based on a simulation of generic implementations of Autonomous Emergency Braking (AEB) and Autonomous Emergency Steering (AES) systems. Those systems are simulated and applied to vehicles involved in synthetically generated accidents derived from the Virtual Vehicle co-simulation platform (SAFE-UP, Deliverable report D5.3, 2023). Based on an assessment of the accident avoidance potential, accident clusters are formed and specified by their parameter distributions. Figure 3 shows an overview of the simulation process.

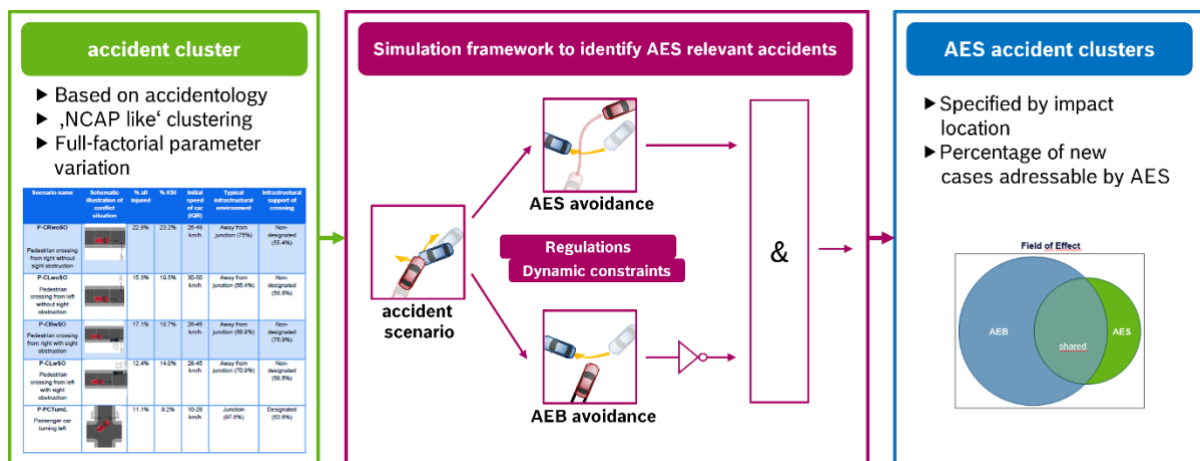


Figure 3: Scenario selection methodology overview.

Single accident scenarios are generated out of the full-factorial simulation experiment, based on the relevant accident scenarios defined in (SAFE-UP, Deliverable report D2.6, 2021). These single accident scenarios are then simulated with the application of both an AEB and an AES maneuver. The respective maneuvers are applied separately, no combined AEB/AES maneuvers are considered. A case becomes relevant for AES only when AES accident avoidance is feasible while AEB accident avoidance is impossible.

The following subchapters describe the scenario selection process more specifically in terms of the used data base and the simulation assumptions and workflow.



3.1.1 Data base

In contrast to the initial scenario selection process based on PCM accident data, the basis for the final scenario selection is given by a full-factorial simulation experiment using synthetically generated accident trajectories derived from the relevant accident scenarios defined in (SAFE-UP, Deliverable report D2.6, 2021). Here, separate parameter definitions are chosen for the pedestrian and bicyclist cases. Parameter ranges as well as object dimensions are set based on assumptions and without the usage of specific data sources. A filtering process based on a statistical analysis of the velocities derived from GIDAS is performed in a later step. For the pedestrian cases, Table 1 contains the parameter variations, leading to 68172 combinations for both frontal crashes (lateral impact location of pedestrian on ego vehicle front) and side crashes (longitudinal impact location of pedestrian on ego vehicle front). Figure 4 visualizes the parameter variations.

Table 1: Parameter variations: pedestrian.

Parameter	Range	Number of variations
Scenario type	crossing far-side, near-side	2
Initial velocity of ego vehicle	10kph – 100kph	19
Pedestrian impact velocity	2kph – 12kph	6
Lateral impact location of pedestrian on ego vehicle front	-5% – 105%	13
Longitudinal impact location of pedestrian on ego vehicle front:	-4.5% – 104.5%	13
Lateral ego vehicle position on road:	40% – 60%	5
Lane width	2.25m – 3.75m	5



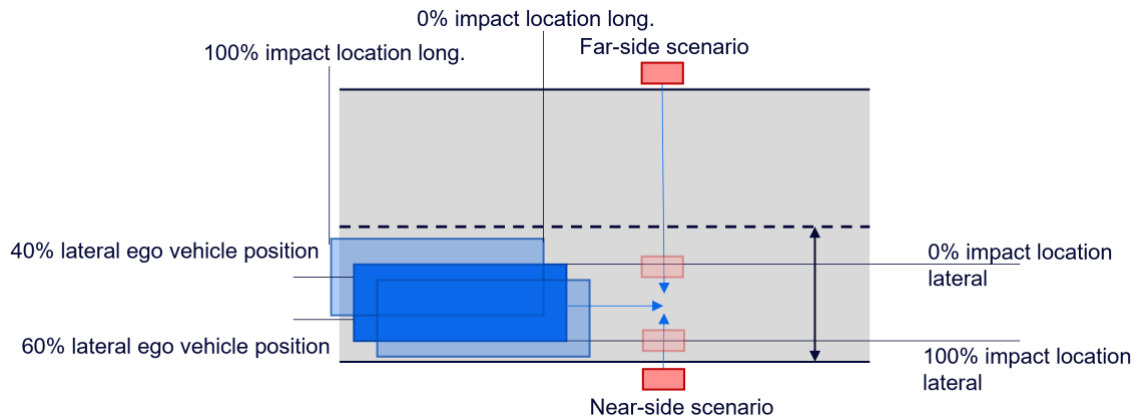


Figure 4: Visualization of parameter variations: pedestrian.

For the bicyclist cases Table 2 contains the parameter variations, leading to 367080 combinations for frontal crashes (lateral impact location of bicyclist on ego vehicle front) and 227240 combinations for side crashes (longitudinal impact location of bicyclist on ego vehicle front). Figure 5 visualizes the parameter variations.

Table 2: Parameter variations: bicyclist.

Parameter	Range	Number of variations
Scenario type	crossing far-side, near-side	2
Initial speed of ego vehicle:	10kph – 100kph	19
Bicyclist impact velocity	2kph – 40kph	20
Lateral impact location of bicyclist on ego vehicle front	-45% – 145%	21
Longitudinal impact location of bicyclist on ego vehicle front	-4.5% – 104.5%	13
Lateral ego vehicle position on road:	40% – 60%	5
Lane width	2.25m – 3.75m	5



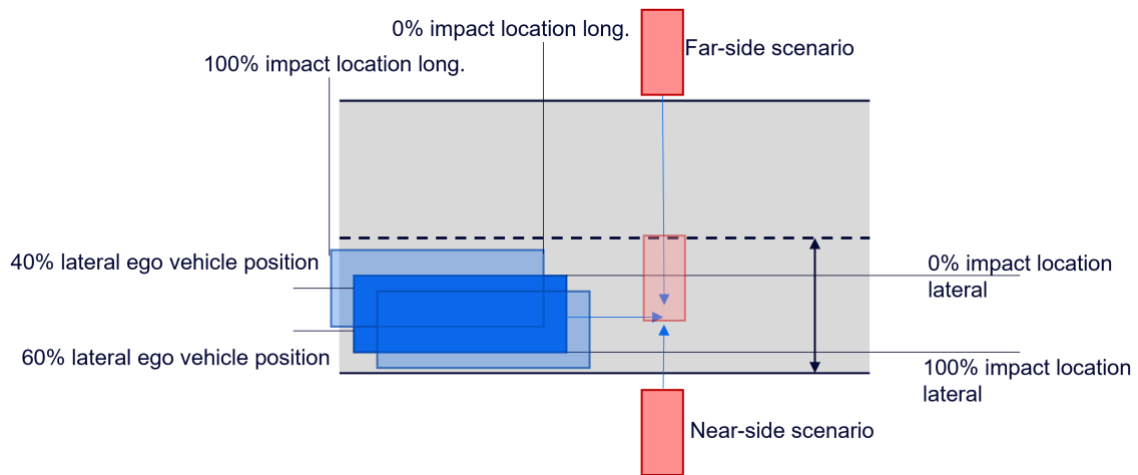


Figure 5: Visualization of parameter variations: bicyclist.

Note that impact locations of 0% refer to the VRU center hitting the ego vehicle edge, hence the negative impact location values. The minimum and maximum values for the impact location parameter refer to edge-to-edge collisions.

3.1.2 Simulation assumptions

To be able to generate useful and realistic simulation results, several assumptions must be made. A detailed description of these assumptions can be found in section 3.1.2 of the previous version of this deliverable report (SAFE-UP, Deliverable report D3.3, 2022). Figure 6 shows an overview of the general simulation assumptions.

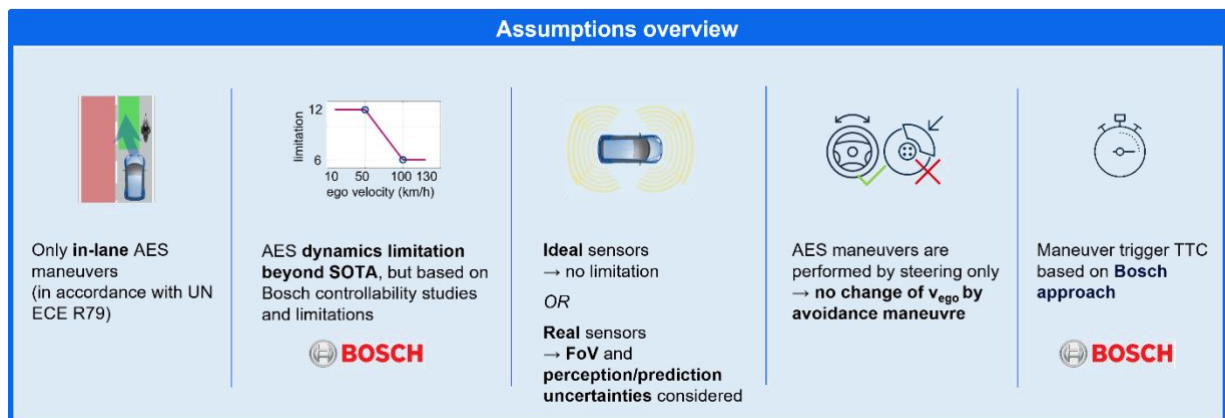


Figure 6: Simulation assumptions for the assessment of the accident avoidance potential of an AES maneuver.



In contrast to D3.3 (SAFE-UP, Deliverable report D3.3, 2022), where sensors are modeled solely by their Field-of-View (FoV), two different modeling variants are chosen in the selection process of this report.

The first variant depicts completely ideal sensors without any FoV limitation, while the second variant uses both FoV limitations and perception and prediction uncertainties derived from sensor specifications or measurements. The perception and prediction uncertainties were derived from Demo 3 vehicle measurements by comparing predictions of the dummy positions for the time t_{CP} , that are calculated at times t_0 , to ground truth data of the dummy positions at time t_{CP} from the pedestrian dummy system. The time t_{CP} is determined by the time the VRU enters a slightly enlarged driving corridor of the ego vehicle. Here, the same prediction algorithm as in the Demo 3 implementation (see 4.2.4) is used. Figure 7 visualizes the approach.

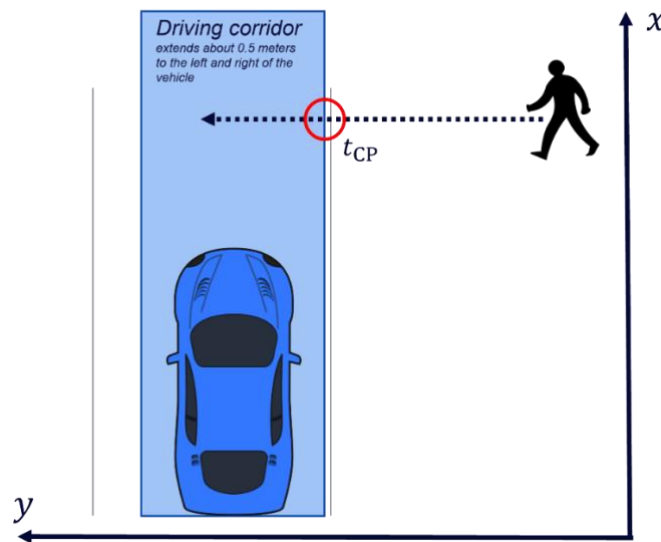


Figure 7: Prediction error determination.

For both x and y coordinates, mean errors as well as the standard deviations are determined and averaged over all measurements.

To consider these uncertainty values conservatively, the object dimensions are enlarged by two times the standard deviations σ per dimension, covering 95% of the distribution. Figure 8 shows the enlargement of the object dimensions.

Note that as all the scenarios are simulated using completely straight, right angled trajectories, this simplified assumption can be considered valid.

How the simulation results of the two variants will be used for the scenario selection process will be further elaborated in Section 3.1.4.



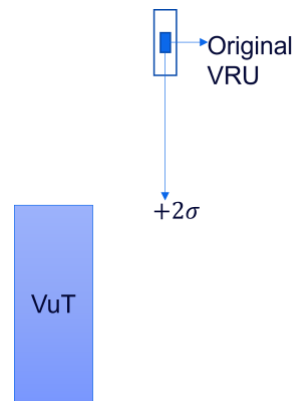


Figure 8: Enlargement of VRU dimension by prediction uncertainty.

3.1.3 Simulation workflow

The simulation workflow is depicted as a flow chart in Figure 9. Based on the trajectories and dynamics from the synthetically generated trajectories, the Time-To-Collision (TTC) and the collision overlap are calculated for each timestamp and then fed into the calculation of the system trigger. At the timestamp where TTC falls below the system trigger threshold, AES and AEB maneuvers are initiated.

For the AEB maneuver, a longitudinal acceleration profile is used to calculate the vehicle's future motion until stand-still.

For the AES maneuver, two trajectories are calculated for every accident scenario: One evading to the left and one to the right. Both trajectories end on the maximum in-lane lateral displacement possible (given by the ego lane information) and use the maximum allowed lateral dynamics.

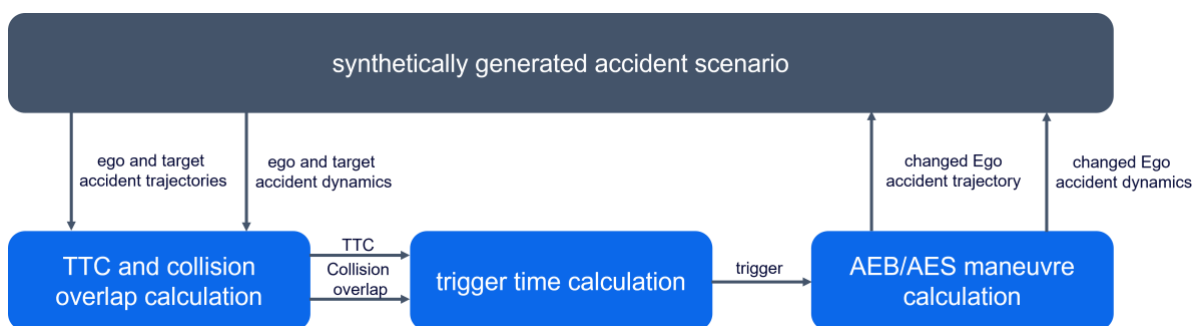


Figure 9: Logical view of the simulation workflow.

The trajectories and dynamics of the ego maneuvers are then used to perform collision checks with the pedestrian trajectory to decide if collision avoidance can be realized (SAFE-UP, Deliverable report D3.3, 2022).



3.1.4 Selection of AES accident clusters

According to the simulation assumptions described in Section 3.1.2, ideal sensors are assumed and neither Field-of-View limitations nor limitations coming from perception and prediction uncertainties are considered in the first variant. Furthermore, due to the full-factorial simulation approach, scenario relevance according to accidentology results is not considered at all. The simulation results of the first variant are therefore used to quantify the maximum possible, theoretical Field-of-Effect independently of any sensor-based limitation and for all possible combinations of scenario parameters. The corresponding results can be found in Section 3.2.1.

In a second step, both scenario relevance and AES avoidance feasibility are considered in the selection process. Therefore, the results from the second simulation variant including FoV and perception/prediction uncertainty limitations are used. Additionally, only Ego and VRU velocity ranges which show a relevance according to accident analyses are chosen for the evaluation. These velocity ranges are defined based on the following selection process:

1. Generate velocity distributions for Ego and VRU for each logical scenario described in (SAFE-UP, Deliverable report D2.6, 2021) based on GIDAS case reconstructions
2. Divide distributions into bins (5kph for the ego vehicle and bicyclist, and 1 kph for pedestrian)
3. Compute share in total cases for each bin
4. Select bins with at least 1% of the total cases. If necessary, increase range to cover at least 80% of accidents of the respective logical scenarios

The results of the velocity selection process can be found in Table 3. Note that for the P-CLwSO, P-CLwSO and P-CLwSO no data was available at the time of this analysis. The complete table can be found in (SAFE-UP, Deliverable report D5.8, 2022).

Scenario	VRU	Ego velocity [kph]	Respective case coverage	VRU velocity [kph]	Respective case coverage
P-CRwSO	Pedestrian	25-55	83%	2-10	99%
P-CLwSO		no data available – assume same range as CRwSO			
P-CRwoSO		no data available – assume same range as CRwSO			
P-CLwoSO		no data available – assume same range as CRwSO			
B-CRwSO	Bicyclist	5-60	98%	6-26	94%
B-CLwSO		5-45	93%	6-30	96%
B-CRwoSO		5-70	96%	6-30	99%
B-CLwoSO		5-55	90%	6-30	100%

Table 3: relevant velocity range selection based on accidentology data.



This second variant is therefore used for the Demo 3 AES development and testing. The results are described in Section 3.2.2.

Figure 10 shows a graphic illustration of the AES accident cluster definition process including a visualization of the Field-of-effect loss due to the consideration of both accidentology relevance and technical feasibility in terms of sensor FoV and perception/prediction uncertainty.

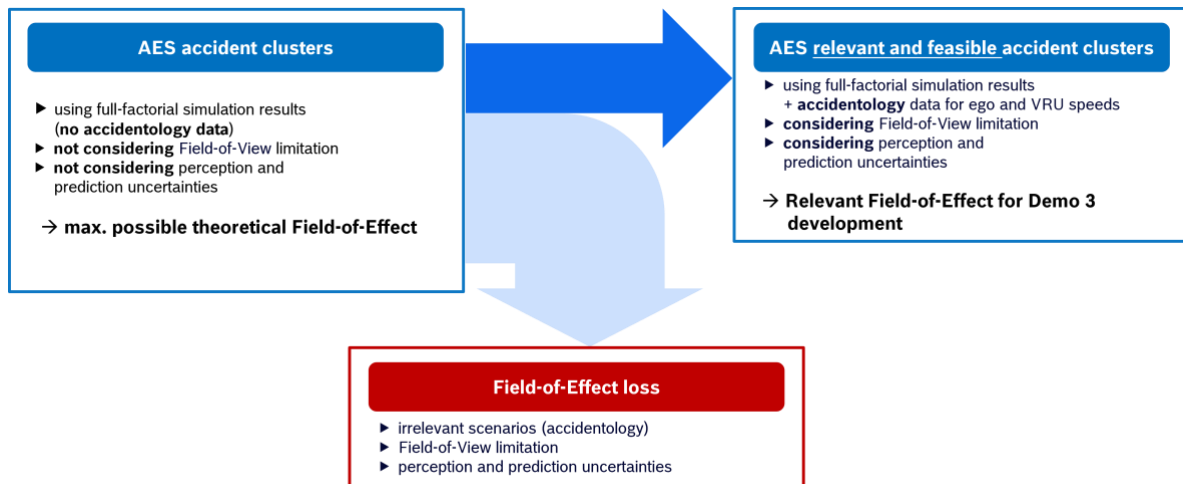


Figure 10: selection of AES accident clusters.

3.2 Selected scenarios for Demo 3

The basis for the Demo 3 scenario selection process is formed by the most relevant accidents with killed or severely injured road users (KSI) identified in (SAFE-UP, Deliverable report D2.6, 2021), which mainly are crossing pedestrian and bicyclist cases with and without sight obstruction:

- P-CRwoSO – Pedestrian crossing from right without sight obstruction
- P-CRwSO – Pedestrian crossing from right with sight obstruction
- P-CLwoSO – Pedestrian crossing from left without sight obstruction
- P-CLwSO – Pedestrian crossing from left with sight obstruction
- B-CRwoSO – Bicyclist crossing from right without sight obstruction
- B-CRwSO – Bicyclist crossing from right with sight obstruction
- B-CLwoSO – Bicyclist crossing from left without sight obstruction
- B-CLwSO – Bicyclist crossing from right with sight obstruction

For the definition of the AES accident clusters, only cases without sight obstruction are considered. For the obstruction cases, it is expected that the time for the perception algorithm to initially detect and spawn an object has a big influence on the performance. As it turned



out to be rather complex to model these effects in a way that the simulation results can be used reliably for the scenario selection, the results without obstruction serve as the basis for the obstruction cases as well. The obstruction effect will then be assessed as part of the safety benefit assessment through simulative and physical testing.

The results are clustered based on the impact location. Frontal collisions are separated into close corner and distant corner, referring to the ego vehicle's corner in relation to the direction the VRU is coming from (see pictograms in the following tables). Side crashes form the third cluster.

For each of the clusters, parameter distributions for ego and VRU velocity, lateral or longitudinal impact location (lateral for frontal impact, longitudinal for side impact) and lane width are given as boxplots showing median and 25%/75% percentiles. Additionally, the complete range of the respective parameter is shown in the top of the table cell. Furthermore, the avoidance share compared to all simulated accidents of the respective cluster is given in the last column.

For the lane width, a median value of 3.5m can be found in all of the identified clusters.

3.2.1 AES accident clusters

The present section deals with the scenario selection simulation results according to the simulation variant referring to the maximum possible, theoretical Field-of-Effect.

Table 4 and Table 5 contain the final scenarios for the pedestrian and bicyclist cases respectively. As the simulation is based on synthetically generated, straight accident trajectories, and due to the full-factorial parameter variation, simulation results for left and right cases are identical. Therefore, only results for the *crossing from right* cases are contained in the tables.

3.2.1.1 Pedestrian

For the pedestrian cases, it can be seen that for the *frontal impact, close corner* cluster, where the AES maneuver would avoid the accident by steering *into* the walking direction of the pedestrian, a significant avoidance share of 14.5% was identified. In comparison to the *frontal impact, distant corner* cluster, where the AES maneuver would avoid the accident by steering *against* the walking direction of the pedestrian, a rather low avoidance share of 5.4% was identified. For both frontal impact clusters, ego velocities are quite high with median values around 80kph, whereas pedestrian velocities are rather low with median values around 4kph. Impact locations are mostly on the edge of the ego vehicle.

The side impact cases show a quite high avoidance share of 58.8%. Ego velocities are comparable to the frontal impact cases with a slightly lower median value around 70kph, whereas pedestrian velocities are higher compared to the frontal impact cases with a median value around 6kph. Impact locations distribute around the middle of the vehicle with a slight tendency to more impacts on the front half of the vehicle.



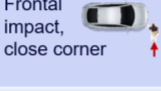
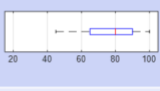
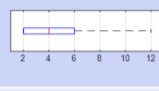


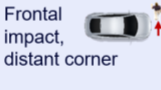
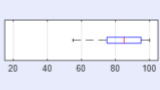


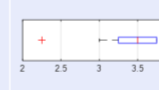
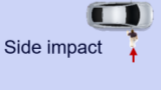
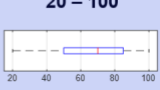
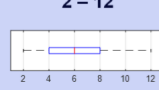
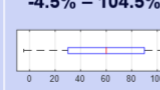
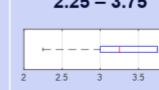
Scenario	Impact location	Ego velocity [kph]	VRU velocity [kph]	Lat./Long. crash impact location [%]	Lane width [m]	Avoidance [%]
P-CRwoSO / P-CLwoSO Pedestrian crossing from right/left without sight obstruction	Frontal impact, close corner 	45 – 100 	2 – 12 	-5% – 40% 	2.25 – 3.75 	14.5
P-CRwoSO / P-CLwoSO Pedestrian crossing from right/left without sight obstruction	Frontal impact, distant corner 	55 – 100 	2 – 6 	50% – 100% 	2.25 – 3.75 	5.4
P-CRwoSO / P-CLwoSO Pedestrian crossing from right/left without sight obstruction	Side impact 	20 – 100 	2 – 12 	-4.5% – 104.5% 	2.25 – 3.75 	58.8

Table 4: AES accident clusters: pedestrian.

3.2.1.2 Bicyclist

For the bicyclist cases, the avoidance shares for both clusters *frontal impact, close corner* cluster, where the AES maneuver would avoid the accident by steering *into* the driving direction of the cyclist, and *frontal impact, distant corner*, a neglectable avoidance share of 2.4% and 1.1% respectively was identified. For both frontal impact clusters, ego velocities are also quite high with median values around 80kph, whereas cyclist velocities are rather low with median values around 3kph. Impact locations are mostly on the edge of the ego vehicle.

The side impact cases show a higher avoidance share of 35.2%. Ego velocities are comparable to the frontal impact cases with a slightly lower median value around 70kph, whereas cyclist velocities are higher compared to the frontal impact cases with a median value around 12kph. Impact locations mainly distribute around the front half of the vehicle.

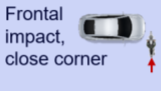
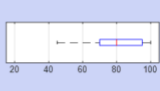
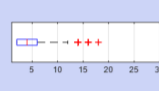
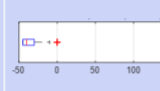

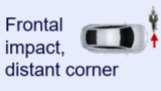
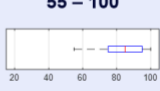

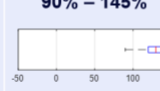

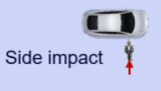
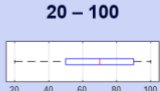
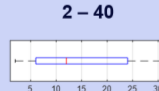
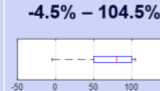
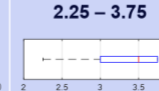
Scenario	Impact location	Ego velocity [kph]	VRU velocity [kph]	Lat./Long. crash impact location [%]	Lane width [m]	Avoidance [%]
B-CRwoSO / B-CLwoSO Bicyclist crossing from right/left without sight obstruction	Frontal impact, close corner 	45 – 100 	2 – 18 	-45% – 0% 	2.25 – 3.75 	2.4
B-CRwoSO / B-CLwoSO Bicyclist crossing from right/left without sight obstruction	Frontal impact, distant corner 	55 – 100 	2 – 6 	90% – 145% 	2.25 – 3.75 	1.1
B-CRwoSO / B-CLwoSO Bicyclist crossing from right/left without sight obstruction	Side impact 	20 – 100 	2 – 40 	-4.5% – 104.5% 	2.25 – 3.75 	35.2

Table 5: AES accident clusters: bicycle.



3.2.2 AES relevant and feasible accident clusters

The present section deals with the scenario selection simulation results according to the simulation variant referring to the relevant Field-of-Effect for the Demo 3 AES development and testing. This includes a filtering for both accidentology relevance in terms of ego and VRU velocities as well as technical feasibility in terms of sensor FoV and perception and prediction uncertainties.

Table 6 and Table 7 contain the final scenarios for the pedestrian and bicyclist cases respectively. As different velocities for the bicyclist crossing from left and right are relevant according to accident analyses, the clusters are not identical, in contrast to the pedestrian cases and all cases from Section 3.2.1.

3.2.2.1 Pedestrian

For the pedestrian cases, the avoidance shares for both clusters *frontal impact, close corner* cluster, where the AES maneuver would avoid the accident by steering *into* the walking direction of the pedestrian, and *frontal impact, distant corner*, an avoidance share of 3.7% respectively was identified. For both frontal impact clusters, ego velocities are close to the maximum values given by accidentology with median values around 50kph, whereas pedestrian velocities are rather low with median values around 2kph. Impact locations are mostly on the edge of the ego vehicle.

The side impact cases show a still quite high avoidance share of 37.7%. Ego velocities are comparable to the frontal impact cases, whereas pedestrian velocities are higher compared to the frontal impact cases with a median value around 4kph. Impact locations mainly distribute around the front half of the vehicle.


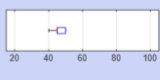
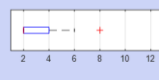



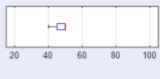
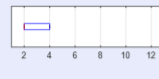

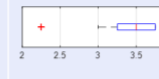



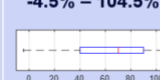

Scenario	Impact location	Ego velocity [kph]	VRU velocity [kph]	Lat./Long. crash impact location [%]	Lane width [m]	Avoidance [%]
P-CRwoSO / P-CLwoSO Pedestrian crossing from right/left without sight obstruction	Frontal impact, close corner 	40 – 50 	2 – 8 	-5% – 0% 	3 – 3.75 	3.7
P-CRwoSO / P-CLwoSO Pedestrian crossing from right/left without sight obstruction	Frontal impact, distant corner 	40 – 50 	2 – 4 	90% – 105% 	2.25 – 3.75 	3.7
P-CRwoSO / P-CLwoSO Pedestrian crossing from right/left without sight obstruction	Side impact 	30 – 50 	2 – 10 	-4.5% – 104.5% 	2.25 – 3.75 	37.7

Table 6: AES relevant and feasible accident clusters: pedestrian.



3.2.2.2 Bicyclist

For the bicyclist cases crossing from right, the avoidance shares for the *frontal impact, close corner* cluster, where the AES maneuver would avoid the accident by steering *into* the walking direction of the pedestrian, a neglectable avoidance share of 0.6% was identified, whereas the avoidance share of the *frontal impact, distant corner* cluster disappears completely. The ego velocities remain quite high with a median value of 70kph, whereas cyclist velocities are rather low with a median value of 2kph. Impact locations are mostly on the edge of the ego vehicle.

The side impact cases show a higher avoidance share of 35.2%. Ego velocities are comparable to the frontal impact cases with a slightly lower median value around 70kph, whereas cyclist velocities are higher compared to the frontal impact cases with a median value around 12kph. Impact locations mainly distribute around the front half of the vehicle.

For the bicyclist cases crossing from left, the avoidance shares for both the *frontal impact, close corner* cluster and the *frontal impact, distant corner* cluster disappear completely.

The side impact cases show a remaining avoidance share of 10.6%. Ego velocities are lower compared to the frontal impact cases with a median value of 45kph, whereas cyclist velocities are slightly lower compared to the frontal impact cases with a median value of 10kph. Impact locations also mainly distribute around the front half of the vehicle.

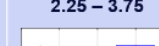
Scenario	Impact location	Ego velocity [kph]	VRU velocity [kph]	Lat./Long. crash impact location [%]	Lane width [m]	Avoidance [%]
B-CRwoSO Bicyclist crossing from right without sight obstruction	Frontal impact, close corner 	45 – 70 	6 – 12 	-45% – -20% 	3 – 3.75 	0.6
B-CRwoSO Bicyclist crossing from right without sight obstruction	Frontal impact, distant corner 					0
B-CRwoSO Bicyclist crossing from right without sight obstruction	Side impact 	25 – 70 	6 – 30 	-4.5% – 104.5% 	2.25 – 3.75 	20.8
B-CLwoSO Bicyclist crossing from left without sight obstruction	Frontal impact, close corner 					0
B-CLwoSO Bicyclist crossing from left without sight obstruction	Frontal impact, distant corner 					0
B-CLwoSO Bicyclist crossing from left without sight obstruction	Side impact 	25 – 50 	6 – 30 	-4.5% – 104.5% 	2.25 – 3.75 	10.6

Table 7: AES relevant and feasible accident clusters: bicyclist.



3.2.3 Summary and Discussion

In this analysis, scenarios are considered as AES scenarios if accident avoidance using AEB is impossible and accident avoidance using AES is possible. Accident avoidance is identified using a simulation study based on synthetically generated accident trajectories with full-factorial parameter variations. Only cases without sight obstruction were considered. The scenario selection process was split into two different approaches, forming two relevant AES accident cluster groups:

1. *AES accident clusters*: maximum possible, theoretical Field-of-Effect independently of any sensor-based limitation and for all possible combinations of scenario parameters.
2. *AES relevant and feasible accident clusters*: the relevant Field-of-Effect for the Demo 3 AES development including both accidentology relevance in terms of ego and VRU velocities as well as technical feasibility in terms of sensor FoV and perception and prediction uncertainties.

The AES accident clusters were further split into three impact location clusters:

1. Frontal impact, close corner
2. Frontal impact, distant corner
3. Side impact

The results show limited avoidance shares for the pedestrian cases with frontal impact location and a quite big avoidance share for the side impact cases. For the bicyclist cases, avoidance shares for the frontal impacts can be neglected, whereas the side impact cases show a significant avoidance share.

All frontal impact clusters show impact locations distributing narrowly around the edge of the ego vehicle. The side impact clusters show impact locations mainly distributing around the front half of the ego vehicle.

Ego velocities always distribute to the maximum value, as AES avoidance potential, especially compared to AEB avoidance potential increases with higher velocities. The inverse effect occurs for the VRU velocities, where the AES avoidance potential increases with lower VRU velocities, as less lateral displacement is required for complete accident avoidance.

The *AES relevant and feasible accident clusters* serve as the basis for the physical testing case selection, which will be described in (SAFE-UP, Deliverable report D5.3, 2023).



3.3 Applicability for future scenarios for Demo 3

The general method of scenario selection can be applied on any other data base or scenario set. So, when definitions of future accident scenarios become available, the scenarios that could be addressed by Demo 3 can be extended.



4. Demo 3 development

4.1 Overall demonstrator scope

This final Demo 3 deliverable report focuses on the final implementation of all Demo 3 subsystems, including a more detailed explanation of the developed algorithms as well as the specific increments compared to the initial development reported in (SAFE-UP, Deliverable report D3.3, 2022). The general layout of the software is shown in Figure 2.

System integration and functional verification of the whole architecture was done using the scenarios described in Section 3.2.

The Demo 3 AES function is aligned with the UNECE regulation R79 ESF (UNECE, 2018). Therefore, the usable evasion space is limited to the current lane, i.e. only in-lane maneuvers are performed. This contrasts with currently available driver-initiated evasive steering support systems, where the driver may initiate a maneuver exceeding the current lane.

Preliminaries:

The terminology used within this report can have in literature slightly different interpretations. To avoid confusion, this paragraph defines the terminology and ontology used in this chapter, which is an extension on the review article of (Laurène Clausmann, 2020) where widely accepted terminologies are explained.

In a general hierarchical scheme of automated vehicles (see Figure 11) once the high-level route and decision are known, the motion strategy includes generating and selecting a *path* and a *trajectory*.

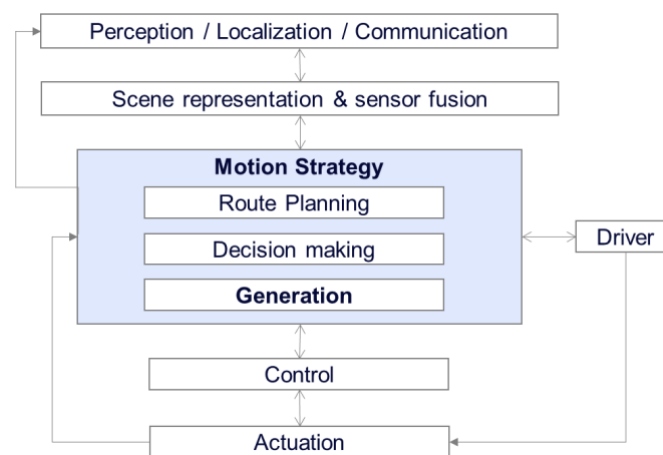


Figure 11: General hierarchical abstraction scheme of automated vehicles adopted from (Laurène Clausmann, 2020), where the generation block contains the path and trajectory generation.



Path here refers to the sequence of space-related states in the free space (also referred to as geometric waypoints) and *trajectory* refers to the sequence of spatiotemporal states in the free space (also referred to as time-varying waypoints).

Furthermore, *maneuvers* refer to a predefined motion considered as a subspace of paths or trajectories, i.e. motion and actions or tasks refer to symbolic operations of maneuvers or intentions of road users.

4.2 Demonstrator subsystems

A general overview of the demonstrator subsystems is given in Figure 2. Detailed descriptions for each subsystem can be found in the following subsections with focus on the increments compared to the initial development reported in (SAFE-UP, Deliverable report D3.3, 2022). Subsystems where no additional development was necessary are not listed in this report.

4.2.1 Subsystem Localization

As localization is merely an enabling technology for the Demo 3 developments, validation and demonstration, the vehicle is equipped with a high end GNSS-RTK sensor. This sensor outputs high frequent and accurate GNSS data, which is fused with IMU data. Position and heading of the vehicle is transformed into a world-fixed Cartesian coordinate frame.

4.2.2 Subsystem Global Planning

The Global Planning subsystem is described in (SAFE-UP, Deliverable report D3.3, 2022). It provides global goal points for the Path Planning subsystem. Goal points can be extracted from a stored map (e.g. in Opendrive format), calculated along a pre-recorded GNSS trace or calculated along the center of the current lane of the vehicle. In the Demo 3 tests, the goal points are provided along the vehicle lane's center due to the unavailability of a map and GNSS trace.

4.2.3 Subsystem Path Planning

The path planning module is responsible for the generation of a path that serves as a reference line for the trajectory generation modules. It defines the intended behavior of the vehicle, e.g. lane following, lane change etc.

TNO has developed two separate versions of the Path Planning module in parallel, a sampling-based planner and a Model-Predictive-Control (MPC) based planner. The first version of these planners is described in (SAFE-UP, Deliverable report D3.3, 2022). In this section, the updates with respect to the first version of these planners will be described.



4.2.3.1 Sampling based planner

In D3.3 (SAFE-UP, Deliverable report D3.3, 2022), a first version of the sampling based planner is described. This planner utilizes the *SST* algorithm introduced in (Y. Li, 2014) in a dynamic motion planning framework. The planner creates a state space search tree by iteratively sampling piecewise constant control inputs, more specifically acceleration and steering angle, and propagating the vehicles states based on a kinematic bicycle system model. Propagated states are checked for validity based on drivable space, defined by the road geometry, collision with the predicted position of other road users (VRU, vehicles) and vehicle dynamic limitations (steering angle, acceleration, legal speed limit). Feasible states are awarded a certain penalty or cost, based on the desired speed, the path length, deviation from lane center and distance to the predicted position of other targets, where the last cost is calculated by drawing an artificial potential function around the predicted target position. The planner is designed as an *anytime* planner, meaning that it is allowed to run for a fixed amount of time and return the most optimal solution (i.e. lowest accumulative motion cost), if any.

Several updates are created based on this initial version. Based on initial performance tests in simulation and on the TNO demonstrator platform, the planner showed slow converge to high quality trajectories, i.e. a long planning time was required to achieve safe and comfortable trajectories. This is due to the unbiased exploration of the state space; all parts of the surrounding space of the vehicle is explored equally without any bias towards favorable areas, such as lane(s) (centers) or along previous calculated trajectories. In order to allow for faster convergence to high quality trajectories, two exploration branches are added to the state space search tree, before running the planner in the *anytime* fashion.

The first exploration branch, starting at the tree root (i.e. the current state of the vehicle), attempts to steer the vehicle towards the closest lane center. This exploration branch is created by firstly picking a point on the closest lane center at a fixed distance away from the current vehicle position. Then, for a fixed number of iterations, inputs are sampled and applied to the current state to achieve a new state sample. After these iterations, the state sample closest to the lane center in terms of Euclidean distance is selected and saved, together with the corresponding control inputs. The initial state is set to the newly selected state and the process is iterated until the goal (space) is reached, no valid state can be found anymore or the distance from tree root to final state exceeds a parametrizable threshold.

The second exploration branch is created from the trajectory calculated in the previous iteration, provided that the starting state is sufficiently close to a given state on the (interpolated) previous solution. First, from all states in the previous trajectory, the one closest to the starting state is selected in terms of 2-norm. If this state is sufficiently close to the starting state, all states from the previous trajectory following this selected state are iteratively checked for validity and added to this exploration branch.

A simulation study has shown that adding these exploration branches to the initial search tree results in a performance gain of amongst others 97% in terms of deviation from desired velocity and 82.7% in terms of deviation from the lane center.

A full description of the sampling based planner can be found in (R. Smit, 2022).



4.2.3.2 MPC based planner

In D3.3 (SAFE-UP, Deliverable report D3.3, 2022), a first version of the MPC-based path-planner is introduced. This planner employs a model-predictive algorithm, i.e., using model-knowledge to predict a future horizon of the vehicle's trajectory, and finding an input which optimizes this trajectory to satisfy an optimal cost (note, that this cost may be different than the cost function of the SST-based planner). This running cost is divided into several design criteria, i.e., progress towards a goal, comfort and risk. In terms of comfort, the running cost primarily focuses on the minimization of the energy of the inputs which drive the trajectory state, i.e., the steering angle and the acceleration of the vehicle. The algorithm is designed to be a standalone planner which, without pre-defined trajectories, can plan a path towards a common goal from the global planner, without using any intermediate milestones, apart from the description of the infrastructure (i.e., a description of the road). Minimization of risk is done by modeling the infrastructure, dynamic objects and static objects as artificial potential fields, or risk fields. By giving these field appropriate sizes and amplitudes, the vehicle is tempted to avoid these “repulsive” fields and, hence, minimize the risk.

During internal testing campaigns at TNO, several problems and shortcomings have been identified, which have been incorporated into the design of the updated model-predictive planner. First, to better align with the Trajectory Generation module, the initial condition of a planning problem starts at the nearest point of the previously optimized path. Due to the high degree of non-linearity of the model-predictive program, the program is prone to get stuck in local optima (i.e., the best solution to the problem within a small neighborhood of possible solutions.). A way to reduce (but not fully neglect) the effect of this phenomenon is by programming the MPC in a different manner. Throughout the development phase, the MPC has been programmed in Matlab and C++ using a direct single shooting method. Direct, meaning that first the model is discretized, and subsequently the optimization problem is solved. Single shooting methods suffer from the issue that, even when the differential equations of the system are stable and well-conditioned, the resulting boundary-value problem may be unstable and ill-conditioned. As a result, while sacrificing little more computational effort, the model-predictive program has been rewritten into a direct multiple-shooting problem.

Another issue that has been found during our testing campaign is the issue when using long-horizon paths with relatively large sampling times. In these cases, it could happen that a potential field can fully lie in between two sampling periods, and hence the running cost is unaffected by the effect of this potential field. To mitigate this issue, we have introduced a novel subsampling method, which linearly interpolates between two sampling periods and assigns a cost to each of these interpolated points. These new interpolated terms are added to the cost function. However, since these interpolated terms are an affine combination of previously declared optimization variables, the computational time is barely affected.

A full description of the MPC based planner can be found in (C. van der Ploeg, 2022).



4.2.3.3 Planner modification for Demo 3 integration

In order to be able to integrate the Path Planning module(s) with the other subsystems described in this chapter in the scope of Demo 3, some final modifications are made to both planners. First, one should note that, even though the planners output a *trajectory* (position, heading and velocity, mapped in time), only the *path* (position, heading) part is used by the other subsystems.

Furthermore, in order to integrate the path planner with the trajectory generator as described in Section 4.2.3, each planning query starts from a specific point of the previously found path, instead of from the current vehicle position.

Finally, the software is transformed to be compatible with the ROS2 middleware, instead of the ROS1 software used for TNO internal developments.

4.2.4 Subsystem VRU Intent & Trajectory Prediction

TU Eindhoven has developed a hybrid physics- and pattern-based trajectory prediction model for different road users, with the main focus being pedestrians. The first version of the trajectory prediction model is described in deliverable D3.3 (SAFE-UP, Deliverable report D3.3, 2022).

Several aspects have been updated with respect to the first version, which are described below. The most notable updates are a thorough optimization of the model's architecture and modifications to the data processing pipeline that prepares the inputs to the model in order to increase robustness towards lower-fidelity perception data. Additionally, the dataset used for the development and evaluation of the model was replaced for Argoverse2 (Wilson, et al., 2021), which, as opposed to the previously used dataset, does not have any legal limitations for using it to train models for an experimental setting. The overall hybrid architecture and updates are described below.

4.2.4.1 Model architecture

State of the art trajectory prediction models are often developed and evaluated on large driving datasets that are publicly available for this task (Muñoz Sánchez, Elfring, Silvas, & van de Molengraft, 2022). These datasets are collected with a vehicle equipped with a sensor suite capable of providing high fidelity perception data, and performance of pattern-based models (assuming reliable data is available at all times) drops drastically when deployed on vehicles with more common lower-fidelity sensor suites. To overcome this challenge, the final model architecture has been implemented as overviewed in Figure 12.



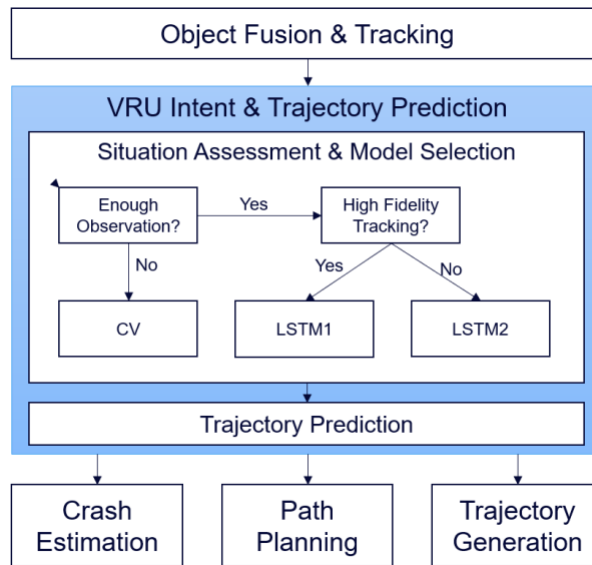


Figure 12: Overview of the VRU Intent & Trajectory Prediction subsystem.

A first assessment is done to determine if sufficient information of the VRU is available for the implemented pattern-based model. If there is not, a constant velocity (CV) model is used, which despite its simplicity has been shown to provide competitive results since it describes well average walking behavior (Schöller, Aravantinos, Lay, & Knoll, 2020). Next, depending on the expected fidelity of the object fusion & tracking data, one of two LSTM Autoencoder variants are used. The first is developed following standard practices in the trajectory prediction scientific community, and the second is a modified version to increase robustness towards unreliable inputs. The base architecture of both LSTMs is as described in (SAFE-UP, Deliverable report D3.3, 2022), and an optimal number of layers and neurons is achieved as described next.

4.2.4.2 Architecture optimization

To find an optimal configuration for the selected model, a grid search is performed in a subset of all training data varying model parameters such as the number of layers and number neurons in each layer of the LSTM's encoder and decoder. For each parameter variation two metrics are reported. First, the Huber loss (Huber, 1964) achieved on the validation set. This loss was chosen over the standard squared error to mitigate the effect of outliers.

Figure 13 overviews the results of the architecture optimization process for the pedestrian prediction models. The 5 architectures that achieved the lowest loss are highlighted in yellow, and the one that achieved the lowest loss in green.



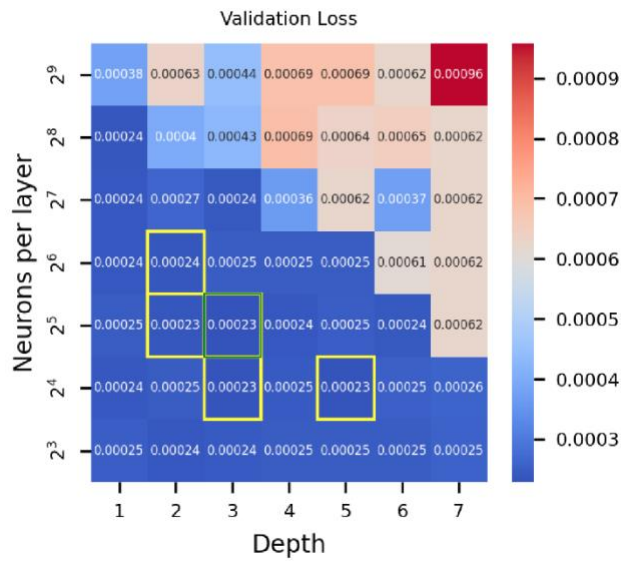


Figure 13: Validation loss achieved by different architectures.

Since it is crucial that the model is capable of running real-time, and lower runtime is always preferred, if several architectures achieve similar performance, the model with lower number of layers and neurons is preferred. Thus, the selected model has 2 hidden layers in the encoder and decoder, and 2⁶ neurons each. The same approach is followed for different road users such as cyclists.

4.2.4.3 Increasing robustness towards unreliable inputs

In the development of state-of-the-art machine learning prediction models, it is common practice to perform certain modifications to their inputs before prediction instead of operating directly with the output of the object tracking module, as this presents several benefits such as lower training times and reduced model complexity. This process typically consists of 3 steps:

1. Transformation of all object observations to an egocentric view with respect to the last RU observation.
2. Rotation of the scene such that the RU is always facing the same direction. In this case, the positive x axis.
3. Data normalization. Several normalization approaches exist. In this work one of the most common practices is used: scaling every feature to a common range. In this case [-1, 1].

After predictions are made, the predictions are transformed to the corresponding original frame applying the same operations in reverse.

This data processing pipeline assumes a certain degree of accuracy on the tracked object's positions and headings to perform the required transformations. After preliminary tests in the



vehicle, it was observed this accuracy is not always guaranteed, resulting in severely lacking predictions compared to the performance achieved on common (offline) benchmarks. Example of these deficiencies are sensor noise, delay and bias. Hence, for future research, the training data would have to be further pre-processed to well represent the noise and inaccuracies that a certain sensor set would exhibit.

To mitigate this problem, the pre-processing pipeline is updated to artificially simulate the detected in-vehicle inaccuracies during the training phase, and rotation of the scene (step number 2 above) is avoided, as inaccuracies in the RU's detected heading can severely deteriorate the predictions.

4.2.5 Subsystem Trajectory Generation

Bosch has developed the Trajectory Generation subsystem, which is responsible for the computation of vehicle trajectories (spatiotemporal information about the vehicles future motion) on the basis of the information provided by the Path Planning and VRU Intent & Trajectory Prediction subsystems as well as vehicle state and environmental information provided by the Sensor and Vehicle Control subsystems. Vehicle trajectories are evaluated regarding a risk estimation associated with their potential realization by the Crash Prediction & Avoidance Estimation subsystem and handed over to the Safety Decision subsystem (see Figure 14, only relevant links included). The Trajectory Generation subsystem constitutes of three subsystems of its own: *Nominal driving trajectory generation*, *AEB trajectory generation* and *AES trajectory generation*.

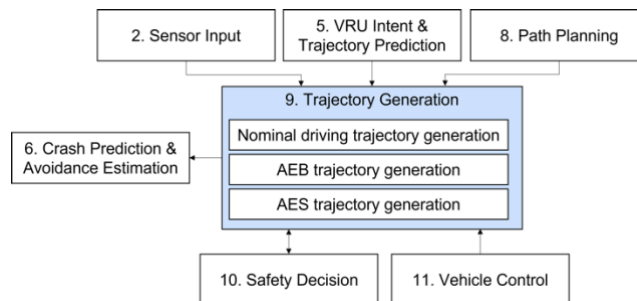


Figure 14: Overview of the Trajectory Generation (inter-)dependencies.

The first version of the developed trajectory generators has been introduced in (SAFE-UP, Deliverable report D3.3, 2022) as a top level description. This section therefore focuses on a more detailed explanation of the used approaches as well as on the increments compared to the development status reported in (SAFE-UP, Deliverable report D3.3, 2022).

4.2.5.1 AES trajectory generation

The *AES trajectory generation* subsystem implemented in the demonstrator is based on the trajectory planning approach presented in (Löffler, Gloger, & Joos, to be published). It constitutes a sampling-based trajectory generation algorithm with its basic structure shown in Figure 15. The algorithm, depicted as the green box, acts on the parametrization (sampled



from intervals of maneuver trigger times T_{trig} and possible lateral displacements Y_L) of a constrained flatness-based trajectory generator, depicted as the embedded blue box, to calculate sets of evasive emergency trajectories. During runtime full maneuver trajectories for each sampled parametrization are calculated by the underlying trajectory generator, where, due to the model-based nature of the trajectory generator, the calculation of each trajectory directly yields the full modeled time evolution of all vehicle states $\underline{x}^*(t)$ as well as the corresponding control input $\underline{\delta}^*(t)$. As the trajectory generator operates in a Frenet frame (Kühnel & Hunt, 2006) of the path provided by the Path Planning subsystem (for details see below), these trajectories are transformed into a global frame of reference prior to further processing by other subsystems by the transformation \mathcal{F} . The sets $\{(\underline{x}^*(t), \underline{\delta}^*(t))\}$ of trajectories (the underline notation is used in this report to indicate representations in the global frame) are the outputs of the subsystem to the Crash Prediction & Avoidance Estimation (see Section 4.2.6) and Safety Decision (see Section 4.2.6) subsystems.

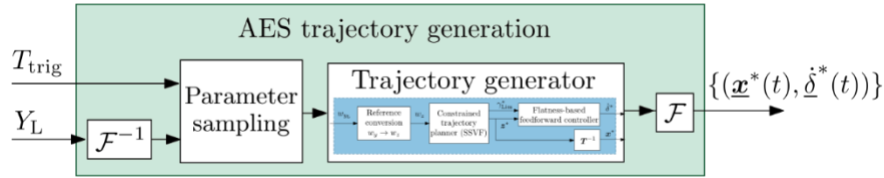


Figure 15: Schematic of the AES trajectory generation algorithm.

The overall algorithm is capable of performing a cyclic trajectory replanning during an AES maneuver in order to adapt the actually driven vehicle trajectory to environmental changes, such as e.g. changes of an obstacle's motion, and significant deviations of the planned from the actual vehicle state that cannot be sufficiently compensated by the Vehicle Control subsystem, as e.g. road bumps substantially influencing the steering angle.

In the following a brief description of the algorithm's concepts is given. In order to consider the vehicle dynamics, the extended single track model

$$\dot{\mathbf{x}} = \mathbf{A} \mathbf{x} + \mathbf{b} u$$

$$= \begin{bmatrix} \frac{-c_{\alpha,v} - c_{\alpha,h}}{m v} & -1 - \frac{c_{\alpha,v} l_v - c_{\alpha,h} l_h}{m v^2} & 0 & 0 & \frac{c_{\alpha,v}}{m v} \\ c_{\alpha,h} l_h - c_{\alpha,v} l_v & \frac{-c_{\alpha,v} l_v^2 - c_{\alpha,h} l_h^2}{\theta v} & 0 & 0 & \frac{c_{\alpha,v} l_v}{\theta} \\ 0 & 1 & 0 & 0 & 0 \\ v & 0 & v & 0 & 0 \\ 0 & 0 & 0 & 0 & 0 \end{bmatrix} \mathbf{x} \quad (1a)$$

$$+ [0, 0, 0, 0, 1]^T \dot{\delta}$$

$$\mathbf{y} = \mathbf{c}^T \mathbf{x} = [0, 0, 0, 1, 0] [\beta, \dot{\psi}, \psi, y_L, \delta]^T \quad (1b)$$

with $\mathbf{x}(0) = \mathbf{x}_0$ is introduced in state-space-representation. It consists of a standard single track model (Schramm, Hiller, & Bardini, 2018), an input rate model by means of a single integrator, and of the lateral displacement y_L , which represents the system output y . Note that the model extension by y_L uses a small-angle approximation of the slip and yaw angle in



order to linearize the system. In this controllable, time-invariant Single-Input-Single-Output (SISO) system of order $n = 5$, the system state x is composed of the slip angle β , the yaw rate $\dot{\psi}$, the yaw angle ψ , the steering angle δ , which represents the physical control input to the vehicle, and y_L . The model control input u is given by the steering angle gradient $\dot{\delta}$, such that a smooth and viable steering angle is ensured.

Due to (1) being a SISO system, trajectory planning can only be realized for a single reference state. As a consequence, the AES trajectories only describe the vehicles relative lateral motion in a Frenet frame of a reference curve (Kühnel & Hunt, 2006). This reference curve represents the intended path of the vehicle irrespective of the emergency situation, e.g. it follows the lane center, and is handed over from the Path Planning subsystem.

For AES to be realized as a SAE L2 system according to (SAE, 2018), trajectory dynamics have to be limited in such a way that every driver can still control the vehicle at any time. The yaw rate has been identified as the vehicle-independent dynamics parameter, that correlates the most with the human ability to control a driving maneuver (Neukum & Krüger, 2003), (Neukum, Paulig, Frömmig, & Henze, 2010). Therefore, constraints of the maximum yaw rate

$$\dot{\psi}_{\ominus} \leq \dot{\psi} \leq \dot{\psi}_{\oplus} \quad (2a)$$

are utilized in this work as a safety measure to ensure the controllability of AES maneuvers.

Further, the vehicle actuator limits are considered by means of additional state and input constraints

$$\dot{\delta}_{\ominus} \leq \dot{\delta} \leq \dot{\delta}_{\oplus} \quad (2b)$$

$$\delta_{\ominus} \leq \delta \leq \delta_{\oplus} \quad (2c)$$

In order to generate the constrained AES trajectories, the structural property of differential flatness (Fliess, Lévine, Martin, & Rouchon, 1995) is exploited. It states that all relevant quantities such as the states x , the control input u , as well as the output y can be expressed by means of a flat output z and its time derivatives $\dot{z}, \ddot{z}, \dots, z^{(n)}$. As a result, the plant (1) is obtained in the controllable canonical form

$$\begin{aligned} \dot{z} &= \mathbf{A}_R z + \mathbf{b}_R u \\ &= \begin{bmatrix} 0 & 1 & 0 & 0 & 0 \\ 0 & 0 & 1 & 0 & 0 \\ 0 & 0 & 0 & 1 & 0 \\ 0 & 0 & 0 & 0 & 1 \\ 0 & 0 & 0 & -a_3 & -a_4 \end{bmatrix} z + \begin{bmatrix} 0 \\ 0 \\ 0 \\ 0 \\ 1 \end{bmatrix} u \end{aligned} \quad (3a)$$

$$y = \mathbf{c}_R^T z = [c_{R,1}, c_{R,2}, c_{R,3}, 0, 0] z \quad (3b)$$

The inner layer of the constrained trajectory generator is depicted in Figure 16.



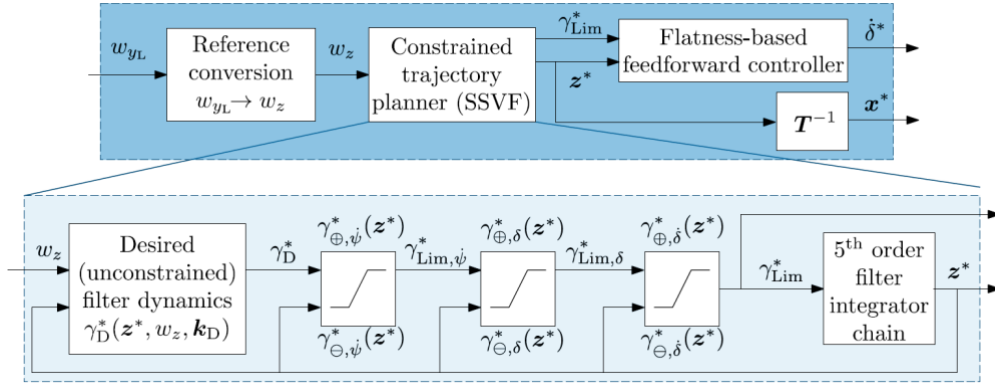


Figure 16: Structure of the inner solution part: A constrained flatness-based trajectory generator using the SSVF.

It is composed of a flatness-based feedforward controller to calculate the trajectories of the steering angle gradient,

$$u^* = \delta^* = z^* + a_3 \overset{(5)}{\ddot{z}^*} + a_4 \overset{(4)}{z^*}, \quad (4)$$

as well as a transformation of the target lateral displacements w_{yL} into a reference w_z for the flat output,

$$\begin{bmatrix} \dot{w}_z \\ \ddot{w}_z \end{bmatrix} = \begin{bmatrix} 0 & 1 \\ -\frac{c_{R,1}}{c_{R,3}} & -\frac{c_{R,2}}{c_{R,3}} \end{bmatrix} \begin{bmatrix} w_z \\ \dot{w}_z \end{bmatrix} + \begin{bmatrix} 0 \\ \frac{1}{c_{R,3}} \end{bmatrix} w_{yL}, \quad (5a)$$

$$w_z = [1, 0] [w_z, \dot{w}_z]^\top. \quad (5b)$$

In between these two components, a switched state variable filter (SSVF) (Joos, Bitzer, Karrelmeyer, & Graichen, 2019) calculates smooth trajectories for the flat output z and its time derivatives in dependence of the flat output reference w_z . It is designed for good output-tracking with respect to the target lateral displacement w_{yL} and considers the constraints on the flat state and the control input (2).

The SSVF is defined as

$$\dot{z}_i^* = z_{i+1}^*, \quad i = 1, \dots, n-1 \quad (6a)$$

$$\dot{z}_n^* = \gamma_{Lim}^* \quad (6b)$$

$$\gamma_{Lim}^* = \text{sat} \left(\gamma_{Lim, \delta}^*, \gamma_{\Theta, \delta}^*, \gamma_{\Theta, \psi}^* \right) \quad (6c)$$

$$\gamma_{Lim, \delta}^* = \text{sat} \left(\gamma_{Lim, \psi}^*, \gamma_{\Theta, \delta}^*, \gamma_{\Theta, \psi}^* \right) \quad (6d)$$



$$\gamma_{\text{Lim},\psi}^* = \text{sat} \left(\gamma_{\text{D}}^*, \gamma_{\ominus,\psi}^*, \gamma_{\oplus,\psi}^* \right) \quad (6e)$$

$$\gamma_{\text{D}}^* = -\mathbf{k}_{\text{D}}^{\text{T}} \mathbf{z}^* + k_{\text{D},1} w_z. \quad (6f)$$

It is basically an extended n -th order lag element, which can be represented as an unconstrained linear filter, whose desired dynamics (6f) drive a fifth order integrator chain (6a). The extension concerns the dynamical limitation (6c) - (6e) of the input signal of the filter integrator chain (6b) by the constraints (2) as illustrated in the block diagram in Figure 16.

For each planning cycle the trajectory generator is used to create sets $\{(\mathbf{x}^*(t), \delta^*(t))\}$ of trajectories by varying the target lateral displacements w_{y_L} and the maneuver trigger times t_{trig} at which the planned AES trajectories will substitute the current course of the vehicle. This variation is realized by equidistantly drawing fixed numbers N_{y_L}, N_{trig} of samples from the corresponding intervals of possible lateral displacements Y_L maneuver trigger times T_{trig} and calculating trajectories for all the resulting $N_{y_L} \cdot N_{\text{trig}}$ parametrization tuples $(w_{y_L}^{(i)}, t_{\text{trig}}^{(j)})$. The sampling interval Y_L for the target lateral displacements is provided by the Sensor subsystem and derived from the cameras lane detection. It spans from the lane center ($w_{y_L} = 0$ m) to the left/right lane border, depending on the direction of the evasive maneuver. Limiting the AES maneuvers to perform in-lane evasions ensures compliance with current regulations for automated emergency steering manoeuvres (UNECE, 2018). The direction of the maneuver depends on the motion of the VRU to evade. It is chosen to be into the direction of the VRUs motion as calculated by the VRU Intent & Trajectory Prediction module, such that the vehicle would pass in front of the VRU during the maneuver. According to the scenario analysis presented in Section 3.2, an evasion against the direction of the VRUs motion can lead to accident avoidance by AES in the case of a *frontal impact* of a pedestrian on the *distant corner* of the vehicle, too. But as only sensor and prediction uncertainties and no behavioral uncertainties are considered in this simulation analysis, the VRU might abruptly come to a stop, leading to an accident.

The sampling interval T_{trig} for the maneuver trigger times is derived from the information about a predicted collision that is provided by the Safety Decision subsystem (see Section 4.2.6). It spans from the time of trajectory generation ($t_{\text{trig}} = 0$ s) to the predicted time to collision when following the vehicles current trajectory τ_{col} .

As a cyclic trajectory replanning is performed throughout the AES maneuvers, once the maneuver has been triggered (the vehicle follows an AES trajectory), only the sampling of target lateral displacements is continued and the trigger time is fixed to the time of the current trajectory generation.

The most notable increments compared to the initial Trajectory Generation reported in (SAFE-UP, Deliverable report D3.3, 2022) are given below. The final version of the AES trajectory generator now features the transformation between the Frenet frame and the global frame for all calculated vehicle states as well as the steering angle gradient. Furthermore, to optimize the performance of the cyclic replanning of trajectories, a prediction of the initial state for the next planning cycle is performed to compensate for the steering actuator deadtime. Here, the



same lateral vehicle dynamics model as for the trajectory planning itself is used. Hence, a prediction of all states is calculated and used for the initialization.

4.2.5.2 Nominal driving trajectory generation

Nominal driving trajectory generation is used to compute the vehicle's trajectories for driving under nominal conditions when there is no need for any emergency maneuvering and the driving goal is to follow the path planned by the Path Planning subsystem.

It uses the constrained flatness-based trajectory generator from Section 4.2.5.1 with a less dynamic parametrization of the SSVF and with a target lateral displacement of $w_{yL} = 0\text{m}$. Additionally, instead of sampling trajectories, only a single trajectory per planning cycle is calculated. The planned trajectories reduce the lateral offset to the reference line, i.e. the path, starting from the current vehicle position. A cyclic replanning of nominal trajectories is performed throughout the driving operation, which generates the behavior of a low-frequency closed-loop path-tracking controller.

The most notable increments compared to the initial Trajectory Generation reported in (SAFE-UP, Deliverable report D3.3, 2022) are identical to those of the AES trajectory generator described in Section 4.2.5.1.

4.2.5.3 AEB trajectory generation

AEB trajectory generation performs the calculation of vehicle trajectories for an automated emergency braking maneuver. If a collision with a VRU is predicted for the vehicle following the nominal driving trajectory or during an AES maneuver, calculation of AEB trajectories will be triggered by the Safety Decision subsystem (see Section 4.2.6).

Although there might exist situations in which a mere velocity reduction could be sufficient to avoid a collision, the AEB intervention will always guide the vehicle to standstill, as these scenarios are not within the scope of this research work (see Section 3).

The current nominal trajectory is used as the basis for the AEB trajectories. The point in time at which the AEB should have brought the vehicle into standstill at the latest is determined via the predicted time of collision and the nominal trajectory. In contrast to the approach described in the (SAFE-UP, Deliverable report D3.3, 2022), in which the AEB intervention follows the path of the nominal trajectory, the braking maneuver in the final implementation is realized on a straight line trajectory. The AEB trajectories follow the nominal trajectory until deceleration is initiated. From the start of the deceleration, the AEB trajectories no longer contain any lateral dynamics. This simplification had to be made because the interfaces of the demo vehicles EPS (electronic power steering) and ESC (electronic stability control, braking system) systems cannot guarantee parallel steering and braking at the required high dynamics. This simplification of the system is justified as the scenarios examined only contain straight reference paths and the nominal trajectories should therefore also be almost straight. Another change to the development status reported in (SAFE-UP, Deliverable report D3.3, 2022) is that trajectories are sampled by varying a safety distance between the calculated



vehicles location of standstill and the predicted location of a collision (determined from the predicted time to collision τ_{col} and the currently followed trajectory provided by the Safety Decision subsystem, see Section 4.2.7.2) instead of sampling starting times of the AEB intervention. These safety distances can be set more intuitively and it is easier to validate whether the planned trajectories could be adhered to. A fixed number of trajectories is generated with safety distances sampled equidistantly from the interval of zero to a chosen maximum safety distance. Sampling is required because the AEB trajectory generation does not trigger the AEB intervention itself. The decision for an AEB intervention and the selection of a specific AEB trajectory depends on the risk assessment provided by the Crash Prediction & Avoidance Estimation subsystem, that considers also the inaccuracies of the VRU prediction (see Sections 4.2.6 and 4.2.6). When calculating the AEB trajectories, it is unknown which safety distance would lead to the lowest risk estimation.

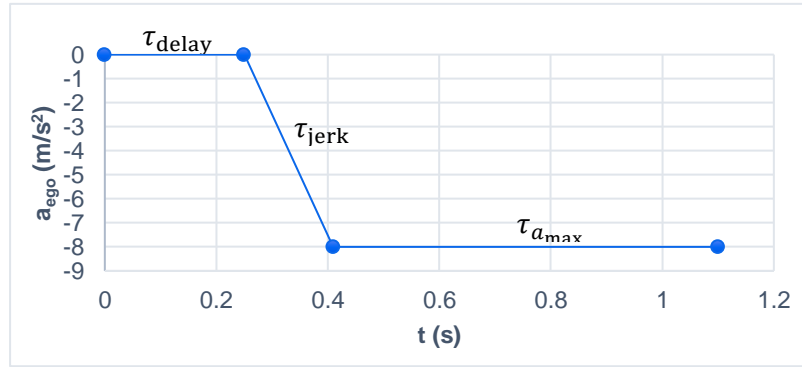


Figure 17: AEB deceleration model.

The calculation of the AEB trajectories is based on a longitudinal deceleration model of the vehicle, that is depicted in Figure 17. The model takes into account the delay and build-up (j , jerk) of a requested deceleration due to communication delay and the pressurization of the hydraulic braking system. Once the braking system is fully pressurized, the vehicles deceleration can be regarded as constant at a value of a_{max} . To calculate the minimum distance needed to bring the vehicle to standstill (dtb , distance threshold to brake), it is assumed that the vehicle velocity while nominal driving v_{ego} is constant. Since only crossing scenarios are considered in the demonstration, no velocity components of the VRU have to be considered. The distance threshold can then be described as

$$dtb(v_{ego}) = d_{delay}(v_{ego}) + d_{jerk}(v_{ego}) + d_{a_{max}}(v_{ego}) + d_{safety},$$

where $d_{delay}(v_{ego}) = v_{ego} \tau_{delay}$ describes the distance travelled during the duration of delay (τ_{delay}), $d_{jerk}(v_{ego}) = v_{ego} \tau_{jerk} + \frac{j}{6} \tau_{jerk}^3$ is the distance travelled during the duration of pressure build-up ($\tau_{jerk} = \frac{a_{max}}{j}$), $d_{a_{max}}(v_{ego}) = -\frac{a_{max}}{2} \tau_{a_{max}}(v_{ego})^2$ is the distance travelled at maximum deceleration until standstill, $\tau_{a_{max}} = -(v_{ego} + \frac{j}{2} \tau_{jerk}^2) / a_{max}$ and d_{safety} is the sampled safety distance.



Based on the assumption of constant vehicle velocity during nominal driving, the duration before the predicted collision at which the braking maneuvers must start are determined by $\tau_b = dtb/v_{ego}$. Figure 18 displays the dependency of dtb and τ_b on the vehicle velocity for the used parametrization of the longitudinal deceleration model (see Figure 17) and a safety distance of $d_{safety} = 0$ m.

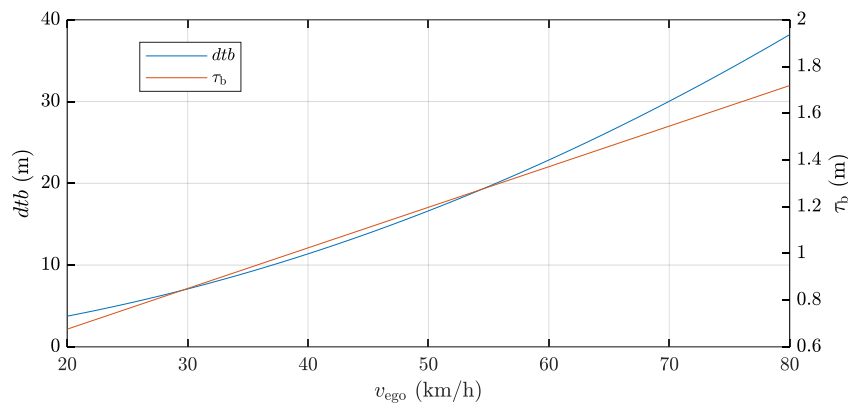


Figure 18: Dependence of dtb and τ_b on the vehicle velocity.

If avoidance by an AEB is not possible (dtb for $d_{safety} = 0$ m is larger than the distance between the vehicle and the location of the predicted collision), only a single trajectory is calculated that initiates an immediate braking maneuver to at least reduce the kinetic energy of a collision as much as possible.

4.2.6 Subsystem Crash Prediction & Avoidance Estimation

The subsystem Crash Prediction & Avoidance Estimation developed by THI is built upon the basic concepts of (SAFE-UP, Deliverable report D3.3, 2022). The deliverable D3.3 describes a deterministic risk estimation algorithm based on (Wang, Wu, Zheng, Ni, & Li, 2016). Also, a method of shape approximation and collision checking based on circles is described in (SAFE-UP, Deliverable report D3.3, 2022). Whereas the shape approximation and collision checking based on circles is kept for the final demonstrator vehicle, the deterministic risk estimation algorithm is improved to a probabilistic risk estimation algorithm. The motivation behind this change is that the VRU predictions (see Section 4.2.4) are strongly uncertain in the first instances of observation, which might cause false risk estimations and crash predictions. Having a probabilistic risk estimation mainly addresses the case of a false prediction. With a deterministic algorithm, where no information about the prediction quality, i.e. uncertainty, is taken into consideration, the trajectory decision could potentially select an unsafe trajectory. Here, a probabilistic risk estimation algorithm, considering the uncertainty, can be parameterized to suggest more conservative behavior and therefore a safer decision under high uncertainty.

(Tolksdorf, Tejada, van de Wouw, & Birkner, to be published) For this work, probabilistic risk is modeled as the expected severity of an event in accordance with (Tolksdorf, Tejada, van



de Wouw, & Birkner, to be published) $z_k \in \mathbb{R}^{n_\varepsilon}$. In $k \in \mathcal{E} \subseteq \mathcal{B}_{\varepsilon,k} \subseteq \mathbb{R}^{n_\varepsilon} \times k \in \mathcal{S} : \mathcal{B}_{\varepsilon,k} \rightarrow \mathbb{R}_{+,0} \subseteq \mathcal{B}_{\varepsilon,k}$. That said, the risk at time k is given by

$$R_k := \mathbb{E}[s(z_k)] = \int_{\mathcal{B}_{\varepsilon,k}} s(z) p_{z,k}(z) dz,$$

where $p_{z,k}$ denotes a probability density function at time instance k . This general description is operationalized for the demonstrator by assuming perfect knowledge of the ego vehicle's future configuration, a Gaussian distribution of the object's configuration, and a total kinetic energy model for the potential collision severity.

The orientation is neglected by assuming circular shape approximations and therefore the joint configuration is simplified to $z = ((x_e, y_e), (x_o, y_o))$. From the joint configuration, the severity can be derived by using the finite difference between two time instances as

$$s(z_k) = \frac{1}{2}(m_e v_{e,k}^2 + m_o v_{o,k}^2).$$

We define the event of a collision as

$$\mathcal{B}_{\varepsilon,k} := \left\{ \left((x_{e,k}, y_{e,k}), (x_{o,k}, y_{o,k}) \right) \mid \|r_k\| \leq r_{e,k} + r_{o,k} \right\},$$

where (x, y) denote the ego vehicle and object configuration, respectively. Further, $r_k = (x_{e,k} - x_{o,k}, y_{e,k} - y_{o,k})^T$ is the relative distance between both actors at time k . Lastly, r_e, r_o denote the radii of the respective circles of the actors, approximating the shape (see (SAFE-UP, Deliverable report D3.3, 2022)).

To implement the algorithm within the vehicle, the collision indicator function is introduced:

$$I_c \left((x_{e,k}, y_{e,k}), (x_{o,k}, y_{o,k}) \right) = \begin{cases} \|r_k\| \leq r_{e,k} + r_{o,k}, \\ 0, \text{ else.} \end{cases}$$

With the collision indicator function, the law of great numbers is utilized to approximate the probabilistic risk of collision with

$$R_k \approx \frac{1}{N} \sum_{n=1}^N I_c(z_n) s(z_n)$$

here z_n refers to a sample of a joint configuration at time instance k , drawn from $p_{z,k}$, parameterized by the mean and standard deviation provided at each time instance by the VRU prediction subsystem.

4.2.7 Subsystem Safety Decision

The subsystem safety decision developed by Bosch evaluates the planned future motion of the vehicle, controls the planning of motion alternatives (nominal driving, AEB maneuver, AES maneuver) and decides which of the planned trajectories will be followed.



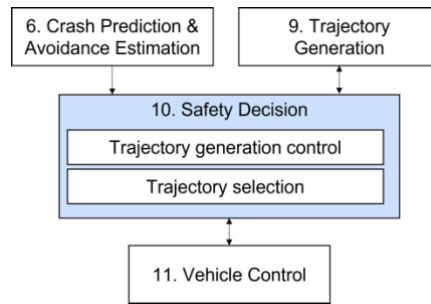


Figure 19: Overview of the Safety Decision (inter)dependencies.

A schematic of the subsystems (inter-)dependencies is depicted in Figure 19. The subsystem safety decision (in the following also called Safety Decision) receives the trajectories planned by the motion alternative submodules of the Trajectory Generation subsystem, their respective risk and avoidance estimates provided by the Crash Prediction & Avoidance Estimation subsystem, and information about the currently executed driving maneuver from the subsystem Vehicle Control (see Section 4.2.8). Based on these inputs Safety Decision performs two main tasks. First, the selection of the next trajectory to be followed from all planned alternatives (and thus scheduling of the driving maneuvers), that is then provided to the subsystem Vehicle Control (see Section 4.2.7.1), and second the control of the Trajectory Generation subsystem (see Section 4.2.7.2) in terms of decisions on which motion alternatives should be planned and providing the required aggregated information for these plannings.

4.2.7.1 Trajectory selection and maneuver scheduling

Safety Decision’s selection of the future trajectory to be followed and scheduling of the driving maneuvers is based on the comparison of the risk and avoidance estimations for planned trajectories and the currently active driving maneuver.

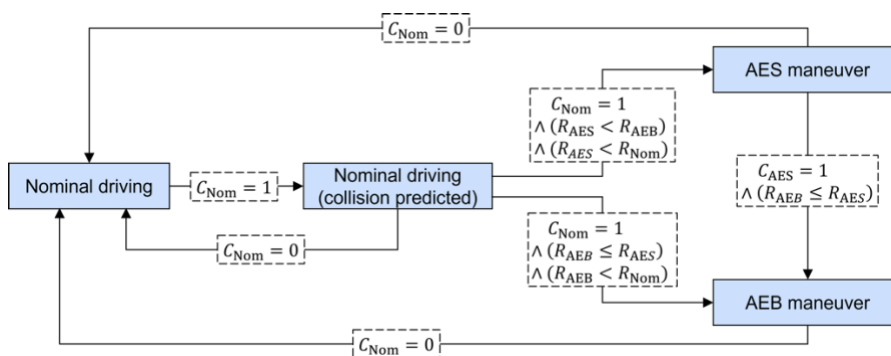


Figure 20: Maneuver scheduling logic of the subsystem safety decision.

Figure 20 shows a schematic view of the maneuver scheduling logic employed by Safety Decision. The subsystem distinguishes between four maneuver states (depicted as blue boxes): nominal driving, nominal driving (collision predicted), *AEB maneuver* and *AES*



maneuver. Within the state of *nominal driving* no safety thread has been recognized for the vehicle and thus no trajectory planning from an active safety system is needed. In the state of *nominal driving (collision predicted)*, a collision on the currently driven nominal trajectory has been predicted (and the trajectory planners for the AEB and AES trajectories have been activated) but not all information needed to decide on the scheduling of the following emergency maneuver is available yet. This information are up-to-date sets of both, planned emergency trajectories from every active emergency planner and their respective risk and avoidance estimates. Here trajectories are regarded as up-to-date, if they have been planned after the last information update provided by Safety Decision to the Trajectory Generation subsystem (check for Section 4.2.7.2). The safety system is set to be in states of *AEB maneuver* or *AES maneuver* depending on the selection of the respective future trajectory to be followed.

For each planned trajectory k of a set of planned trajectories, two quantities are derived from the respective risk and avoidance estimates. The collision indicator $C_{M,k}$ and the trajectory risk $R_{M,k}$, where $M \in \{\text{Nom}, \text{AES}, \text{AEB}\}$ indicates the respective type of trajectory (Nominal driving, AEB maneuver, AES maneuver). The collision indicator is given by $C_{M,k} = \begin{cases} 1, & \text{if } \sum_l I_C(z_l) \geq 1 \\ 0, & \text{else} \end{cases}$, where I_C is the collision indicator function and z_l are the respective joint configurations introduced in Section 4.2.6. The trajectory risk $R_{M,k}$ equals the risk of collision R as introduced in Section 4.2.6, but its comparison operations are subject to the rules $R_{K,a} < R_{L,b}$ if $\begin{cases} R_a < R_b \wedge C_{K,a} = C_{L,b} \\ C_{K,a} = 0 \wedge C_{L,b} = 1, \end{cases}$ where $K, L \in \{\text{Nom}, \text{AES}, \text{AEB}\}$ and R_a, R_b are the respective risks of collision corresponding to the trajectory risks $R_{K,a}, R_{L,b}$.

For the trajectory selection and the scheduling of maneuver states the subsystem safety decision first determines the trajectory with the lowest risk per trajectory type, resulting in the trajectory risks R_{Nom} , R_{AEB} and R_{AES} ($R_M = R_{M, \tilde{k}_M}$, $\tilde{k}_M = \underset{k}{\operatorname{argmin}} R_{M,k}$). With these risks and the corresponding collision indicators $C_M = C_{M, \tilde{k}_M}$ scheduling of maneuver states is performed as depicted in Figure 20, where the exact conditions for the state transitions are given in the dashed boxes. After the determination of the maneuver state the respective planned trajectory \tilde{k}_M is provided to the Vehicle Control subsystem for the execution of the maneuver.

In case of the *AES maneuver* state, there is a slight deviation from the procedure described above. Once Safety Decision has been signaled, the ongoing execution of an AES trajectory by the Vehicle Control subsystem, the evaluation of AES trajectories is changed. As long as the vehicle executes the current AES maneuver (that is as long as Vehicle Control has not signaled a subsequent execution of nominal trajectory, e.g. after an emergency situation has been resolved, or the *AEB maneuver* state is scheduled), sets of newly planned AES trajectories are filtered by their target lateral displacement w_{y_L} (see Section 4.2.5.1) prior to the determination of R_{AES} and C_{AES} . The filtering excludes all trajectories with a target lateral displacement less than the target lateral displacement of the trajectory previously selected for execution. This mechanism is implemented to prevent a planned reduction of lateral



displacement during the trajectory replanning of an ongoing AES maneuver, that could occur due to fluctuations of the predictions of the VRUs future motion. As described in Section 4.2.5.1, the lateral evasive motion of planned AES trajectories is always in the direction the VRUs motion, such that a reduction of lateral displacement would lower the distance to the evaded VRU. Therefore, the AES maneuver is performed with the target lateral deviation following the maximum of all trajectories previously selected during the maneuver.

4.2.7.2 Trajectory generation control

The planning of future trajectories by the Trajectory Generation subsystem is controlled by Safety Decision and based on the selection of future trajectories and the scheduled maneuver states depicted in Figure 20.

Depending on the current maneuver state, the motion alternative submodules of the trajectory generation are activated (once planning of the respective trajectories is needed) or deactivated (once the respective maneuver state of a motion alternative cannot be reached any longer). Table 8 summarizes the dependence of the Trajectory generation submodule on the current maneuver state.

Table 8: The dependence of trajectory generation on maneuver state.

Maneuver state	Trajectory generation submodule		
	Nominal driving trajectory generation	AES trajectory generation	AEB trajectory generation
Nominal driving	active	inactive	inactive
Nominal driving (collision predicted)	active	active	active
AES maneuver	active	active	active
AEB maneuver	active	inactive	active

Nominal trajectories are constantly planned throughout all driving states for two reasons. Firstly, to ensure the existence of a nominal trajectory based on the most current information regarding the vehicles state and its surroundings for a smooth transition from an emergency maneuver back to the nominal driving operation. Secondly, the planning of AES and AEB trajectories depends on the availability of a current nominal trajectory as parts of this trajectory may be incorporated into the planned emergency alternatives, as described in Section 4.2.3.

In addition to the activation/deactivation of trajectory generation submodules, Safety Decision also provides information regarding the planned and predicted future of the driving situation to the generation submodules. This contains information about the currently selected trajectory itself, which is needed by the generators to ensure a smooth concatenation of subsequent trajectory plannings, as well as information about a potentially predicted collision that has been obtained from the Crash Prediction & Avoidance Estimation subsystem. The



predicted time to collision τ_{col} when following the currently selected trajectory is used to limit the temporal sampling space of the emergency planners (see Sections 4.2.5.1 and 4.2.5.3).

4.2.8 Subsystem Vehicle Control

Bosch developed the subsystem Vehicle Control, that receives selected trajectories from the safety decision subsystem and sends braking and steering commands at a cycle time of 20 ms to the ESC and EPS systems of the vehicle as described in (SAFE-UP, Deliverable report D3.3, 2022). The currently executed maneuver is reported back to the subsystems safety decision and Trajectory Generation (see Sections 4.2.3 and 4.2.6).

As described in the sections above, the cyclic trajectory replanning acts as a low-frequency feedback path for vehicle control by taking updates of the vehicle states as well as environmental information into account. This low-frequency feedback in combination with the model-based feedforward steering commands calculated by the Trajectory Generation subsystem already lead to a rather satisfactory tracking of the vehicles planned lateral deviation (see Section 5.3.1.2). To further increase the quality of the systems trajectory tracking additional high-frequency trajectory tracking controllers will be implemented in the vehicle.

Firstly, a PI controller acting on the steering angle and utilizing the feedforward steering commands of the planned trajectories has been developed. Secondly, a state-feedback controller acting on the braking system will utilize wheel-individual brake interventions to perform a steer-by-brake action. This approach will enable the system to also partially compensate detrimental effects of unintended driver reactions to an emergency situation. A typical reaction pattern of a shocked driver will be a short but firm grasp on the steering wheel, temporary blocking the systems steering intervention and thus lowering the lateral deviation that can be achieved by an AES maneuver (Schneider, 2018).

At the time of this report, both of these complementary control strategies have been tested in simulation. Implementations in the vehicle have not yet been tested in the vehicle due to delays in the optimization of the controller parameters for the demonstrator vehicle. Test results of the controller's operation will be reported in (SAFE-UP, Deliverable report D3.8, 2023).



5. Demo 3 test results

During Demo 3 development, three software integration and testing weeks were conducted, where all partners met at Bosch testing facilities to integrate, test and fine tune the developed subsystems and algorithms in the relevant Demo 3 scenarios according to Section 3.2. Some impressions from the integration and testing workshops are shown in Figure 21 and Figure 22.



Figure 21: The Demo 3 team on the Bosch test track.

The present section contains selected qualitative test results of the developed subsystems proving their general functionality. Extensive quantitative measurement evaluations of both the whole system and the subsystems will follow in the deliverable report (SAFE-UP, Deliverable report D3.8, 2023). An estimation of the Demo 3 safety benefit based on both physical and simulative testing will follow with deliverable reports (SAFE-UP, Deliverable report D5.3, 2023) and (SAFE-UP, Deliverable report D5.6, 2023) of Work Package 5.





Figure 22: Impressions from system testing during a Demo 3 integration workshop.

5.1 Test results Path Planning

Before integration in the Demo 3 complete system, additional tests are performed in simulation, as well as on the TNO demonstrator platform, in addition to what has been described in (SAFE-UP, Deliverable report D3.3, 2022) Chapter 5.1. The performance results in simulation can be found in (R. Smit, 2022) and (C. van der Ploeg, 2022), where it is shown that the planners are able to deal with various road layouts and are able to anticipate on the predicted motions of other traffic participants.

To show the capability of navigating various road layouts, closed loop automated driving tests using the TNO demonstrator platform are carried out at the Aldenhoven Testing Center, Germany. Here a global high-level route is drafted for the path planner to navigate, including two 90° turns and a roundabout. The reference path, proposed trajectories and final closed loop driven path are depicted in Figure 23 and Figure 24 for the sampling based planner and the MPC planner respectively. Furthermore, some relevant Key Performance Indicators (KPIs) for navigating this road layout are plotted in Figure 25 and Figure 26. From these results, we concluded that, due to the sampling-based nature of the SST planner, the resulting proposed state to follow could contain substantial noise. However, due to its sampling-based nature, the SST planner is able to deal with more complex environments, which are difficult to capture in the polynomial-based road description used by the MPC planner. Using the MPC for more complex environments is future work for TNO and is seen as the ideal hybrid combination. As such, for the demonstrator it was decided to include the MPC-based planner for the final DEMO3 software.



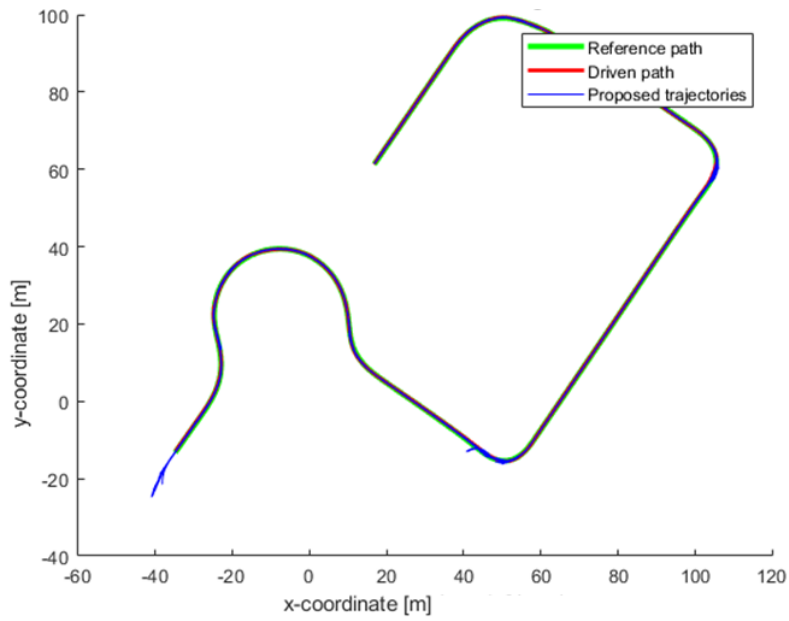


Figure 23: Reference path, proposed trajectories and driven path for sampling based path planner benchmark.

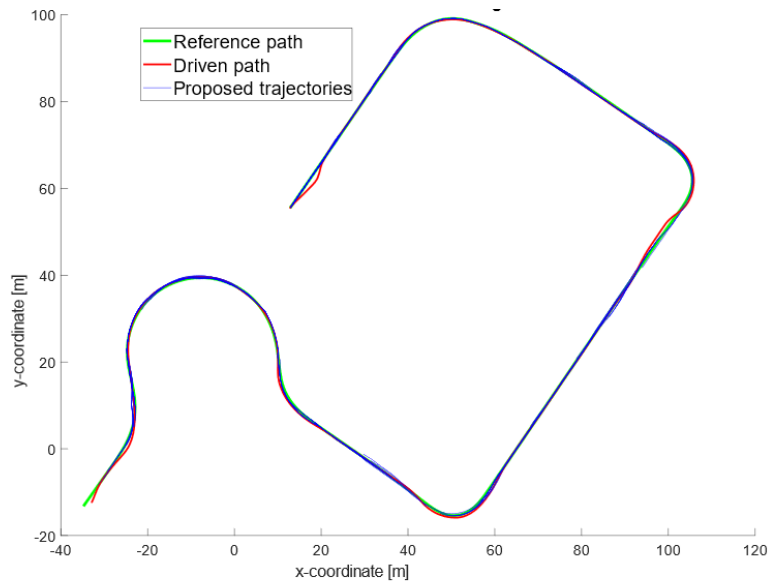


Figure 24: Reference path, proposed trajectories and driven path for MPC based path planner benchmark.



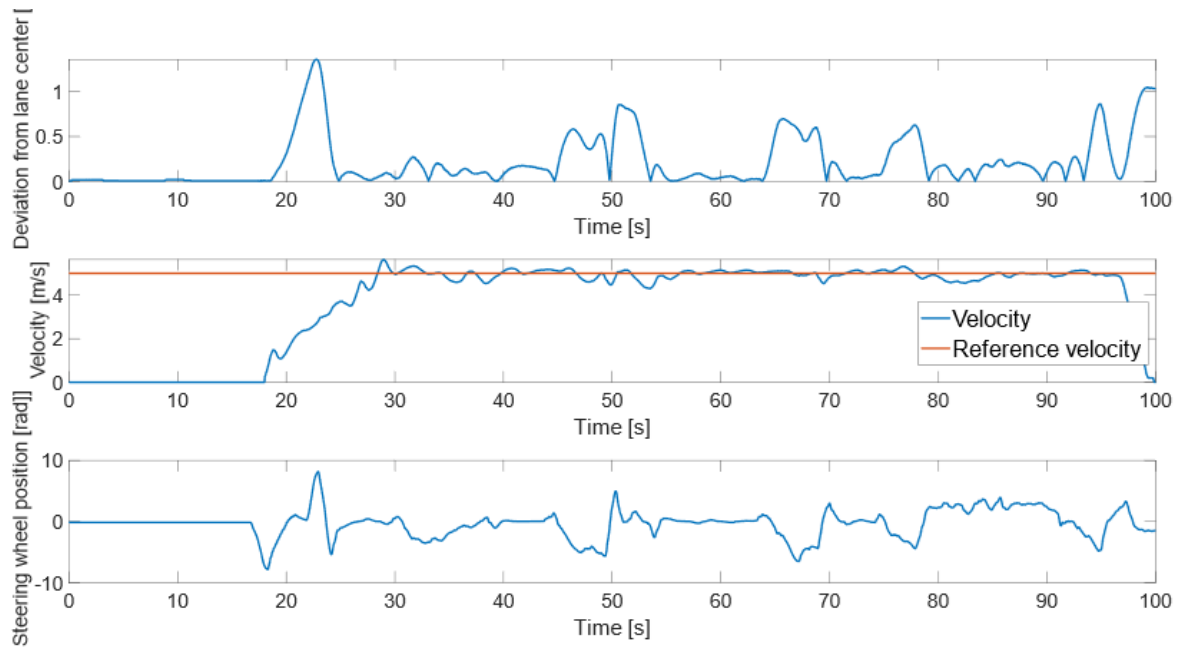


Figure 25: Variables of interest (KPIs) for the sampling based planner.

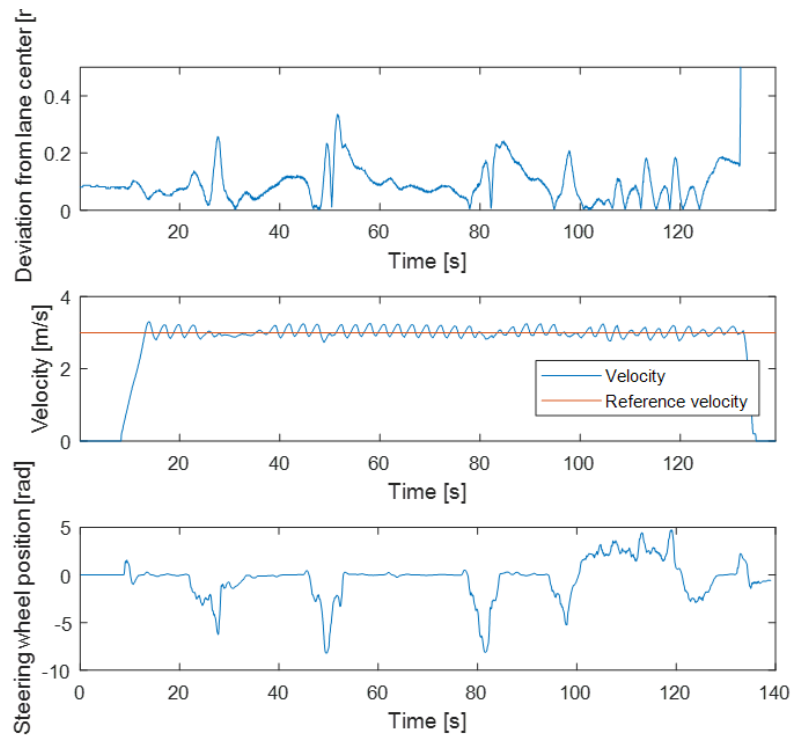


Figure 26: Variables of interest (KPIs) for the MPC based planner.



5.2 Test results VRU Intent & Trajectory Prediction

Prediction accuracy is reported for the point in time where there could be a critical situation if no pre-emptive action is taken based on the current ego trajectory and the predicted VRU trajectory. For each evaluated scenario, this reference point is taken at the time the VRU enters the ego's driving corridor as illustrated in Figure 7. For any time before that in which the pedestrian is detected, predictions are generated for the critical time. To evaluate the accuracy of the predictions, the mean and standard deviation of final displacement error (FDE) is reported, which is computed as the Euclidean distance between the predicted and the true VRU positions.

Figure 27 shows the mean and standard deviation of the predictions' FDE at the critical time based on 27 measurements. The critical time for which predictions are reported is considered TCP $t=0$ from Figure 7, and how much time in advance these predictions were generated is depicted in the x-axis. Additionally, Table 9 provides specific values at some of the horizons for clarity. Two evaluations were performed: first using the inputs from the object fusion & tracking module, which in some situations can introduce tracking inaccuracies that are highly detrimental for the predictions. Next, a higher-fidelity sensor suite is simulated by using the VRU's reference data, which yields a significant improvement. Based on this conclusion, a trade-off could be made in prediction accuracy w.r.t. the required future sensor performance of future vehicles using prediction algorithms.

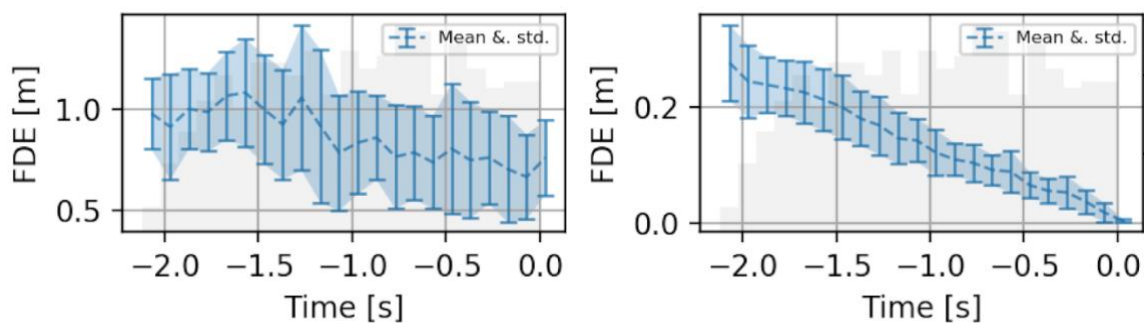


Figure 27: FDE mean and standard deviation of predictions when using lower-fidelity object tracking (left) and high-fidelity tracking (right).



Table 9: FDE mean and standard deviation of some prediction horizons when using lower-fidelity object tracking and high-fidelity tracking.

	Time [s]	-2	-1.6	-1.2	-0.8	-0.4	-0.03
Lower-fidelity tracking	FDE [m]	0.91	1.09	0.92	0.77	0.75	0.76
	FDE std. [m]	0.26	0.27	0.38	0.26	0.29	0.19
High-fidelity tracking	FDE [m]	0.25	0.21	0.15	0.1	0.06	0
	FDE std. [m]	0.06	0.05	0.04	0.03	0.02	0

5.3 Test results AES Trajectory Generation

The following section contains test results for the AES trajectory generation subsystem. As the nominal driving trajectory generator uses the same approach for trajectory generation as the AES trajectory generator, but in a simplified way, no specific test results for the nominal case are listed here. Test results for both the nominal driving trajectory generator and the AEB trajectory generator will be included in the following D3.8 deliverable report.

The AES trajectory generator designed in 4.2.5.1 is tested by means of both a simulation and the application in the Demo 3 vehicle. First, the simulation presented in 5.3.1.1 focuses on the demonstration of the trajectory sampling process in an artificial situation. Afterwards, the vehicle experiment described in 5.3.1.2 aims to investigate the planner's performance with respect to accuracy in a specific pedestrian crossing scenario.

5.3.1.1 Simulation

For the purpose of a simulation study, the AES trajectory generator is embedded into a MATLAB simulation framework, where possible collision scenarios can be generated synthetically. The main goal of the simulation experiment is to provide an illustrative and comprehensive access to the process of trajectory planning by means of an example under 'clinical' conditions. In the considered example, the vehicle is assumed to follow the lane center while a pedestrian is crossing the lane, leading to a potential collision. The planning cycles calculated during the complete scenario are restricted to two. Furthermore, limited amounts of three samples for both t_{trig} and w_{y_L} are drawn. The simulation directly generates the sampling intervals T_{trig} and Y_L which are necessary to execute the trajectory optimization. For simplicity, the vehicle is further assumed to perfectly follow the planned trajectories.



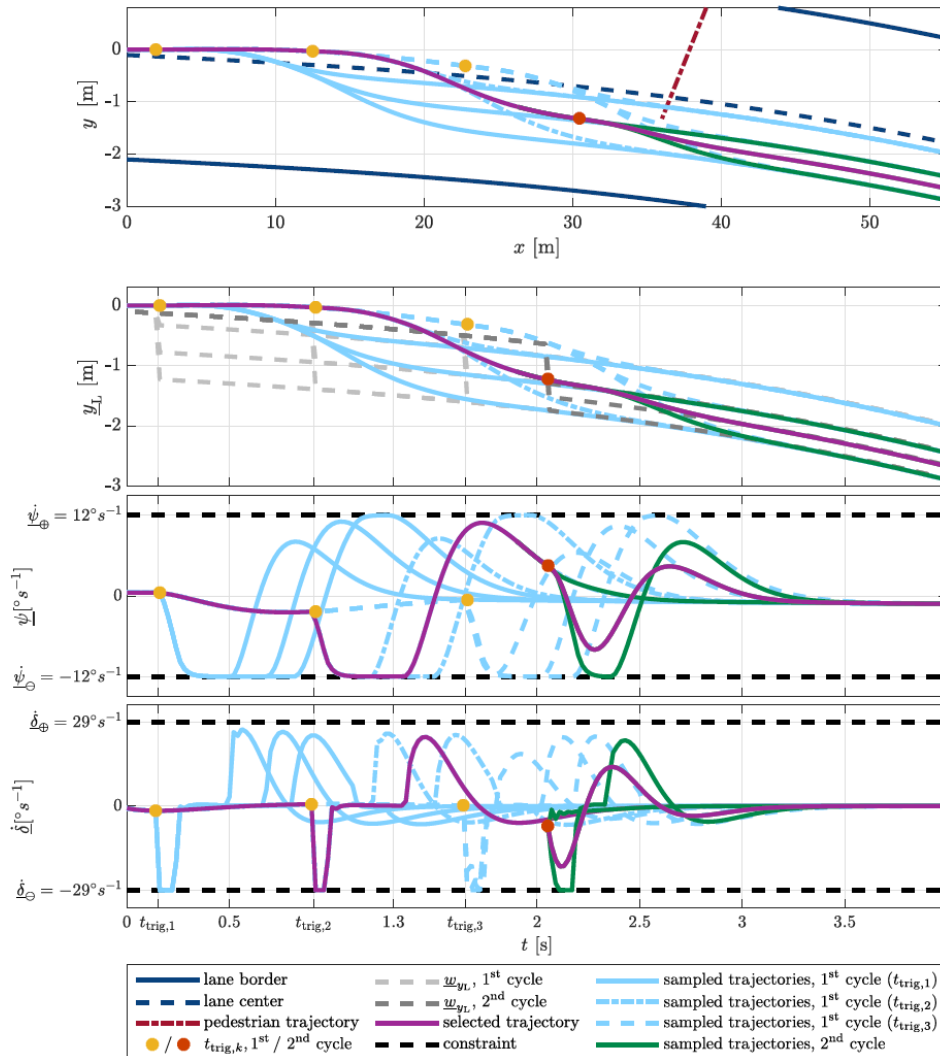


Figure 28: Example of the AES trajectory sampling by means of the simulation results.

The simulation setup is detailed in the following by means of the plots given in Figure 28. Note that the plots are narrowed down to the most relevant signals which are the sampled trajectories in the upper graph as well as the time evolutions of the planned lateral offset y_L , yaw rate $\dot{\psi}$ and the steering angle gradient $\dot{\delta}$ that are shown in the lower graph. All signals are represented in the global frame.

In the depicted scenario, the vehicle follows a typical lane of a width of 4 meter. Its borders are marked as the two solid dark blue lines. The lane center, dashed dark blue line, serves as the path, i.e. the reference line of the trajectory generator. The pedestrian trajectory is illustrated as dash-dotted dark red line. The vehicle velocity is assumed to be constant at typical urban driving speed of $v = 13.8ms^{-1}$. Three samples for both t_{trig} and w_{y_L} are drawn, leading to the trajectories of the first planning cycle, shown in light blue, with the trigger time encoded to the trajectories stroke style and emphasized by the light orange dots. The dashed



light grey lines represent the target lateral displacement values \underline{w}_{y_L} . For parts of the trajectories previous to their respective trigger, i.e. for $t < t_{trig,k}$ the nominal driving trajectory generator is active, trying to follow the lane center. The trajectories selected for the execution of the AES maneuver are depicted in violet. A second planning cycle is initiated at $t \sim 2.05s$ with sampled trajectories shown in green color and their target lateral displacements \underline{w}_{y_L} represented by the dashed dark gray lines. As the starting time of this planning cycle, emphasized by the dark orange dots, is larger than the trigger time $t_{trig,2}$ of the previously chosen trajectory, the maneuver trigger time is fixed to $t_{trig} = 0$ s. Only w_{y_L} is now sampled within an interval that is assumed to be updated by the Object Fusion & Tracking subsystem due to an intermittent change of the scenario.

The simulation demonstrates the AES trajectory generator's capability of planning AES trajectories that satisfy the given controllability and actuator constraints in terms of yaw rate and steering angle gradient. Moreover, the simulation results show an effective constraint exploitation, leading to maximized dynamics for the evasive maneuver, as can be seen from the lower graph of Figure 28. Due to the cyclic replanning of trajectories, the trajectory generator is capable of adapting to environmental changes.

5.3.1.2 Vehicle application

The present section demonstrates the application of the AES trajectory generator in the Demo 3 vehicle. As test scenario, the *P-CRWSO frontal impact, close corner* the according to the definition in Section 3.2 is used. The obstruction is located close to the lane border, such that an AEB accident avoidance is infeasible. The vehicle velocity is constant at $v = 13.8ms^{-1}$ and the pedestrian velocity is constant at $v = 1.67s^{-1}$. The impact constellation of vehicle and pedestrian without any emergency system intervention is such that the pedestrian center would be hit by the vehicles front right corner. The Vehicle Control unit purely forwards the flatness-based feedforward control input $\tilde{\underline{\delta}}^*(t)$ to the steering actuator, which acts as a low-level controller for the target steering angle $\tilde{\underline{\delta}}^*(t)$. No additional trajectory tracking controller is used for the testing. The position and heading data is captured using a fused Global Navigation Satellite System (GNSS)/Inertial Navigation System (INS) solution with a specified position accuracy of 2cm, while the yaw rate and steering angle signals are measured by embedded vehicle sensors. A delay of $t_d = 0.15s$ of the steering actuator is considered in all planned states, except the steering angle $\underline{\delta}(t)$ as this state acts as the control value for the steering actuator. The replanning cycle of the AES planner is set 200ms.

An exemplary measurement from the test is shown in Figure 29. More precisely, it contains the AES trajectory states $\underline{y}_L(t)$, $\underline{\psi}(t)$, $\underline{\dot{\psi}}(t)$, $\underline{\delta}(t)$ as well as the control input $\underline{\dot{\delta}}(t)$ in the global frame in top down order.



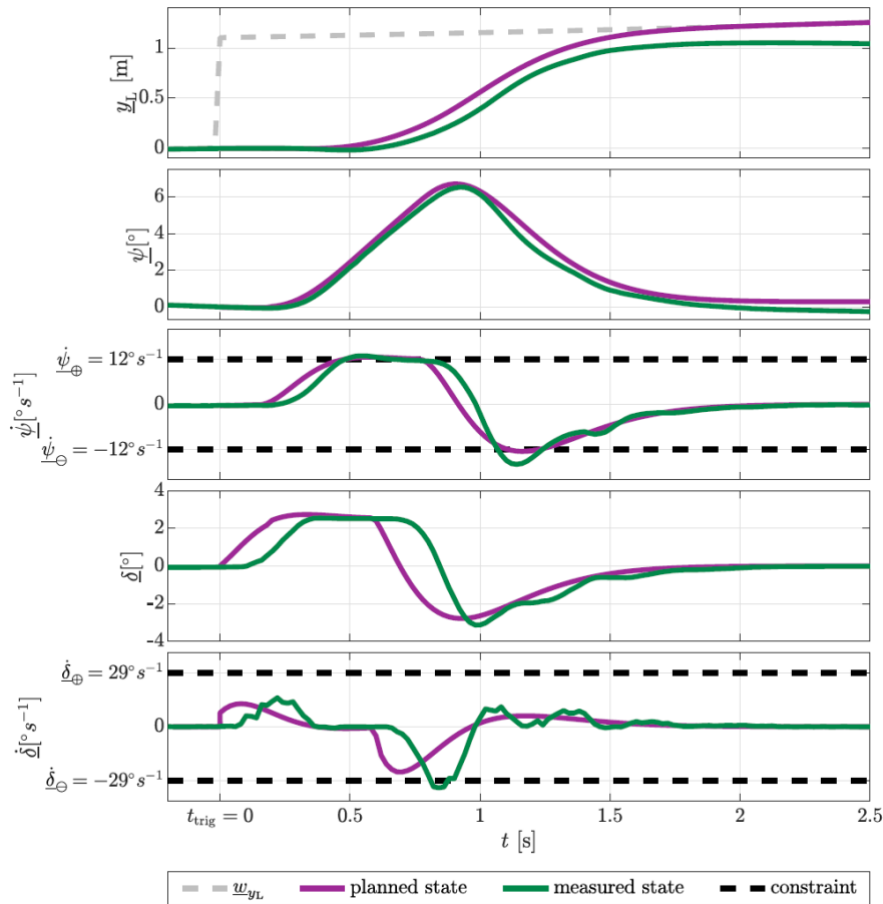


Figure 29: Planned and measured constrained state and input trajectories for a driven AES maneuver.

Note that the slip angle β is not further discussed here, as it is negligible for the trajectory dynamics of the investigated scenario. The planned trajectories of each signal are plotted in violet, while actually measured signals are colored green. In the top most graph, the dashed gray line represents the target lateral displacement \underline{w}_{y_L} . The controllability constraints (2c) and actuator limits (2a) are included as dashed black lines in the respective graphs. Further note that the state constraints (2b) of the steering angle lie outside the displayed range, as the much more restrictive controllability constraints (2c) limit the maximum steering angle. In the vehicle the target steering angle $\underline{\delta}^*(t)$ acts as a feedforward-only control request for the steering system. Therefore, the fourth graph in Figure 29 shows the pure following behavior of the low-level controller of the steering actuator. Towards the end of the maneuver, around $t \sim 0.8s$, this underlying controller leads to a higher steering angle speed than requested by the planner as the decreased dynamics at the end of the AES maneuver do not saturate the controller limits. Due to this fact the steering angle controller is able to compensate for its delay t_d at time $t \sim 1s$. According to the third graph, the planned yaw rate stays within its constraints, while the measured yaw rate shows two overshoots at $t \sim 0.5s$ and $t \sim 1.2s$. Due to the vehicle setup of a purely feedforward-based control, the first slight violation is assumed



to be caused by model uncertainties. In contrast, the second violation results from the steering angle controller behavior leading to a higher steering angle speed than requested by the planner as described above. This behavior is not the result of the general limitations of dynamics, but rather of the parametrization of the vehicles steering angle controller. Hence, it can be addressed by implementing an additional closed-loop controller on the lower prioritized states of the SSVF, e.g. the yaw rate itself, and by fine tuning the controller of the steering system. The AES trajectory in the first graph as well as the yaw angle in the second graph show an increasing deviation between planned and measured states over time, caused by the accumulation of lower order state errors. These deviations can be decreased by a closed-loop trajectory tracking controller.

However, considering the fact that the considered control implementation is feedforward-only, the tracking behavior observed for states can be judged as very satisfactory.



6. Simulations with focus on adverse weather conditions

This chapter details the background for the scenario specification as well as the simulation and trajectory analysis of conflicts to evaluate the impact of adverse weather conditions on intervention functions and to identify potential further developments.

6.1 Velocity analysis for passenger car conflicts with pedestrians and cyclists

The basis for all further accident data analysis is the result of the clustering of conflict situations for passenger car-to-pedestrian and passenger car-to-bicycle crashes published within SAFE-UP Deliverable D2.6 (SAFE-UP, Deliverable report D2.6, 2021). For passenger car-to-pedestrian and passenger car-to-bicycle in total for each group nine different conflict scenarios are identified and the scenarios and the description and meaning are used in this deliverable.

6.1.1 Passenger car conflicts with Pedestrian

For the analysis of passenger car (PC)-to-pedestrian(P) conflict scenarios the following six scenarios had been taken into account for the analysis as published in D2.6:

PC moves forward:

1. P crossing from left without sight obstruction, abbreviated with: P-CLwoSO
2. P crossing from left with sight obstruction: P-CLwSO
3. P crossing from right without sight obstruction: P-CRwoSO
4. P crossing from right with sight obstruction: P-CRwSO
5. P walking in longitudinal direction: P-Long

PC moves backwards:

6. PC reverse: P-PCRev

For the scenarios defined when the passenger car turns: 7. PC turning left (P-PCTurnL) and 8. PC turning right (P-PCTurnR), the scenarios are divided into in total four groups according to the turning direction of the passenger car and the walking direction of the pedestrian as illustrated in Figure 30 and described as the following:

1. PC turning left: P-PCTurnL



- | | |
|--|---------------|
| 7.1 PC turning left, P same direction | P-PCTurnL-SD |
| 7.2 PC turning left, P opposite direction | P-PCTurnL-OD |
| 2. PC turning right: | P-PCTurnR |
| 8.1 PC turning right, P same direction | P -PCTurnR-SD |
| 8.2 PC turning right, P opposite direction | P-PCTurnL-OD |

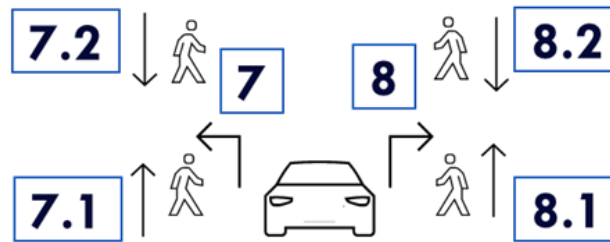


Figure 30: P conflict scenarios definition for PC turning.

The speed analysis is done using the GIDAS PCM dataset 2020-1 which is the same dataset used for the trajectory analysis published in D2.6. To have a common timestep for all results a fixed time-to-collision (TTC) at 2.5s is used to extract speed information of the passenger car and the pedestrian. This timestep had been identified as a fixed time where in most of the cases no driver reaction has taken place and to have an exact time definition valid for all cases. For all ten pedestrian conflict scenarios described above the speed information as displayed as an example for P-CLwoSO in Figure 31 is given for the passenger car.

Figure 31 gives information of the passenger car speeds in P-CLwoSO based on value distribution parameters displayed as a boxplot, that are: mean, minimum value (min), 25th percentile (25%), 50th percentile, median (50%), 75th percentile (75%) and maximum value (max) and a cumulative sum of speeds driven dependent on the sustained injury severity of the pedestrian. The information given are here: Coverage of 10% and 90% of all passenger car speeds.

As documented in Figure 31 based on 298 GIDAS-PCM cases the 50th percentile, median speed in P-CLwoSO conflict scenario is 45 km/h when considering all injury severities of the pedestrian. The 25th percentile is 35 km/h and the 75th percentile is 50 km/h. Additionally 10% of the passenger cars have a driving speed at TTC=2,5s in the range between 0 km/h and 21 km/h. When focusing on 90% of all speeds driven the range is between 0 km/h and 60 km/h.

Additionally, Figure 32 gives the same information on walking speeds of the pedestrian in P-CLwoSO conflict scenario. The 50th percentile of walking speeds is 5 km/h. 90% of all pedestrians have walking speeds between 0 and 15 km/h.



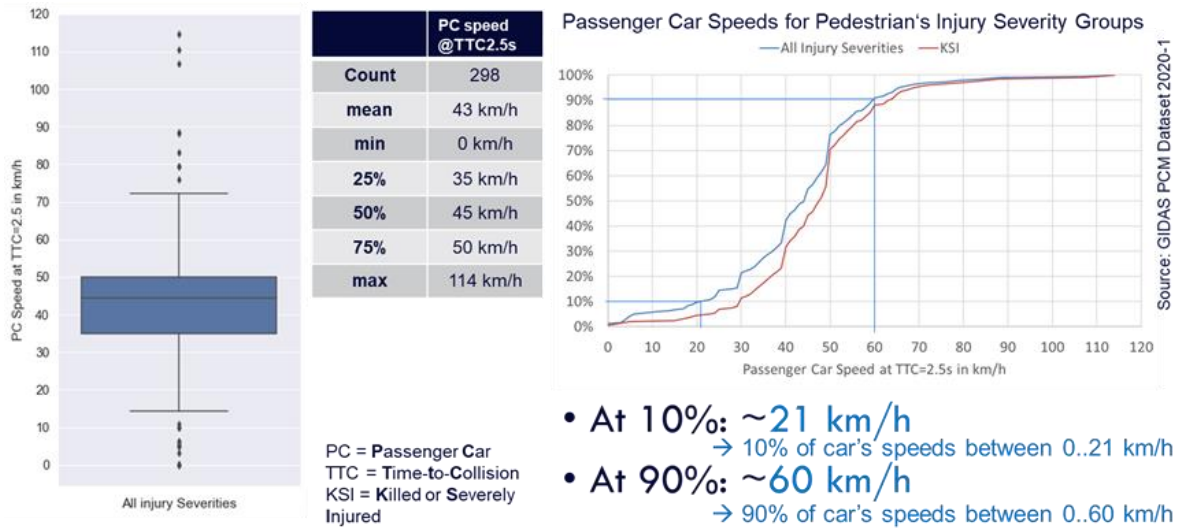


Figure 31: Passenger car speed information for P-CLwoSO at TTC=2.5s.

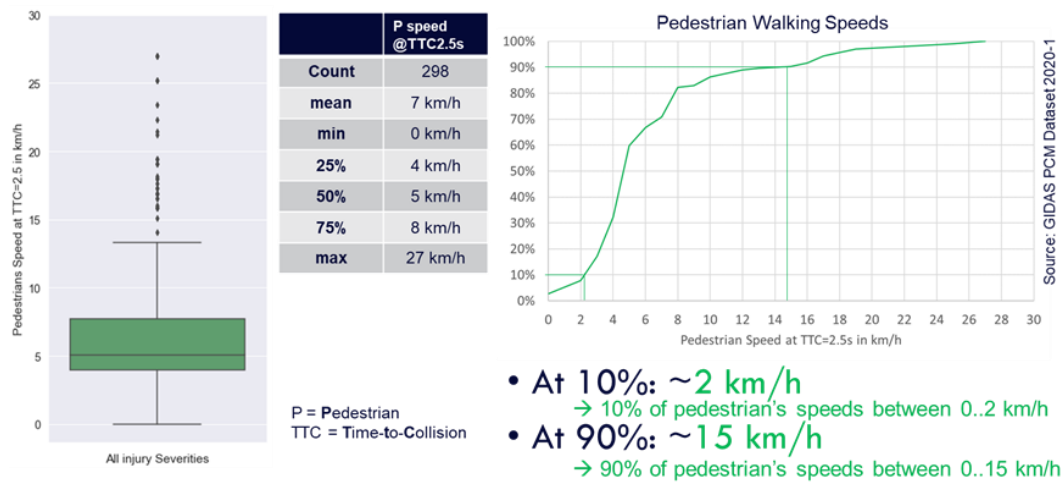


Figure 32: Pedestrian walking speed information for P-CLwoSO at TTC=2.5s.

In Table 10 information for all 10 conflict scenarios is given.

Table 10: Passenger car conflicts with pedestrians information.

P ID	Conflict Scenario	Injury Severity Group	Count	Passenger Car speed information at TTC=2.5s								Pedestrian walking speed information at TTC=2.5s							
				mean in km/h	min in km/h	25% in km/h	50% in km/h	75% in km/h	max in km/h	coverage at 10%	coverage at 90%	mean in km/h	min in km/h	25% in km/h	50% in km/h	75% in km/h	max in km/h	coverage at 10%	coverage at 90%
1.	P-CLwoSO	All Injury severities	298	43	0	35	45	50	114	0.21 km/h	0.60 km/h	7	0	4	5	8	27	0.2 km/h	0.15 km/h
1.	P-CLwoSO	KSI	201	47	0	40	48	53	114	0.30 km/h	0.63 km/h	-	-	-	-	-	-	-	-
2.	P-CLwoSO	All Injury severities	263	36	0	28	35	45	109	0.19 km/h	0.50 km/h	8	0	5	6	9	27	0.1 km/h	0.16 km/h
2.	P-CLwoSO	KSI	142	38	9	30	40	47	96	0.24 km/h	0.52 km/h	-	-	-	-	-	-	-	-
3.	P-CRwoSO	All Injury severities	406	38	0	30	40	48	104	0.14 km/h	0.54 km/h	6	0	4	5	8	27	0.2 km/h	0.13 km/h
3.	P-CRwoSO	KSI	212	42	0	34	45	50	99	0.17 km/h	0.58 km/h	-	-	-	-	-	-	-	-
4.	P-CRwoSO	All Injury severities	380	36	0	28	35	45	97	0.19 km/h	0.51 km/h	8	0	5	6	8	27	0.2 km/h	0.15 km/h
4.	P-CRwoSO	KSI	182	40	0	30	40	48	97	0.24 km/h	0.55 km/h	-	-	-	-	-	-	-	-
5.	P-Long	All Injury severities	36	52	10	39	50	67	89	0.20 km/h	0.79 km/h	4	0	3	5	5	7	0.2 km/h	0.6 km/h
6.	P-PCRev	All Injury severities	47	5	0	0	5	8	18	0 km/h	0.10 km/h	3	0	2	3	4	13	0 km/h	0.5 km/h
7.1	P-PCTurnL-SD	All Injury severities	66	23	0	16	24	30	42	0.12 km/h	0.30 km/h	6	0	4	5	6	21	0.2 km/h	0.8 km/h
7.2	P-PCTurnL-OD	All Injury severities	86	18	3	15	20	24	41	0.7 km/h	0.28 km/h	5	0	2	5	5	16	0.2 km/h	0.7 km/h
8.1	P-PCTurnR-SD	All Injury severities	25	19	0	15	20	26	40	0 km/h	0.31 km/h	4	0	3	4	5	8	0.2 km/h	0.6 km/h
8.2	P-PCTurnL-OD	All Injury severities	21	17	0	10	17	23	29	0.4 km/h	0.26 km/h	5	3	4	5	5	7	0.3 km/h	0.6 km/h



6.1.2 Passenger car conflicts with bicyclists

For the analysis of passenger car (PC)-to-bicyclists (B) conflict scenarios the following eight scenarios had been taken into account for the analysis as published in D2.6:

PC moves forward:

- | | |
|---|----------|
| 1. Bicyclist crossing from right: | B-CR |
| 2. Bicyclist crossing from left: | B-CL |
| 3. Bicyclist longitudinal same direction: | B-LongSD |
| 4. Bicyclist longitudinal opposite direction: | B-LongOD |

PC moves backwards:

- | | |
|---|---------|
| 5. Bicyclist in conflict with PC reversing: | B-PCRev |
|---|---------|

PC is stationary:

- | | |
|---|----------|
| 6. Bicyclist in conflict with stationary PC | B-PCStat |
|---|----------|

PC turns:

- | | |
|--|-----------|
| 7. Bicyclist in conflict with PC turning left | B-PCTurnL |
| 8. Bicyclist in conflict with PC turning right | B-PCTurnR |

For the scenarios defined when the bicyclist crosses the forward moving passenger car: 1. Bicyclist crossing from right (B-CR) and 2. Bicyclist crossing from left (B-CL), subgroups are derived based on the existence of a view obstruction for the passenger car driver as illustrated in Figure 33 and described as the following:

- 1.a Bicyclist crossing from right with sight obstruction B-CRwSO
- 2.a Bicyclist crossing from left with sight obstruction B-CLwSO

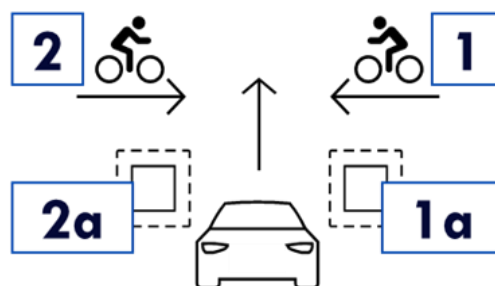


Figure 33: B conflict scenarios definition for PC moves forward and bicyclist crossing.

In both scenarios 1.a and 2.a only cases with view obstruction of any kind are included. Therefore 1.a forms a subset of 1. and 2.a forms a subset of 2.

The speed analysis is done using the GIDAS PCM dataset 2020-1 which is the same dataset used for the trajectory analysis published in D2.6. To have a common timestep for all results



a fixed time-to-collision (TTC) at 2.5s is used to extract speed information of the passenger car and the bicyclist. For all ten bicyclist conflict scenarios described above the speed information is displayed as an example for B-CR in Figure 34 for is given for the passenger car.

The Figure 34 gives information of the passenger car speeds in B-CR based on value distribution parameters displayed as a boxplot, that are: mean, minimum value (min), 25th percentile (25%), 50th percentile, median (50%), 75th percentile (75%) and maximum value (max) and a cumulative sum of speeds driven dependent on the sustained injury severity of the bicyclist. The information given are here: Coverage of 10% and 90% of all passenger car speeds.

The information of 1142 passenger cars involved in B-CR conflict scenario is aggregated. the 50th percentile, median speed in B-CR conflict scenario is 15 km/h when considering all injury severities of the bicyclists. The 25th percentile is 8 km/h and the 75th percentile is 29 km/h. Additionally 10% of the passenger cars have a driving speed at TTC=2,5s of 0 km/h. That means that 10% of the passenger cars are standing at that specific timestep before accelerating and having the conflict with the bicyclist. When focusing on 90% of all speeds driven the range is between 0 km/h and 45 km/h.

Additionally, Figure 35 gives the same information on riding speeds of the bicyclist in the B-CR conflict scenario. The 50th percentile of bicyclists' riding speeds is 15 km/h. 90% of all bicyclists have riding speeds between 0 and 22 km/h.

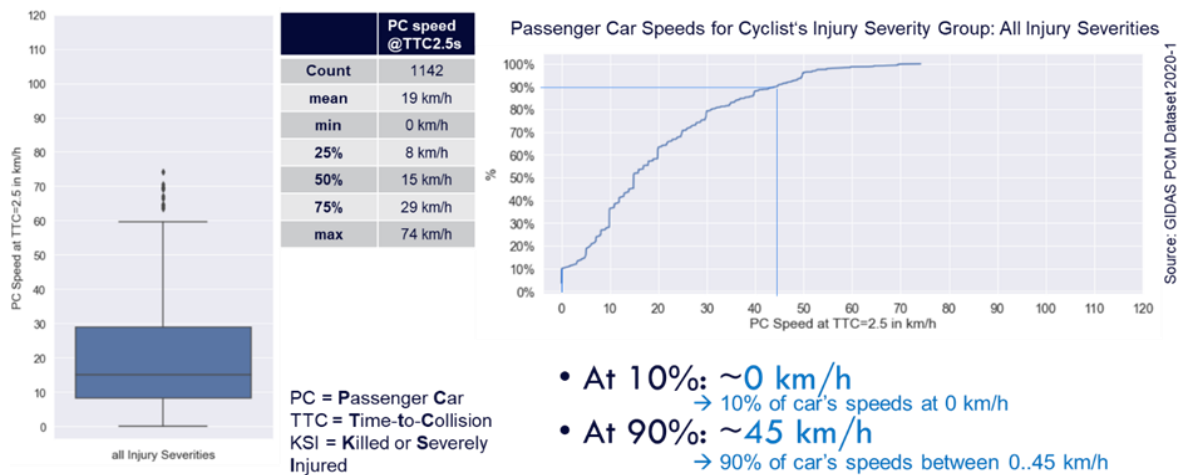


Figure 34: Passenger car speed information for B-CR at TTC=2.5s.



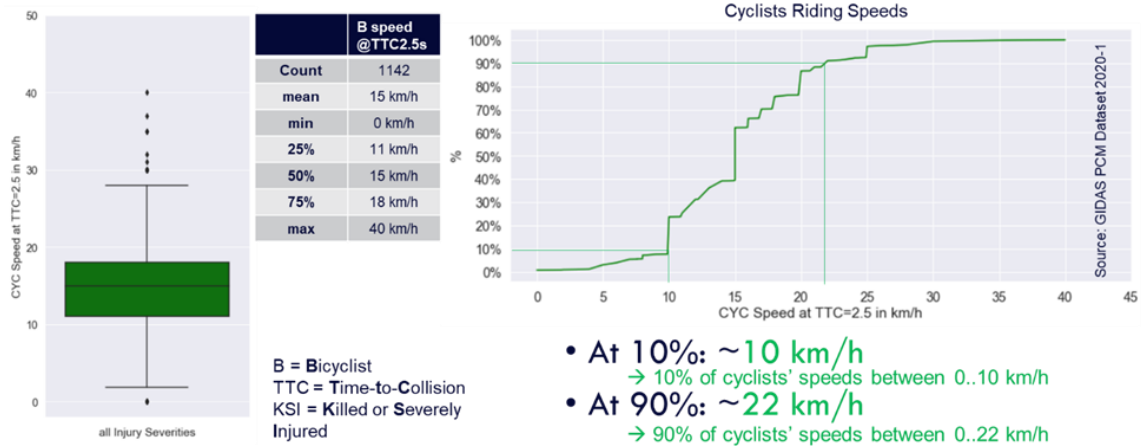


Figure 35: Bicyclist riding speed information for B-CR at TTC=2.5s.

In Table 11 information for all 10 conflict scenarios is given.

Table 11: Passenger car conflicts with bicyclists information.

B.ID	Conflict Scenario	Injury Severity Group	Count	Passenger Car speed information at TTC=2.5s						Bicyclist riding speed information at TTC=2.5s									
				mean in km/h	min in km/h	25% in km/h	50% in km/h	75% in km/h	max in km/h	coverage at 10%	coverage at 90%	mean in km/h	min in km/h	25% in km/h	50% in km/h	75% in km/h	max in km/h	coverage at 10%	coverage at 90%
1	B-CR	All Injury severities	1142	19	0	8	15	29	74	0 km/h	0.45 km/h	15	0	11	15	18	40	0.10 km/h	0.22 km/h
1	B-CR	KSI	278	27	0	10	25	43	74	0.4 km/h	0.50 km/h	-	-	-	-	-	-	-	-
1.a	B-CRwSO	All Injury severities	494	19	0	8	15	29	70	0 km/h	0.40 km/h	16	0	12	15	20	37	0.10 km/h	0.22 km/h
2	B-CL	All Injury severities	782	21	0	10	20	30	102	0 km/h	0.41 km/h	17	0	14	15	20	45	0.9 km/h	0.24 km/h
2	B-CL	KSI	190	29	0	15	26	37	102	0.6 km/h	0.50 km/h	-	-	-	-	-	-	-	-
2.a	B-CLwSO	All Injury severities	272	21	0	10	19	30	100	0 km/h	0.36 km/h	18	2	14	16	20	45	0.10 km/h	0.24 km/h
3	B-LongSD	All Injury severities	161	38	0	23	40	50	103	0.6 km/h	0.60 km/h	16	0	12	15	20	35	0.8 km/h	0.24 km/h
4	B-LongOD	All Injury severities	70	24	0	8	22	35	90	0 km/h	0.46 km/h	17	8	15	17	20	30	0.11 km/h	0.22 km/h
5	B-PCRev	All Injury severities	24	6	0	0	5	9	20	0 km/h	0.14 km/h	12	5	10	12	15	15	0.7 km/h	0.15 km/h
6	B-PCStat	All Injury severities	35	0	0	0	0	0	0	0 km/h	0 km/h	19	5	15	18	20	31	0.13 km/h	0.27 km/h
7	B-PCTurnL	All Injury severities	279	21	0	15	20	26	46	0.10 km/h	0.30 km/h	17	0	12	16	22	49	0.8 km/h	0.27 km/h
8	B-PCTurnR	All Injury severities	338	22	0	15	21	29	65	0.9 km/h	0.36 km/h	18	0	14	17	20	45	0.9 km/h	0.25 km/h

6.2 Scenario selection for simulations with focus on adverse weather conditions

This section details the simulations performed on conflicts between passenger cars and pedestrians to evaluate the impact of adverse weather conditions on intervention functions. The focus of the simulations is on pedestrians and on precipitation as it is significantly more prevalent in crashes with VRUs than other weather phenomena like fog (SAFE-UP, Deliverable report D2.6, 2021).

The main goals of the simulations are to assess the influence of rain on generic AEB (Autonomous Emergency Braking) and AES (Autonomous Emergency Steering) functions using the results of the detection degradations from Deliverable D3.5 (SAFE-UP, Deliverable report D3.5, 2022) and to identify in which scenarios AES functions can provide a benefit over AEB functions.



Scenario cluster selection

The basis for the simulation scenario selection are the identified conflict scenarios between passenger cars and pedestrians from Deliverable D2.6 (SAFE-UP, Deliverable report D2.6, 2021), which are summarized in Table 10.

Due to the low velocities in the reversing cluster (90th percentile at 9.5km/h for the passenger car) and a precipitation share significantly below the baseline precipitation share, the reversing cluster is disregarded for simulations.

Scenario parametrization

For each of the selected scenario clusters, up to 3 simulation configurations with different velocity values are defined. One configuration is simulated with the median velocity values of the passenger car and the pedestrian in the respective cluster at a TTC of 2.5s. In addition, up to two configurations are simulated with sensor critical velocity values of the cluster at a TTC of 2.5s.

In addition to the configuration with median velocities (1), for the crossing scenarios one configuration focuses on the range (2) limitation and one on the opening angle (3) limitation of a sensor as shown in Figure 36.

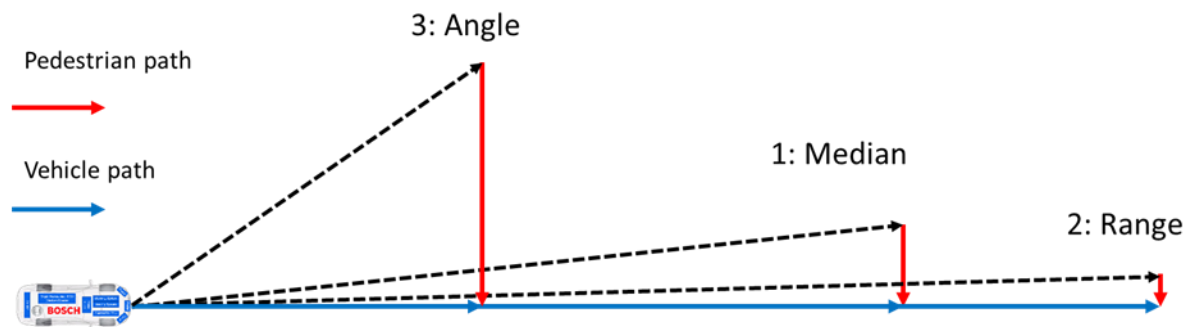


Figure 36: Selected configurations for crossing scenarios.

As for the crossing scenarios the number of accidents is sufficiently large, passenger car velocities are also extracted from the accidents with KSI pedestrians in addition to the accidents with injured pedestrians (see Section 6.1.1). Always the extremer value of both groups is chosen for simulation. The extracted median velocities (1) are marked with red arrows in Figure 37 exemplarily for the cluster CLwoSO.

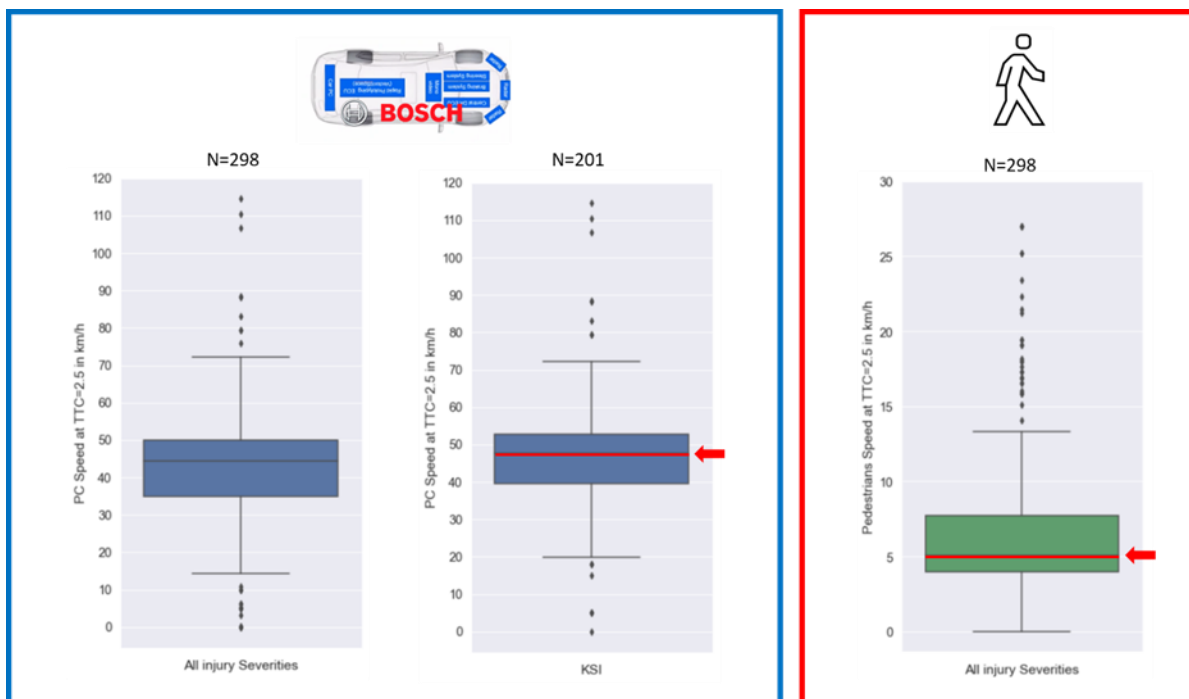


Figure 37: Extracted velocities for the simulation based on median velocities.

For the configuration focusing on range (2), the 90th percentile of the passenger car velocity distribution and the 10th percentile of the pedestrian velocity distribution of the cluster at a TTC of 2.5s is chosen as shown in Figure 38 for the cluster CLwoSO. As the 90th percentile of the passenger car velocities in the group with KSI pedestrians is extremer (higher), this value is chosen for simulation. With the selected high speed of the passenger car and the low speed of the pedestrian, this configuration can identify limitations with respect to the sensor range.

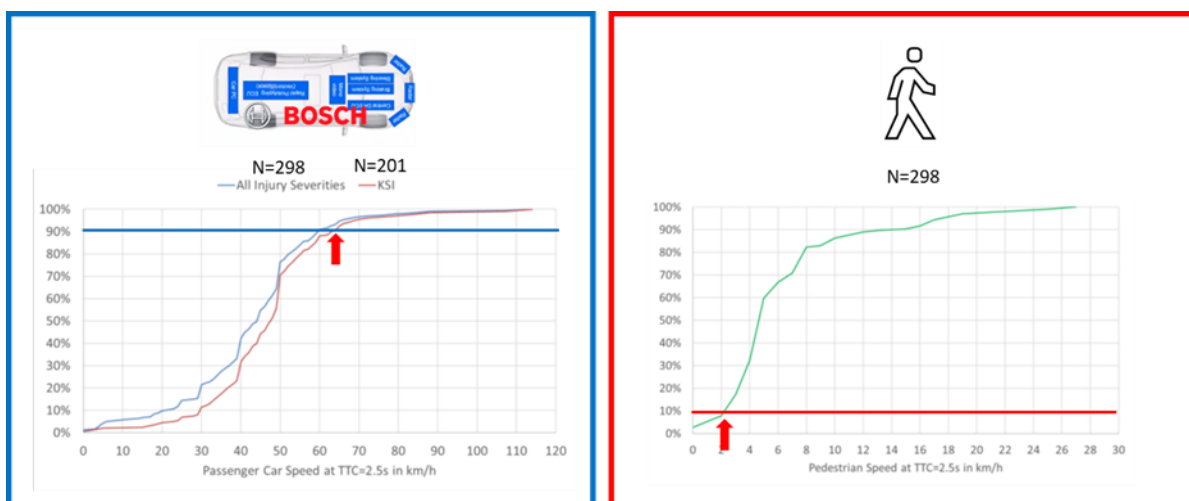


Figure 38: Extracted velocities for the simulation focusing on the sensor range.



For the configuration focusing on the opening angle (3), the 10th percentile of the passenger car velocity distribution and the 90th percentile of the pedestrian velocity distribution of the cluster at a TTC of 2.5s is chosen as shown in Figure 39 for the cluster CLwoSO. As the 10th percentile of the passenger car velocities in the group including all injured pedestrians is extremer (lower), this value is chosen for simulation. By combining a low speed of the passenger car with the high speed of the pedestrian limitations concerning the opening angle of the sensors can be identified.

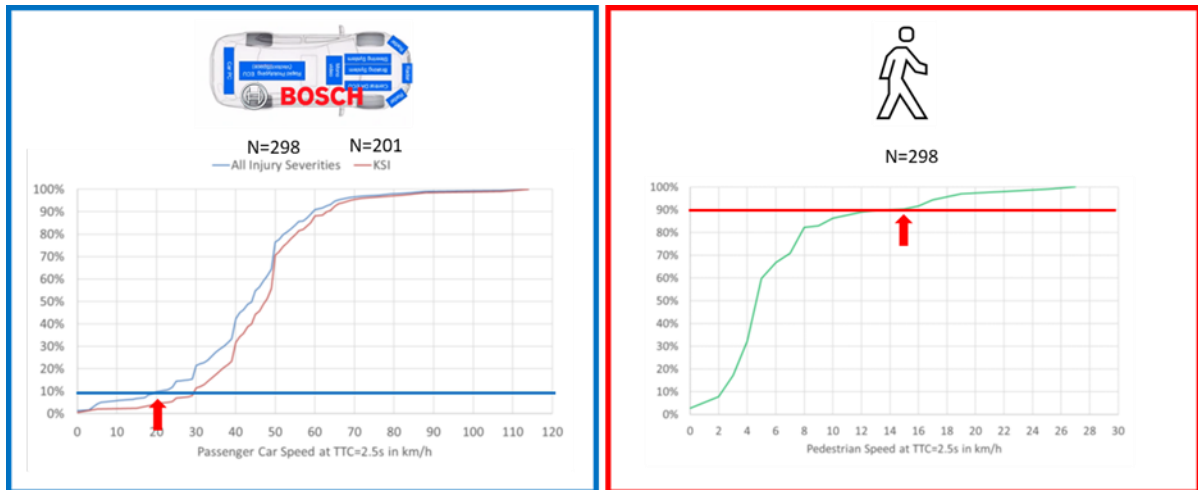


Figure 39: Extracted velocities for the simulation focusing on the sensor opening angle.

For the longitudinal cluster, besides the configuration with median velocities (1) one configuration represents the worst case and one the best case in terms of range as shown in Figure 40. To simulate the worst case (2), the 90th percentile of the passenger car as well as pedestrian velocity distribution is selected and the pedestrian is chosen to run in oncoming direction. To simulate the best case (3), the 10th percentile of the passenger car as well as pedestrian velocity distribution is selected and the pedestrian is chosen to head in the same direction as the passenger car.

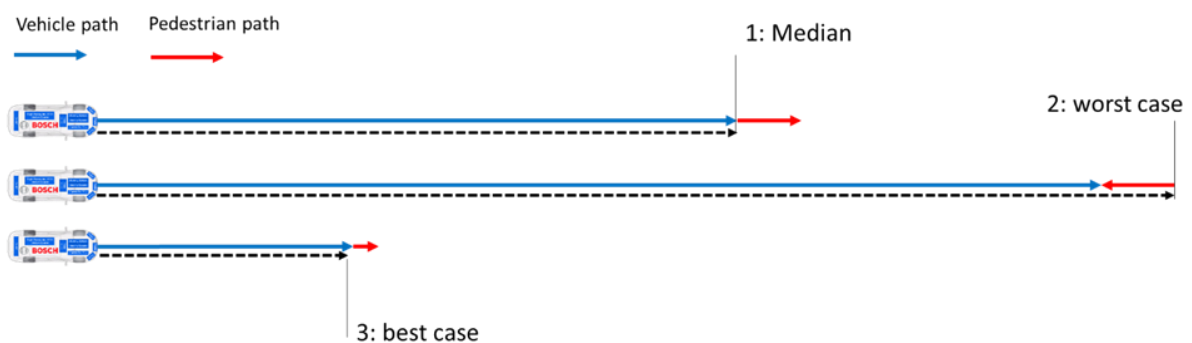


Figure 40: Selected configurations for the longitudinal scenario.



Harmonization with EuroNCAP scenarios

The goal for the simulation is to provide a representative excerpt from the accident events including pedestrians, while limiting the simulation effort for this large database. The selected scenarios are structured in such a way that they can be compared with existing results from other projects.

As the scenarios have also been used by EuroNCAP over the last years, it is reasonable to look at the test matrix from EuroNCAP shown in Table 12 for vehicle to pedestrian crashes.

Table 12: Test matrix from EuroNCAP for Car-to-Pedestrian Scenarios (EuroNCAP, 2022).

	CPFA	CPNA	CPNCO	CPLA		CPTA		CPRA/CPRC			
Section	7.2.1	7.2.2	7.2.3	7.2.4		7.2.5		7.2.6			
Type of test	AEB			AEB	FCW/ESS	AEB		AEB			
VUT speed [km/h]	10-60			20-60	50-80	10,15,20	10	4,8			
VUT direction	Forward			Forward		Farside turn	Nearside turn	Rearward			
Target speed [km/h]	8	5		5	5	5		0	5		
Target direction	Coming from Farside	Coming from Nearside		Forward		Coming from Opposite direction	Coming from Same direction	Coming from Opposite direction	Coming from Same direction	Standing, Direction facing selected by lab	Coming from nearside
Impact location [%]	50	25,75*	50	50	25	50		25,50,75	50		
Dummy Articulation	Yes – as per test speed			Yes		Yes		Articulated dummy in 'off' position	Yes		
Lighting condition	Day/Night			Day/Night		Day		Day			
Vehicle lights (night)	Low beam			High beam		N/A		N/A			
Streetlights (night)	Streetlights			No streetlights		N/A		N/A			

The table provides an overview of the range of possible combinations of vehicle speed (VUT speed) and pedestrian speed (Target speed). In addition to these parameters, for example the impact location or obstruction is also varied. The impact location can also be referred to as the virtual hitpoint as it represents the point in percent with reference to the vehicle width, where the pedestrian would hit the passenger car without intervention.

Linking scenarios from EuroNCAP and Cluster from SAFE-UP

In the following, the scenarios identified in the SAFE-UP project are compared with the test cases of EuroNCAP and evaluated with regard to the similarities. If a similarity between the scenarios can be identified, the test layout of EuroNCAP is used. However, the parameters defining the velocities are used as described in the previous chapter.

The cluster CLwoSO corresponds to the Car-to-Pedestrian Farside Adult (CPFA) and CRwoSO corresponds to the Car-to-Pedestrian Nearside Adult (CPNA) test case of EuroNCAP. In these scenarios, an adult is tested who crosses the road from the right or left. For the cluster CLwoSO the virtual hitpoint at 50% is used and for the cluster CRwoSO the virtual hitpoint at 25% is selected, as this is the more critical case for the sensor.



For the CLwSO scenario, the EuroNCAP test case Car-to-Pedestrian Farside Adult (CPFA) has to be supplemented with a visual obstruction. For the CRwSO scenario a corresponding cluster from EuroNCAP exists, namely Car-to-Pedestrian Nearside Child Obstructed (CPNCO), which is used for the definition of the obstruction and the virtual hitpoint. However, for all simulations only adult pedestrians are used as the sensor tests described in (SAFE-UP, Deliverable report D3.5, 2022) were performed with adult targets and the speeds are taken anyway from the accident analysis.

For the longitudinal cluster the comparable scenario is the Car-to-Pedestrian Longitudinal Adult (CPLA). In order to achieve a variation here, the simulation of the pedestrians is set in the same direction and in the opposite direction of vehicle movement. This means evaluating the sensor under the shortest and longest sensor view. For the simulation focusing on the longest sensor view, the virtual hitpoint at 25% is used, and for the other simulations the virtual hitpoint at 50%.

The turning clusters with the four different direction configurations correspond to the Car-to-Pedestrian Turning Adult (CPTA) test cases of EuroNCAP and therefore, the directions and virtual hitpoints are selected as defined there.

As the reversing cluster is not of focus in the simulations, the corresponding scenario Car-to-Pedestrian Reverse Adult/Child moving (CPRA/C) is not considered.

In Table 13, the defined configurations for the simulations including the corresponding EuroNCAP scenario, the velocities, the virtual hitpoints and the layouts are summarized. The selected velocities are marked in each line in bold.



Table 13: Simulated configurations, which are harmonized with EuroNCAP test cases.

Safe-UP ID.Number	Cluster	Category	EuroNCAP Scenario	Simulation Scenario	v_ego kph	v_ego kph2	v_traget kph	Virtual Hitpoint	Obstruction
					All injury severities	KSI	All injury severities		
1a	P-CLwoSO	Median	CPFA	CPFA	45	48 (V0)	5	50% (ENCAP)	no
1b	P-CLwoSO	Range	CPFA	CPFA	60	63 (V1)	2	50% (ENCAP)	no
1c	P-CLwoSO	Angle	CPFA	CPFA	21 (V2)	30	15	50% (ENCAP)	no
2a	P-CLwoSO	Median	CPFA	CPFAO	35	40 (V0)	6	50% (ENCAP Nearside)	ENCAP modified
2b	P-CLwoSO	Range	CPFA	CPFAO	50	52 (V1)	1	50% (ENCAP Nearside)	ENCAP modified
2c	P-CLwoSO	Angle	CPFA	CPFAO	19 (V2)	24	16	50% (ENCAP Nearside)	ENCAP modified
3a	P-CRwoSO	Median	CPNA	CPNA	40	45 (V0)	5	25% (ENCAP, Sensor critical)	no
3b	P-CRwoSO	Range	CPNA	CPNA	54	58 (V1)	2	25% (ENCAP, Sensor critical)	no
3c	P-CRwoSO	Angle	CPNA	CPNA	14 (V2)	17	13	25% (ENCAP, Sensor critical)	no
4a	P-CRwoSO	Median	CPNCO	CPNAO	35	40 (V0)	6	50% (ENCAP)	yes
4b	P-CRwoSO	Range	CPNCO	CPNAO	51	55 (V1)	3	50% (ENCAP)	yes
4c	P-CRwoSO	Angle	CPNCO	CPNAO	19 (V2)	24	15	50% (ENCAP)	yes
5a	P-Long	Median	CPLA	CPLA	50 (V0)		5	50% (ENCAP)	no
5b	P-Long	Range opposite dir.	CPLA	CPLA	79 (V1)		6	25% (ENCAP)	no
5c	P-Long	Range same dir.	CPLA	CPLA	20 (V2)		2	50% (ENCAP)	no
71a	P-PCTurnL-SD	Median	CPTA	CPTA-L	24 (V0)		5	50% (ENCAP)	no
72a	P-PcTurnL-OD	Median	CPTA	CPTA-L	20 (V1)		5	50% (ENCAP)	no
81a	P-PcTurnR-SD	Median	CPTA	CPTA-R	20 (V2)		4	50% (ENCAP)	no
82a	P-PCTurnR-OD	Median	CPTA	CPTA-R	17 (V3)		5	50% (ENCAP)	no

Implementation of detection and intervention functions

For deciding if the pedestrian is detected at a certain relative position to the passenger car, the results of the second measurement campaign are used, where tests were conducted with the Demo 3 vehicle equipped with a radar and a video sensor. The sensor specifications thereof are described in the Deliverable D3.9 (SAFE-UP, Deliverable report D3.9, 2022) and the test and evaluation methodology for the generation of the FoVs of the investigated sensors in the Deliverable D3.5 (SAFE-UP, Deliverable report D3.5, 2022). The resulting FoVs from this methodology shown in Figure 41 for the radar and video sensor are therefore sensor-specific and depend on the methodology from Deliverable D3.5, which is why the results cannot be generalized.



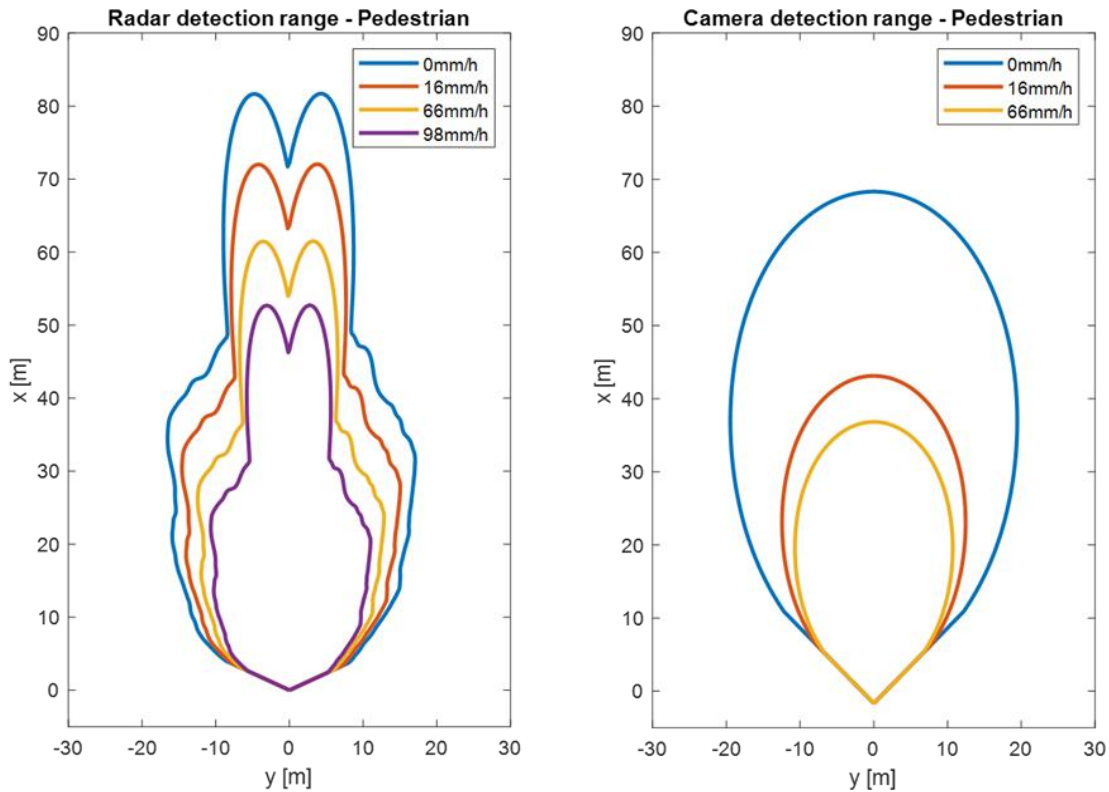


Figure 41: Resulting FoVs from the second measurement campaign, which are sensor-specific and depend on the methodology from (SAFE-UP, Deliverable report D3.5, 2022).

These FoVs are integrated into the simulations to define the area where the pedestrian can be detected by the vehicle with the radar sensor or the video sensor. The radar sensor FoVs are available for 0mm/h, 16mm/h, 66mm/h and 98mm/h and the video sensor FoVs are available for 0mm/h, 16mm/h and 66mm/h, as for 96mm/h no reliable prediction was ensured. In addition to the rain influence modelled by adapting the FoVs, the friction coefficient is adapted in the simulations in correspondence with the rain intensity as summarized in Table 14. The basis for determining an appropriate relating friction coefficient are the results from (Park, Jeong, Jang, & Hwang, 2015), where friction coefficients are given ranging from dry to icy tarmac.

Table 14: Selected friction coefficients for the tested rain intensities.

Rain intensity	Friction coefficient
0mm/h	0.9
16mm/h	0.8
66mm/h	0.6
96mm/h	0.4



Two possible intervention maneuvers are implemented in simulations with AEB (Autonomous Emergency Braking) and AES (Autonomous Emergency Steering) functions, which are performed using generic algorithms. The braking for the AEB function is performed with maximum deceleration and without a change in lateral movement (no steering). Assuming constant acceleration, (Ackermann, Isermann, Min, & Kim, 2014) uses the braking time

$$T_{brake} = \frac{v_{dx}}{2 \cdot a_{brake}}. \quad (7)$$

A constant factor of 0.7s is added, which is aligned with results from simulations. It should take into account that a time is required for the signal transmission, the algorithm triggering, the brake delay as well as that the vehicle should stop with a safety distance to the pedestrian, resulting in the modified braking time of

$$T_{brake} = \frac{v_0}{2 \cdot 0.9g} + 0.7s. \quad (8)$$

The dependency of the braking distance on the road friction and the rain rate is not considered in the estimate of T_{brake} , but different braking distances will occur due to the adapted road friction coefficients.

The steering in the AES function is performed in-lane without a change in longitudinal movement (no braking). To determine the time required for an emergency steering maneuver, several in-lane AES simulations in CarMaker were performed using the default IPG CarMaker steering maneuver with a chosen track offset to ensure in-lane maneuvers. These showed that the vehicle under test needs approximately 1.9s to reach the lateral offset, resulting in the constant steering time of

$$T_{steer} = 1.9s. \quad (9)$$

For all simulated scenarios the lateral velocity before the triggering of the steering maneuver is always zero and it needs the same time for the lateral offset. Due to that the time required for steering is independent of the vehicle velocity.

Intervention decision and trigger timing

The decision to intervene with the AEB or AES function is taken on the basis of three simulation values: TTC, T_{brake} and T_{steer} . All three values are inferred as soon as the pedestrian enters the FoV of the selected sensor. The TTC is calculated for each time step in the clusters with straight movement by assuming constant linear movement for the vehicle and pedestrian and in clusters with a turning vehicle by extracting the collision time from the simulation without intervention.

The possible intervention maneuver strongly depends on the road geometry, the position of the participants and the vehicle maneuver. For instance, it is due to the size of the vehicle and the lane not possible to circumvent a pedestrian who is hit in the middle of the lane (see Section 6.3 for details). Moreover, for simplification steering maneuvers are only allowed in these simulations during straight driving maneuvers. While the required time for the braking maneuver (8) depends on the velocity of the vehicle, the steering time (9) has a constant value of 1.9s.



The decision tree for an AEB or an AES function is shown in Figure 42: In the first step it is decided if steering is possible as an intervention maneuver or not based on the road layout and the position of the participants. If emergency steering is possible, the time required for the evasive steering maneuver is compared to the time required for the braking maneuver. When the calculated time of the braking maneuver is smaller than or equal to the time of the steering maneuver, braking is favored as an intervention function and triggered as soon as the calculated TTC is equal to or smaller than the calculated time for braking T_{brake} . If the calculated time of the braking maneuver is larger than the time of the steering maneuver, it is decided to use the emergency steering intervention, which is triggered when the calculated TTC is equal to or smaller than the calculated time for steering T_{steer} .

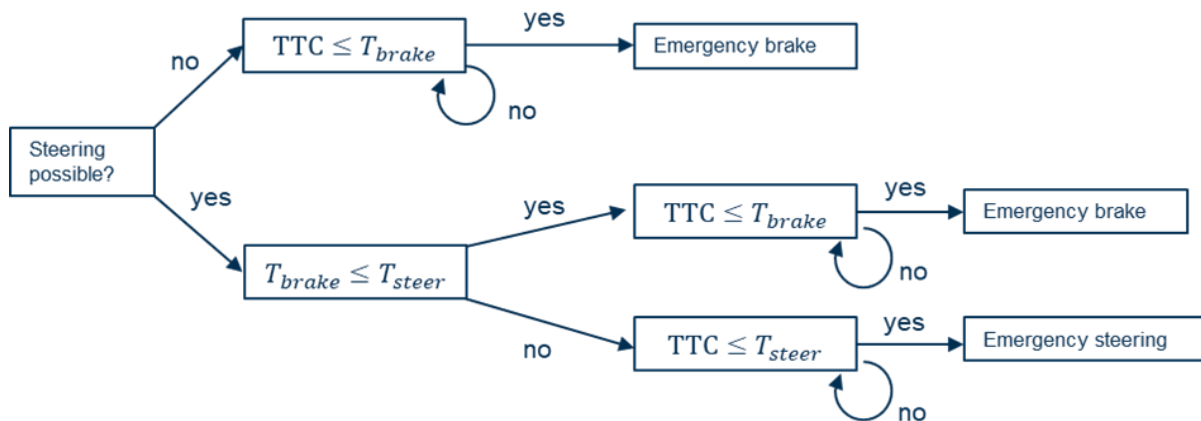


Figure 42: Decision tree for an emergency brake or an emergency steering as an intervention function.

6.3 Description of simulation setup

Simulation setup - input

In order to obtain results from the simulation that are as reliable as possible and that meet the requirements of accident analysis, some parameters of the simulation setup must be defined in advance.

As the vehicle model, the standard IPG vehicle model from CarMaker is used, whereof all parameters and properties are predefined. Certain properties such as brake characteristics and steering characteristics are defined specifically in the project for simulation and can be requested from the CarMaker vehicle model. Within this framework, they follow the requested parameters and are limited only by the maximum ranges of the CarMaker model.

The different clusters from accident research are simulated both with the radar and with the video sensor, which is why the position of the sensors must be taken into account. The simulations were performed individually for both sensors and no fusion system was considered. The installation location of both sensors is shown in Figure 43 for the two sensors.



The video sensor is installed at 2.3m and the radar sensor at 4.0m distance starting from the vehicle’s origin marked with a red cross at the back.

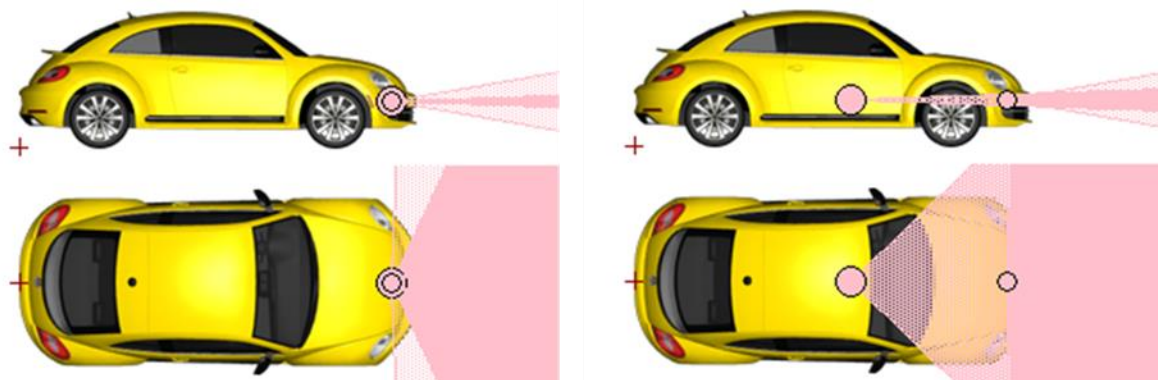


Figure 43: Positioning of the sensors in the IPG vehicle.

As described in Section 6.2, FoVs for the radar were generated for the rain intensities 0mm/h, 16mm/h, 66mm/h, and 98mm/h and for the video sensor for 0mm/h, 16mm/h and 66mm/h. The integration of the FoVs into simulations is shown in Figure 44, which is implemented with a script that can read in data in the format of opening angle and corresponding range values and that can display the sensors in the simulation based on this input. As rain affects besides the field of view also the friction coefficient, this value is as well adapted based on the values from Table 14 via the friction parameter in the IPG-Roadfile.

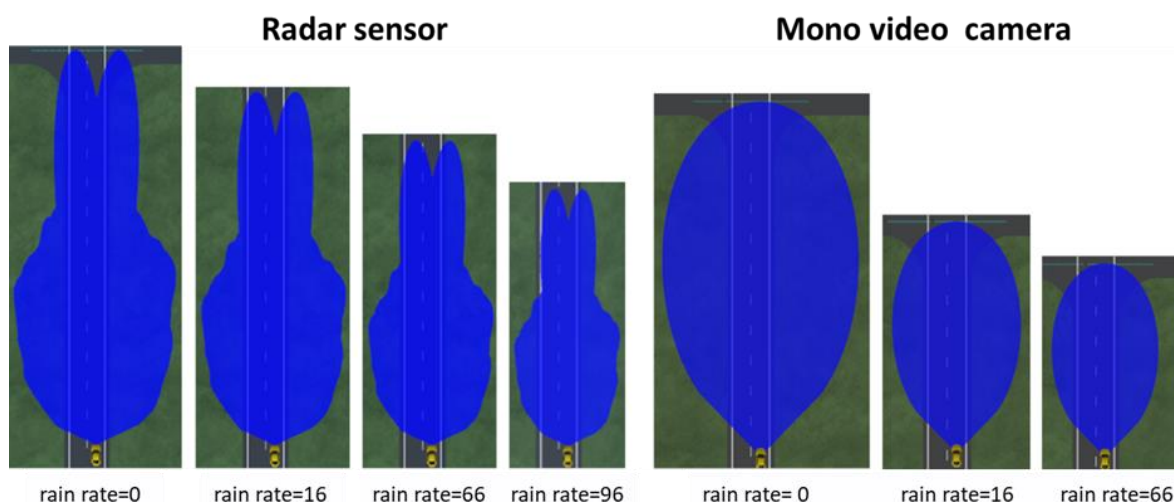


Figure 44: Adapted FoVs integrated into CarMaker.

As described in Section 6.2, occlusion scenarios are also required in the simulations. In harmonization with the test setup from EuroNCAP, the occlusions are generated with stationary vehicles. The distance between the driving and the parking vehicles is 1m and the pedestrian moves past the vehicle at a distance of 1m to the vehicle as illustrated in Figure 45 for the scenario CRwSO.



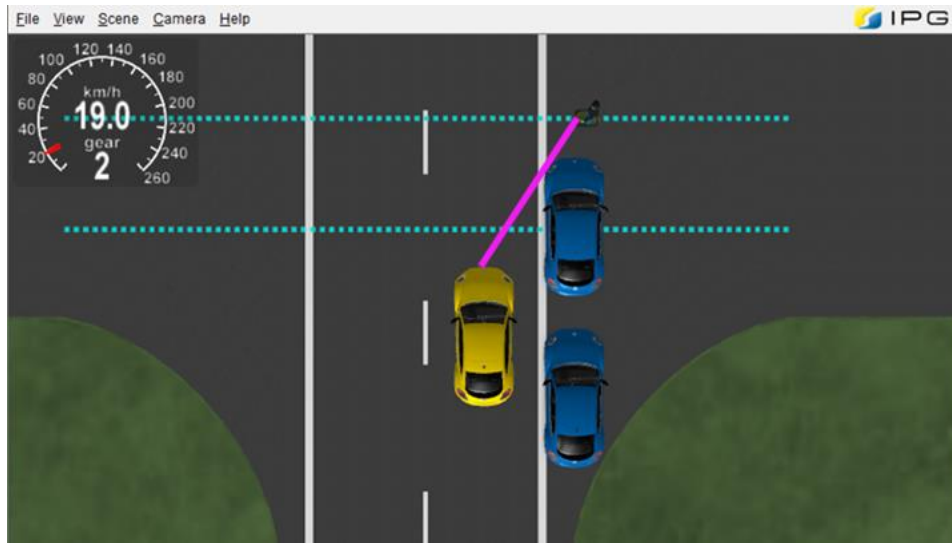


Figure 45: Setup how the occlusion scenarios are modelled in CarMaker.

The pedestrian coming from the right is hidden at larger distances and cannot be detected by the sensor. The earliest point at which the pedestrian can be theoretically detected is marked with a pink line. From this point, the object detection time of the sensor begins as soon as the pedestrian is 500ms within the FoV of the sensor under investigation. For the scenario CLwSO, the distances are defined similarly, however, the parking vehicles are then on the left lane.

As also emergency steering is implemented as a possible intervention maneuver, the dimensions of the road width and the objects need to be defined. The width of the lane including lane markings is defined as 3.9m (lane width + lane markings: 3.5m + 0.15m + 0.25m - maximum values from EuroNCAP (EuroNCAP, 2022)), the width of the vehicle as 2.1m (width including the side mirrors: 1.8m + 2*0.15m - from IPG CarMaker vehicle specification), the width of the pedestrian as 0.33m in the crossing scenarios (step width - from IPG CarMaker pedestrian specification), and the width of the pedestrian as 0.55m in the longitudinal scenarios (shoulder width - from IPG CarMaker pedestrian specification) as shown in Figure 46 for a longitudinal scenario example. It is assumed that steering as an evasive maneuver is in general possible if the available space between the pedestrian and the left lane including the lane marking is larger than or equal to the vehicle width.





Figure 46: Definition of the different width, which are required for evasive steering.

Simulation setup - output

To evaluate the results of the simulations, several output parameters were extracted besides the parameters defining the simulation setup, which include the passenger car and pedestrian velocity, the virtual hitpoint in relation to the passenger car, the rain rate as well as the friction coefficient.

For each simulation, the time required for intervening with steering (T_{steer}) and braking (T_{brake}) is extracted, which is calculated using (8) and (9). Thereby, the values under nominal conditions are estimated, which are used for the decision of the intervention type as described in Figure 42. The resulting intervention type is also extracted for each simulation such that it can be evaluated if braking or steering is preferable in certain scenario types.

In addition, the TTC at which the object is detected is extracted ($T_{detected}$), which is defined by the time at which the pedestrian is 500ms in the FoV of the investigated sensor. It is assumed that 500ms are required for the sensor detection and the signal transmission after the pedestrian initially enters (nearest point) the FoV. For each scenario also the TTC at which the intervention is triggered ($T_{intervention}$) is stored. It is equal to the minimum of the variables $T_{detected}$, T_{brake} , and T_{steer} . The smaller T_{brake} or T_{steer} value decides the chosen intervention maneuver. If the pedestrian is detected sufficiently early, the intervention is triggered when the TTC value is equal to the time required for the braking or steering maneuver (case $T_{intervention} = T_{brake}$ or $T_{intervention} = T_{steer}$). If the pedestrian is detected later than the



intervention maneuver would take, it is triggered as soon as the pedestrian is detected (case $T_{intervention} = T_{detected}$).

For the cases where the intervention function cannot avoid a collision, a parameter is used, which is set from 0 to 1 in the case of a collision (collision), and the collision speed ($v_{collision}$) is extracted, which indicates the residual speed of the passenger car with which it hits the pedestrian. In simulations where the selected intervention maneuver is braking but a collision cannot be avoided, the collision speed is correspondingly lower than the initial speed of the passenger car depending on the time of triggering. In simulations where the chosen intervention maneuver is steering but a crash cannot be avoided, the collision velocity is equal to the initial passenger car velocity as it is not combined with braking.

6.4 Results

This chapter details the evaluation results of the performed simulations of the scenarios described in Section 6.2. First, a general analysis is conducted and then the clusters are analyzed individually with the focus on the influence of the detection type and the rain rate. Subsequently, the most important findings are summarized.

6.4.1 Overview

The number of simulated cases in the crossing and longitudinal scenarios is 21 each, consisting of nine cases with camera detection and 12 cases with radar detection (see Figure 47). The nine cases with camera detection result from three velocity configurations V0, V1 and V2, varied with three rain intensities (0mm/h, 16mm/h and 66mm/h). The mapping from the velocity configurations Vx to the actual velocity values are given in Table 13 for all scenarios. The 12 cases with radar detection result from three velocity configurations V0, V1 and V2, varied with four rain intensities (0mm/h, 16mm/h, 66mm/h, and 96mm/h). The deviation results from the observation that camera detection is no longer possible at the highest rain rate and is therefore not simulated.

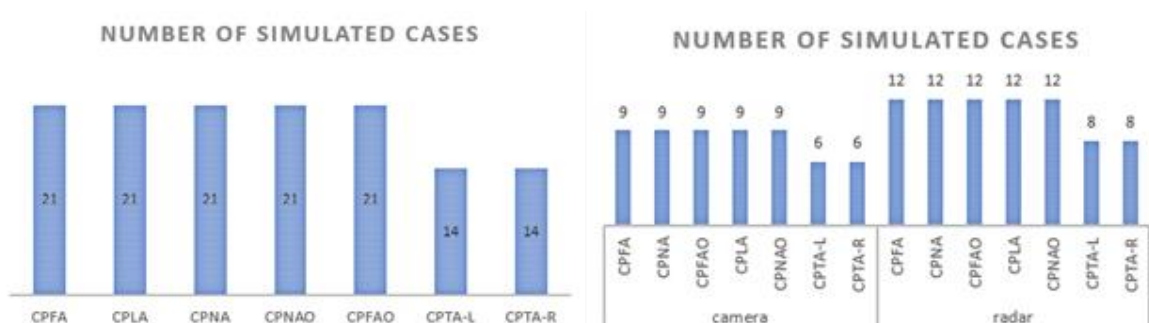


Figure 47: Numbers of simulated cases.



The number of turning scenarios to the left and to the right each consist of six cases with camera detection and eight cases with radar detection. These consist of two median velocities to the left (V_0 and V_1) and two median velocities to the right (V_2 and V_3) each with a same-directed and an oncoming target, varied with three or four rain intensities, respectively (see Figure 47).

Of the 21 cases in each of the longitudinal and crossing scenarios and the 14 cases in each of the turning scenarios, i.e. a total of 133 cases, braking intervention was preferred to steering intervention in 126 cases (see Figure 48). Steering intervention was the prevailing choice in only seven cases in the longitudinal scenario CPLA, where in three camera-based and four radar-based scenarios the steering time (T_{steer}) was smaller than the braking time (T_{brake}).

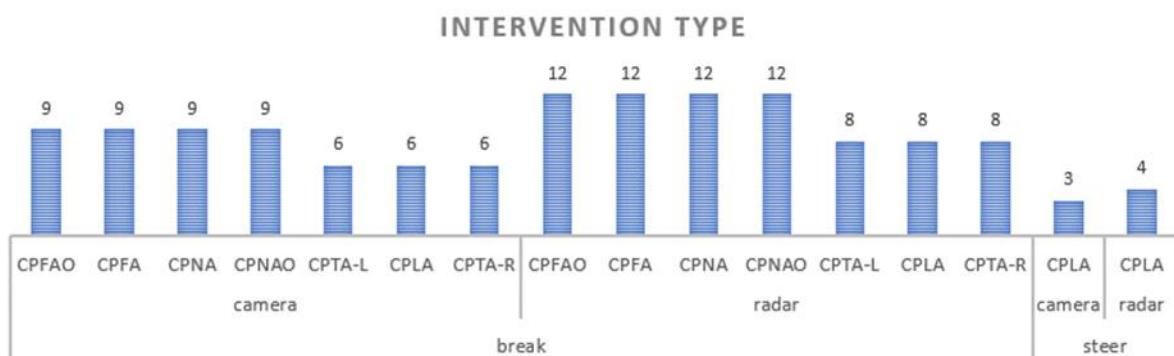


Figure 48: Intervention type per scenario.

The number of collisions shows that the proportion with collisions predominates in scenarios with obstruction (see Figure 49). The obstruction causes delayed detections, which lead to a significant limitation of the avoidance potential. The reason for the high number of collisions is especially that all rain rates from 0mm/h to 96mm/h are included in this evaluation. It can also be observed that for the nearside crossing pedestrian, CPNAO, the visual obstruction directly next to the driving trajectory leads to more collisions than for the farside crossing pedestrian, CPFAO. The ego velocities of both scenarios are comparable, which allows this conclusion.

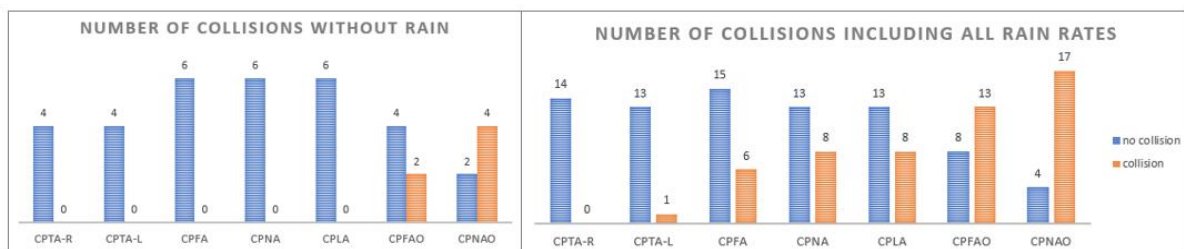


Figure 49: Number of collisions per scenario.



In general, it can be observed that collisions occur in almost every scenario. Turning right is the exception here with none and turning left with one collision.

Both braking and steering intervention lead to collisions (see Figure 50).

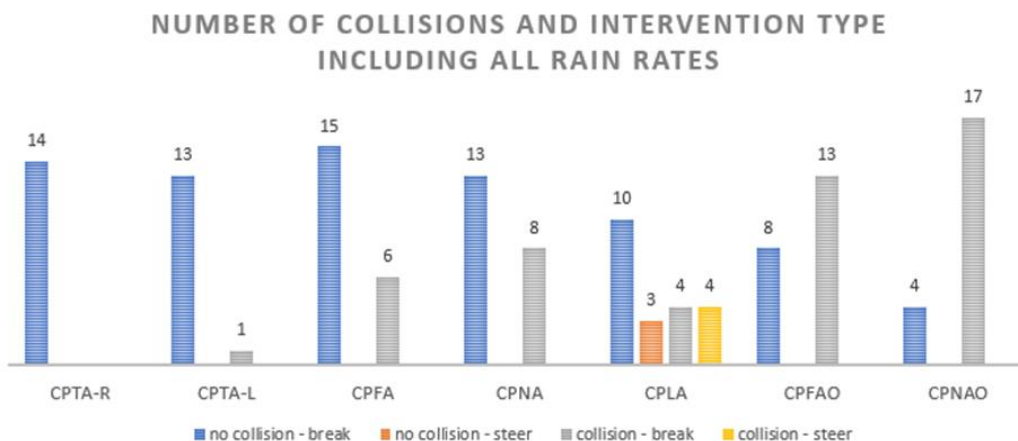


Figure 50: Number of collisions per scenario depending on intervention type.

The number of collisions, taking into account the rain rate, shows a clear trend (see Figure 51). Regardless of the detection type, camera or radar, the number of collisions increases with higher rain rates. If 16% collisions occur with no precipitation, the proportion rises to 26%/21% at 16mm/h. At 66mm/h the proportion of collisions is then 63% and at 96mm/h (radar) 74%.

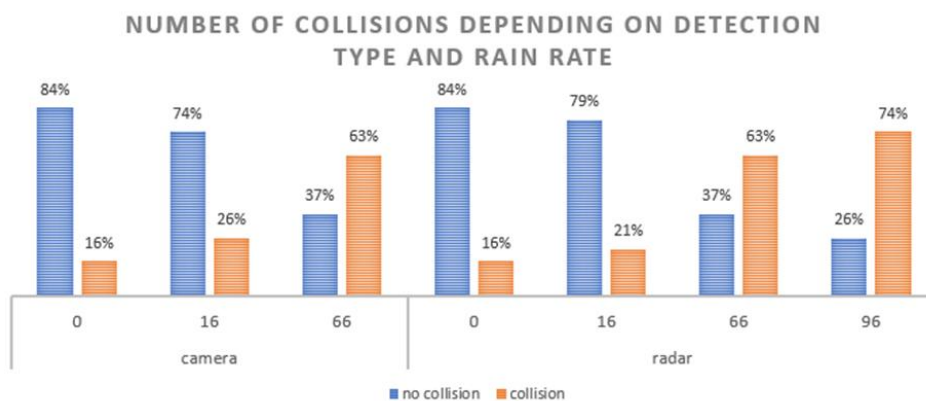


Figure 51: Number of collisions depending on rain rate (0mm/h, 16mm/h, 66mm/h, and 96mm/h).



6.4.2 Results per scenario

In the following subsections, structured by scenario, the influence of the detection type and the rain rate is discussed. Furthermore, it is analyzed what is the cause of the collisions and respectively the dependence of the collisions on T_{steer} , T_{brake} , $T_{detected}$, and $T_{intervention}$.

6.4.2.1 CPFA

In the CPFA scenario, no dependence of the detection type on the number of collisions is observed (see Figure 52).

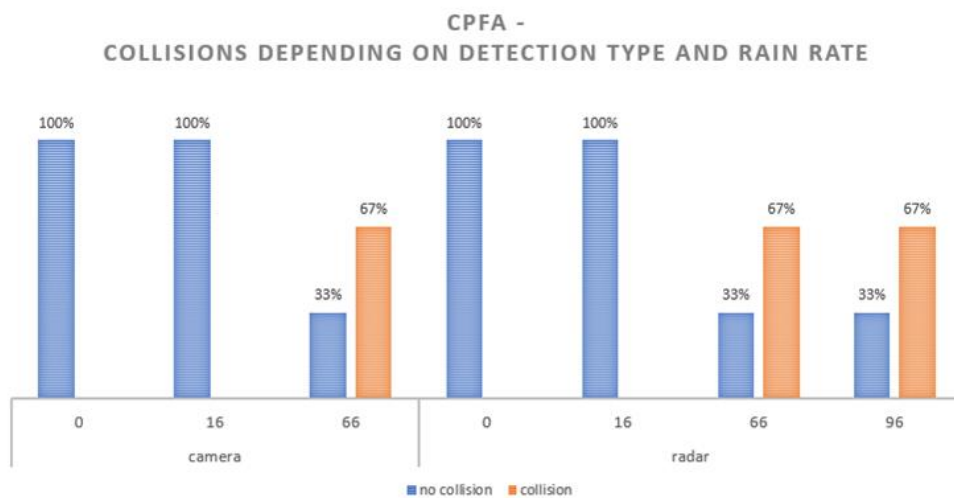


Figure 52: CPFA – Percentage of collisions depending on detection type and rain rate.

At 0 mm/h rain rate, all simulated cases are avoided. The influence of 16mm/h rain rate shows no effect, all simulated cases are still avoided. At 66mm/h and 96mm/h (radar only) rain rate, in 67% of the simulated cases collisions then occur.

In Figure 53 it can be observed that the time T_{steer} is independent of the speed of the vehicle. It is constant at 1.9s. The braking time varies and increases as the ego speed of the vehicle increases. For example, a braking time of 1.69s must be selected at an ego speed of 63km/h (V1 – focus range) to avoid collision with a pedestrian crossing from the left, while a braking time of 1.03s is required at an ego speed of 21km/h (V2 – focus opening angle). For all three speed configurations (V0 – median, V1 – focus range, V2 – focus opening angle), T_{brake} is smaller than T_{steer} , so the braking maneuver is preferred.



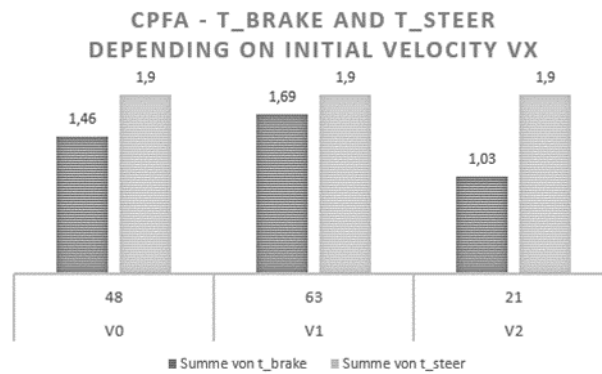


Figure 53: CPFA – T_{brake} and T_{steer} depending on initial velocity V_x .

Another influencing factor is the detection time at which the object is detected by the sensor. As shown in Figure 54, this depends on the detection type - camera or radar - as well as on the rain rate. For example, with radar detection, a rain rate of 0mm/h, and an ego speed of 48km/h (V_0 – median) the pedestrian is already detected at a TTC of 5.1s, while the camera detects it at 4.5s. In general, the radar is more likely to detect the pedestrian over all rain rates and ego speeds earlier.

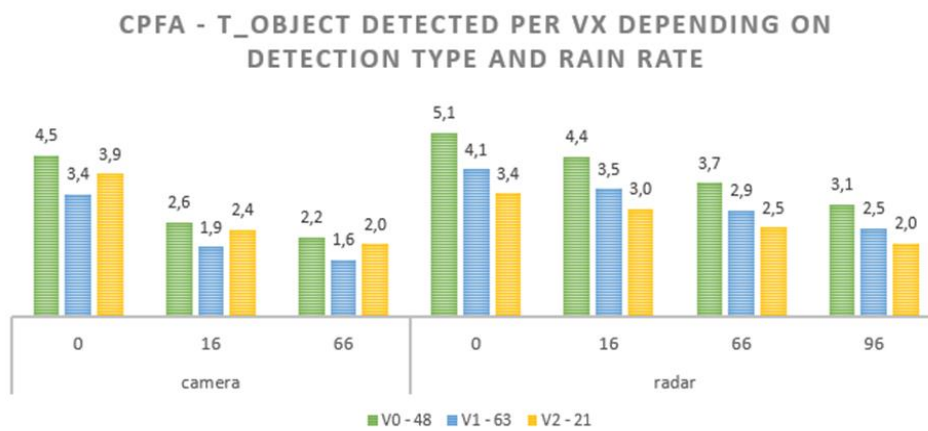


Figure 54: CPFA – $T_{detected}$ per V_x depending on detection type and rain rate.

An exception is perceivable at 21km/h ego speed and 15km/h target speed (V_2 – focus opening angle) and 0mm/h rain rate. Here the camera detects the pedestrian earlier than the radar. This phenomenon can be explained by the fact that at high ego speeds and low target speeds (V_0 – median and V_1 – focus range), the target enters the detection area frontally. At low ego velocities and high target velocities, however, the target enters the lateral boundary of the FoV (see Figure 55). With frontal detection, the radar always detects the object earlier due to its longer detection range to the front. With lateral detection and 0mm/h rain rate, the



FoV of the camera is wider in the x-direction towards the front, which means that the object is more likely to be detected by the camera in this case. At higher rain rates, however, the width of the FoV decreases so that it is approximately comparable to that of the radar.

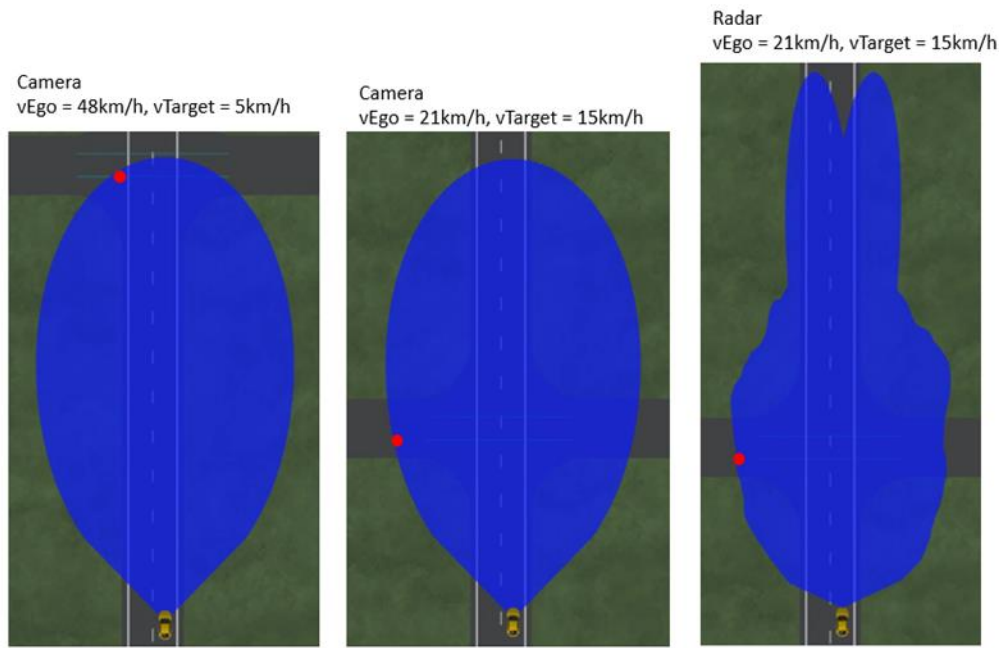


Figure 55: Detection characteristics based on detection type and velocities shown at first entry point into the FoV.

For frontal detection, i.e. V0 (median) and V1 (focus range), the detection time decreases with increasing ego velocity.

The influence of the rain rate can be seen in both camera and radar detection as the detection time decreases with increasing rain rate. A significant difference in the reduction of detection time between radar and camera is seen when the rain rates of 0 and 16mm/h are compared. Here, the camera detection time degrades by up to 45%, while the radar detection time decreases by only 15%. When the rain rate is increased from 16 to 66mm/h, both degrade by another 15% in relation to the rain rate before.

In order to make a statement about which detection times restricted by the rain rates have an influence on the scenario in terms of a resulting collision, the detection time is compared with the shortest intervention time per ego speed (either braking or steering) as a function of the rain rate and the detection type (see Figure 56). In the following, only the collisions that are caused by the influence of the rain rate are discussed. In the CPFA scenario, these are all those with a rain rate of 66mm/h or higher.



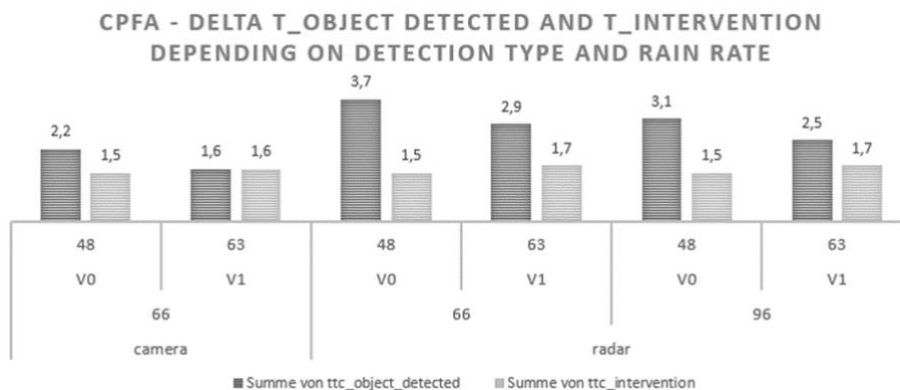


Figure 56: CPFA – $T_{detected}$ and $T_{intervention}$ depending on detection type and rain rate.

The collision at e.g. the camera detection, 66mm/h rain rate and an ego speed of 48km/h (V0 – median) results from the reduced friction value compared to 0mm/h. As explained, this is not included in the calculations of the required intervention time.

If the detection time (2.2s) is higher than the intervention time (1.5s), it is possible to reduce the residual collision speed within T_{delta} by 2.2s minus 1.5s, i.e. 0.7s. In this case, the residual collision speed is 13.7km/h (see Figure 57). Collision avoidance would be possible here with a deceleration of 6m/s² (rough calculation: 0.7s*6m/s²*3.6=15.12km/h). The later detection time is the cause of the collision here, but could potentially be compensated by an earlier emergency braking.

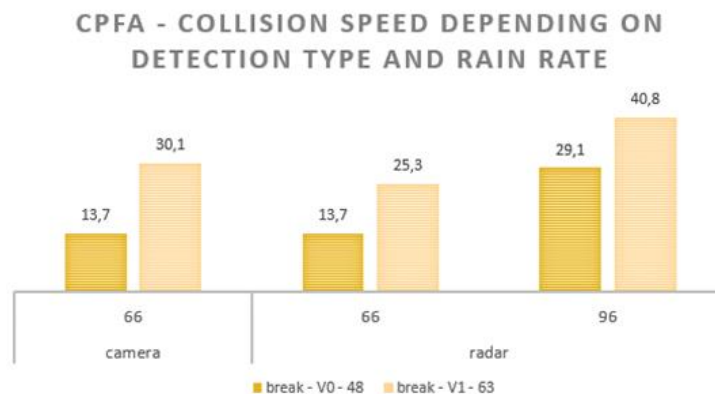


Figure 57: CPFA – Collision speed depending on detection type and rain rate.

In the collision case with V1 (ego speed 63km/h, target speed 2km/h, focus range), 66mm/h, and camera detection, however, there is no difference between the detection time and the intervention time. The later detection time due to the precipitation intensity and the associated



limited FoV is therefore the cause of the collision and can no longer be compensated by an earlier system intervention. The result is a collision at 30km/h.

In case with V0 (median) and radar detection, the collision would be avoidable within T_{delta} 2.2s due to the less restricted FoV and thus earlier detection by an earlier braking intervention. Also, in case V1 (focus range) with 63km/h ego speed and 2km/h target speed this potential would exist.

At 96mm/h rain rate and both cases V0 (median) and V1 (focus range), the collision velocity could be significantly reduced.

Figure 58 shows the respective T_{delta} and the remaining residual velocity per detection type, precipitation intensity and ego velocity. Based on this, the cases with collision are identified, which have an avoidance or mitigation potential with an earlier emergency braking or steering, or which are limited by a late detection due to obstructions.

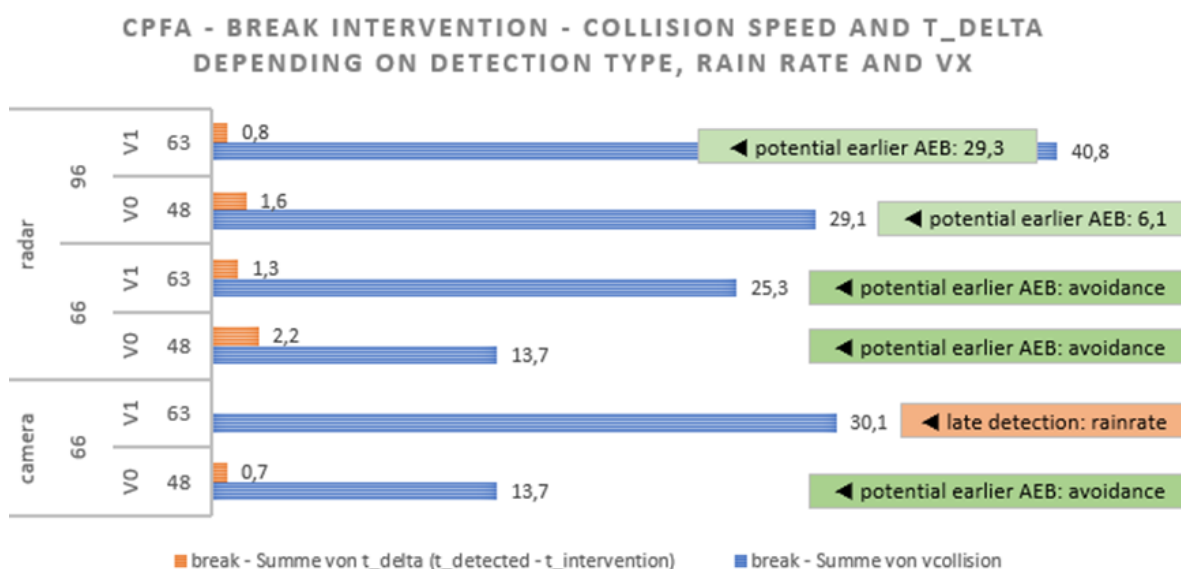


Figure 58: CPFA – Break intervention – collision speed and T_{delta} depending on detection type, rain rate and V_x .

6.4.2.2 CPFAO

In the CPFAO scenario, no dependence of the detection type on the number of collisions is observed (see Figure 59).

At 0 and 16 mm/h rain rate in 33% of the simulated cases collisions occur. The influence of 16mm/h rain rate shows no influence. Then at 66mm/h and 96mm/h (radar only) rain rate in 100% of the simulations collisions occur.



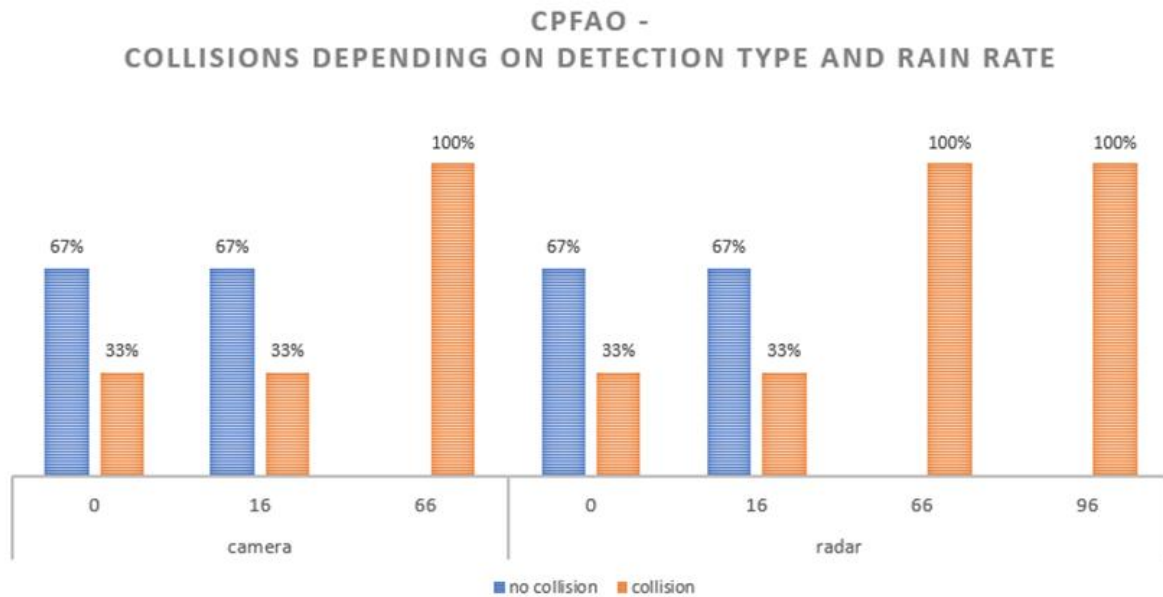


Figure 59: CPFAO – Percentage of collisions depending on detection type and rain rate.

In Figure 60 it can be seen that the time T_{steer} is independent of the speed of the vehicle. It is constant at 1.9s. The braking time varies and increases with increasing ego speed (V_x). For all three speeds (V_0 – median, V_1 – focus range, V_2 – focus opening angle), T_{brake} is smaller than T_{steer} , which is why the braking maneuver is preferred here as well.

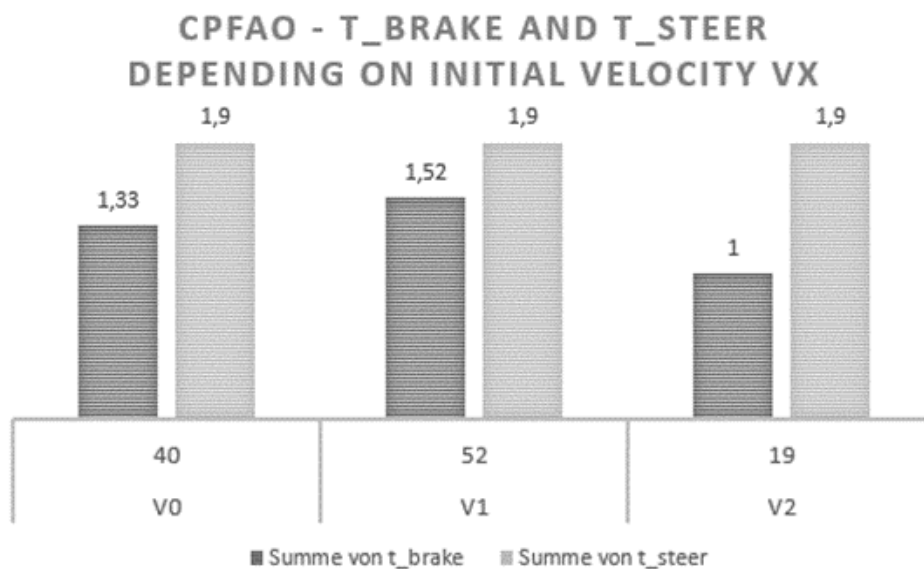


Figure 60: CPFAO – T_{brake} and T_{steer} depending on initial velocity V_x .



When comparing the detection times (Figure 61), it can be seen at V1 (ego speed 52km/h, target speed 1km/h, focus range) that the radar detects the target significantly earlier. This is due to the wider FoV of the radar in the x-direction. The obstruction has no influence on the detection time at V1 (Figure 62, third column).

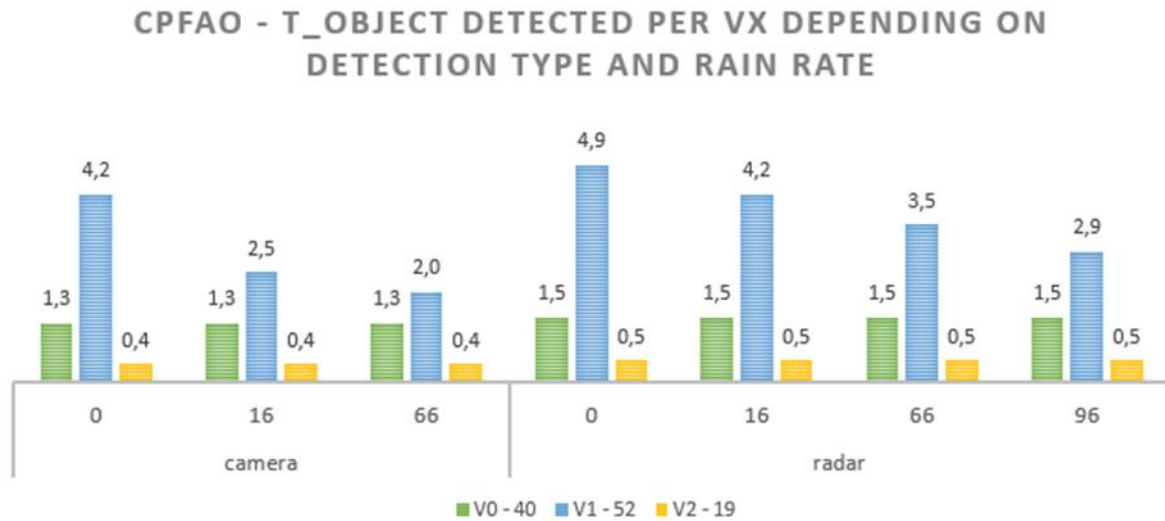


Figure 61: CPFAO – $T_{detected}$ per V_x depending on detection type and rain rate.

At V0 (ego speed 40km/h, target speed 6km/h, median) and V2 (ego speed 19km/h, target speed 16km/h, focus angle), the detection times of the radar and camera are comparable, since they are equally restricted by the visibility occlusion (Figure 62, first and second column).

In general, with respect to the influence of the rain intensity, it can be stated that it is only apparent when the visibility is not restricted by an obstruction object, i.e. at V1 (focus range). For V0 (median) and V2 (focus opening angle), no influence on the detection time can be identified up to the highest rain rate of 66mm/h and 96mm/h, respectively.



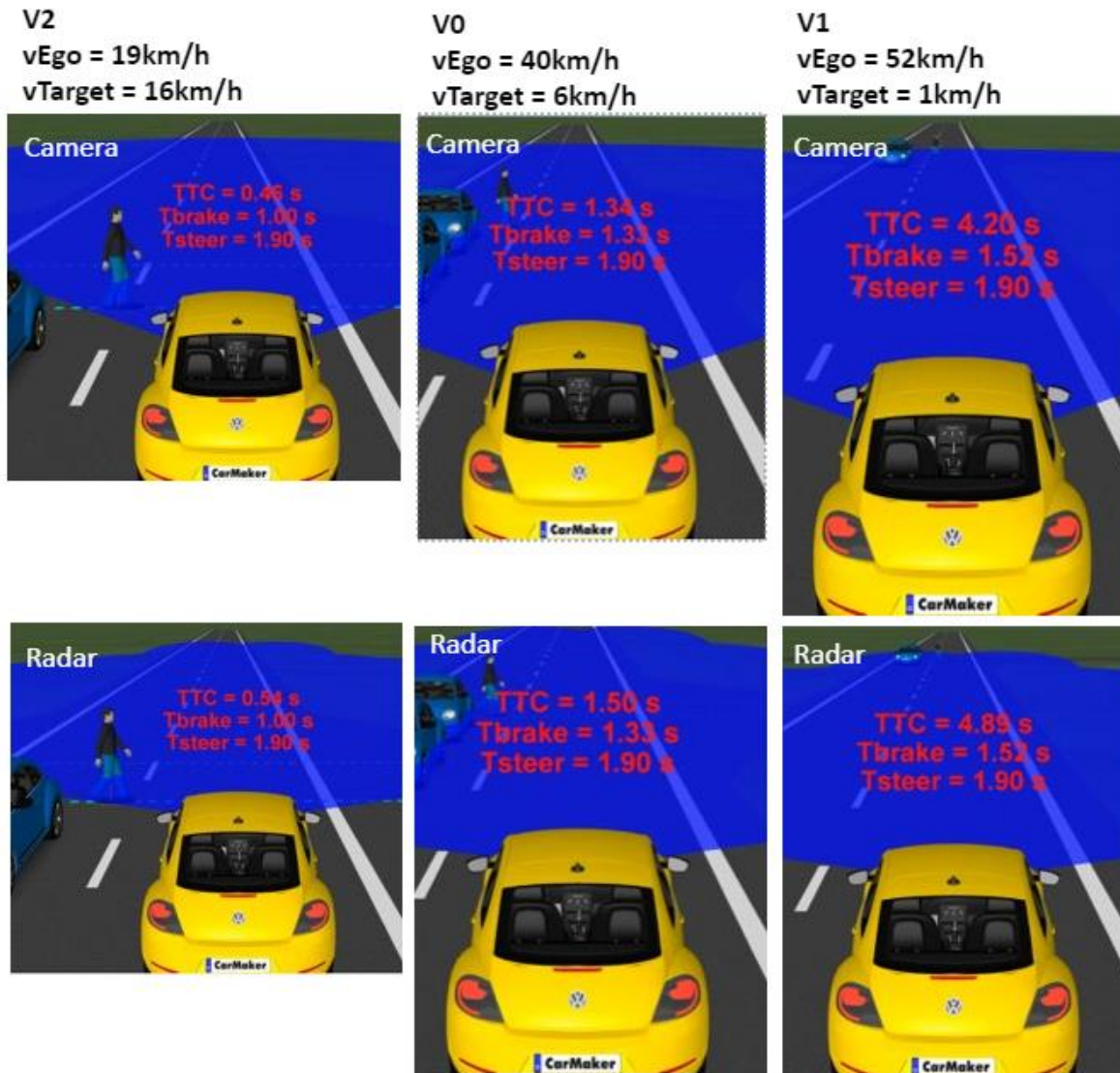


Figure 62: CPFAO – comparison $T_{detected}$ camera and radar with influencing obstruction.

In order to make a statement about which detection times restricted by the rain rates have an influence on the scenario in terms of a resulting collision, the detection time is compared with the shortest intervention time per ego speed (either braking or steering) as a function of the rain rate and the detection type (Figure 63). In the following, only the collisions that are caused by the influence of the rain rate are discussed. In the CPFAO scenario, these are all those with a rain rate of 66mm/h or higher.



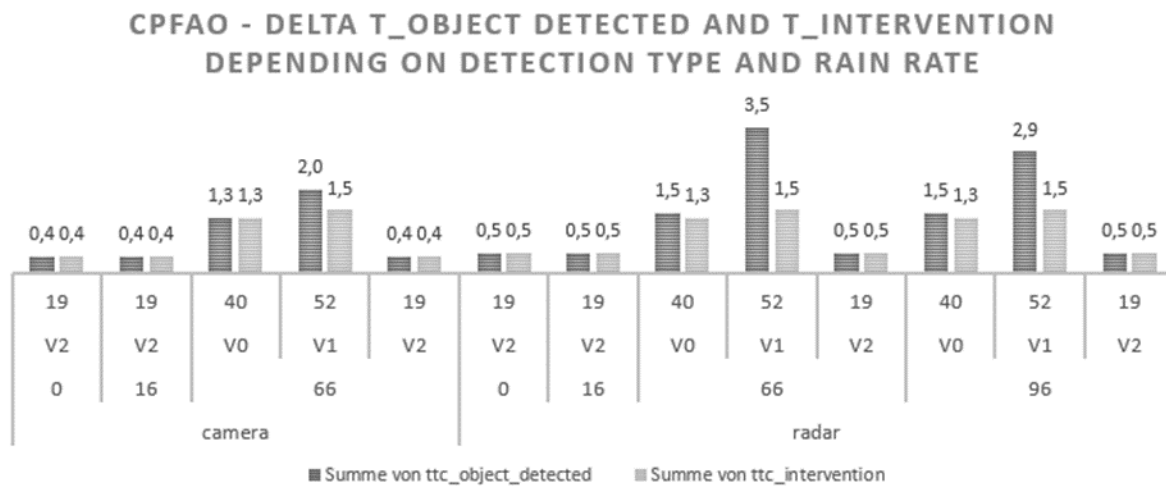


Figure 63: CPFAO – Delta $T_{detected}$ and $T_{intervention}$ depending on detection type and rain rate.

At 66 and 96mm/h rain rate, for V2 (focus opening angle) and for V0 (median) the detection and intervention time is approximately identical for both radar and camera. Accordingly, here the detection is the limiting parameter. In both cases, however, as shown in Figure 62 it is not the FoV, which is restricted by the rain rate, but the visual obstruction that is the cause. Thus, there is no potential for more robust detection in the case of rain, nor for braking to intervene earlier.

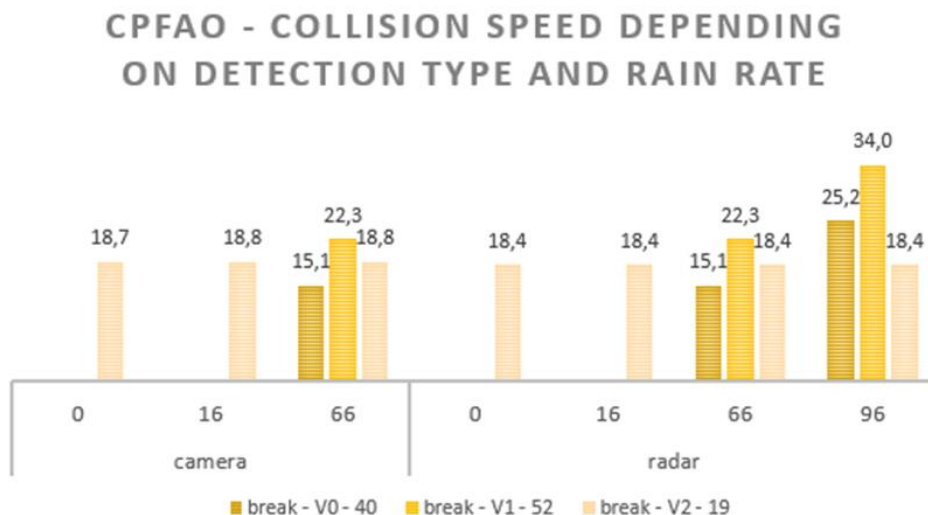


Figure 64: CPFAO – Collision speed depending on detection type and rain rate.

At V1 (52km/h ego speed and 1km/h target speed, focus range) the intervention time of the braking is 1.53s independent of the rain rate. Camera detection is possible at 66mm/h rain



rate from 2.0s and radar detection from 3.5s. The collision speed in both cases is 22.3km/h (Figure 64). With an average deceleration of 6m/s² at 66mm/h rain rate, another 10.8km/h can be reduced in the case of camera detection and 43.2km/h in the case of radar detection. In the case of camera detection, this is sufficient to reduce the collision to about half the collision speed. In the case of radar detection, it is sufficient to avoid the collision.

In the case of 96mm/h rain rate and radar detection, the additional time of 1.4s at a braking deceleration of 4m/s² could reduce further 20.2km/h, which would reduce the collision speed from 34km/h to 13.8km/h. Again, there is potential for an earlier braking intervention.

Figure 65 shows the respective T_{delta} and the remaining residual velocity per detection type, precipitation intensity and ego velocity. Based on this, the cases with collision are identified, which have an avoidance or mitigation potential with an earlier emergency braking or steering, or which are limited by a late detection due to obstructions.

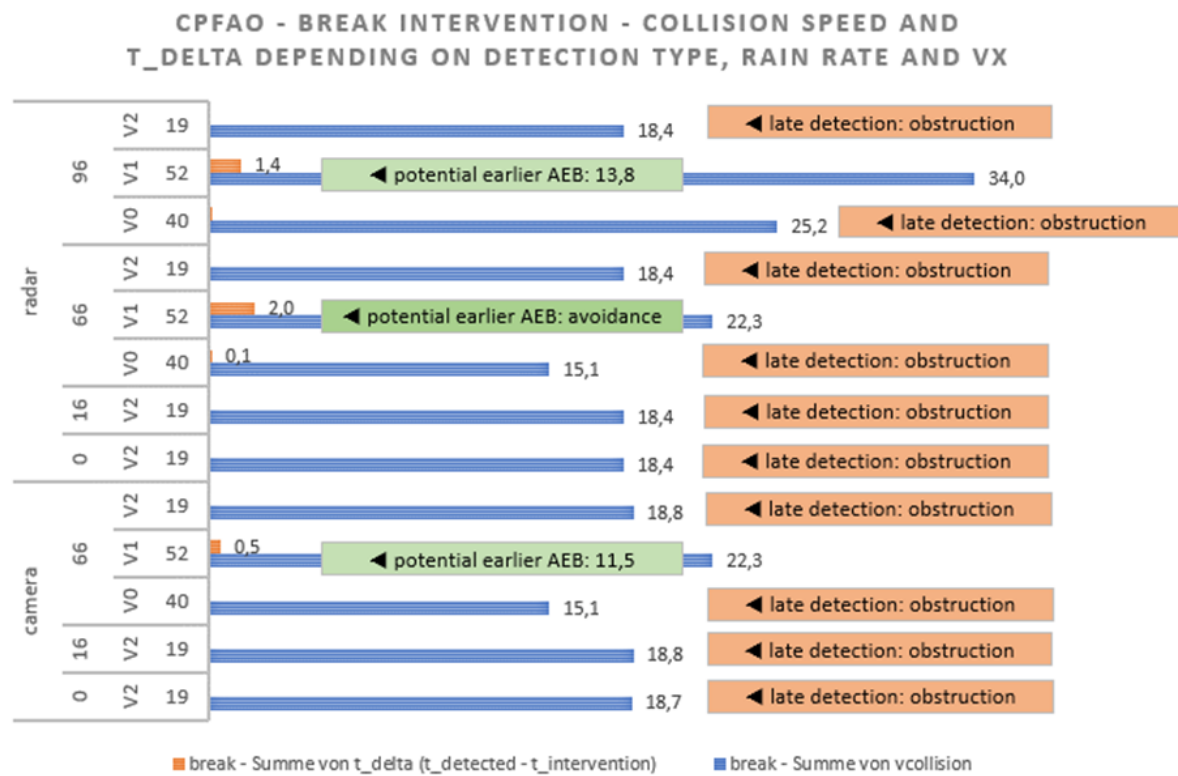


Figure 65: CPFAO – Break intervention – collision speed and T_{delta} depending on detection type, rain rate and V_x .

6.4.2.3 CPNA

In the CPNA scenario, there is also no dependence of the detection type on the number of collisions (Figure 66).



At 0 mm/h rainfall intensity, all cases are avoided. The influence of 16mm/h rain rate shows an influence in contrast to the CPFA scenario as collisions occur in 33% of the simulated cases. At 66mm/h and 96mm/h (radar only) rain rate, collisions then occur in 67% of the simulations.

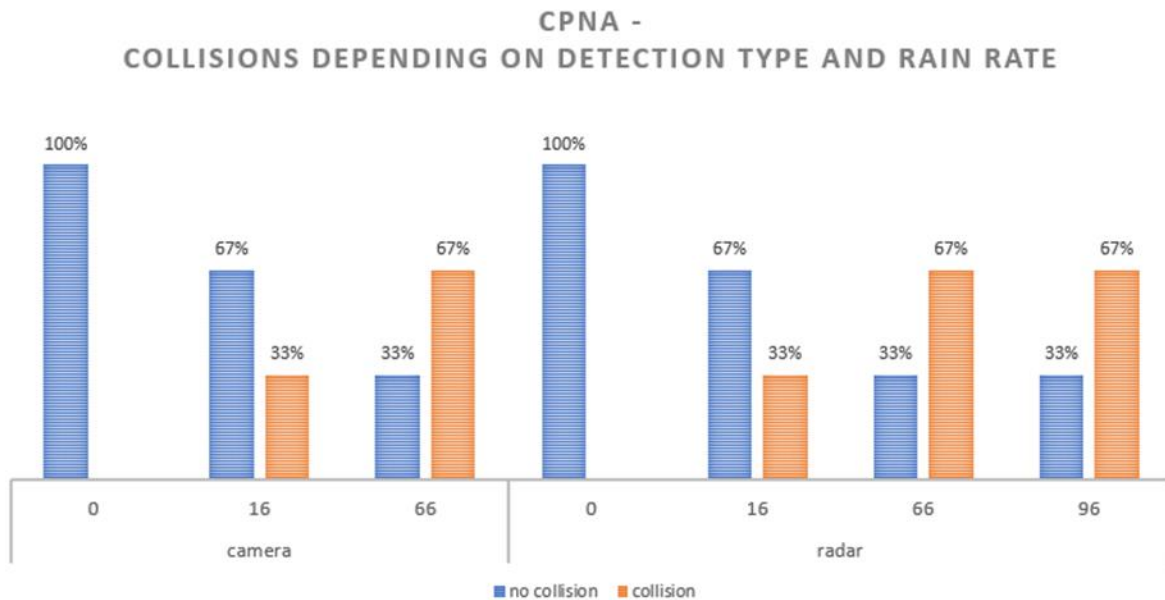


Figure 66: CPNA – Percentage of collisions depending on detection type and rain rate.

In Figure 67 it can be observed that the time T_{steer} is independent of the speed of the vehicle. It is constant at 1.9s.

The braking time varies and increases with increasing ego speed (V_x) of the vehicle. For all three speeds (V_0 – median, V_1 – focus range, V_2 – focus opening angle), T_{brake} is smaller than T_{steer} , which is why the braking maneuver is preferred.



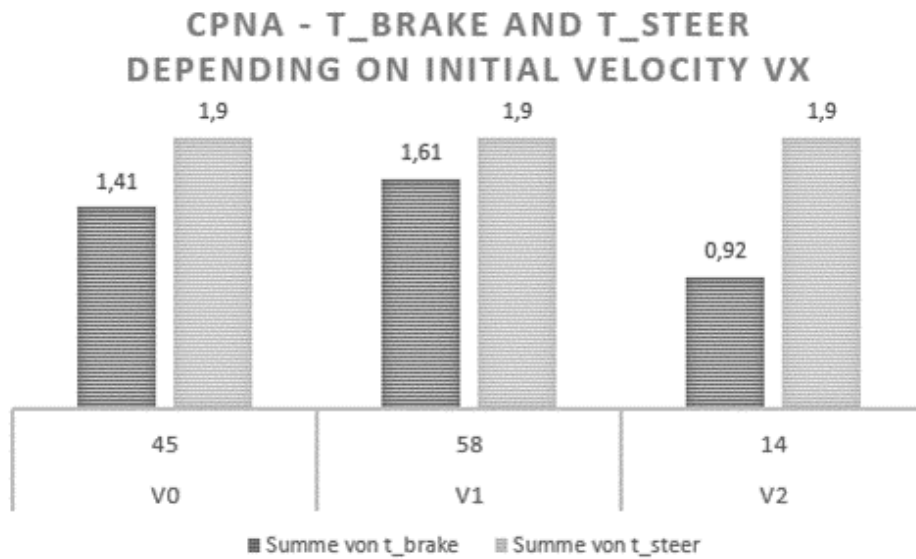


Figure 67: CPNA - T_{brake} and T_{steer} depending on initial velocity V_x.

Another influencing factor is the detection time at which the object is detected by the sensor. As shown in Figure 68, this depends on the detection type - camera or radar - as well as on the rain rate. For example, with radar detection, a rain rate of 0mm/h and an ego speed of 45km/h (V0 – median), the pedestrian is already detected at 5.4s TTC, while the camera detects it at 4.8s. In general, the radar is more likely to detect the pedestrian over all rain rates and ego speeds earlier.

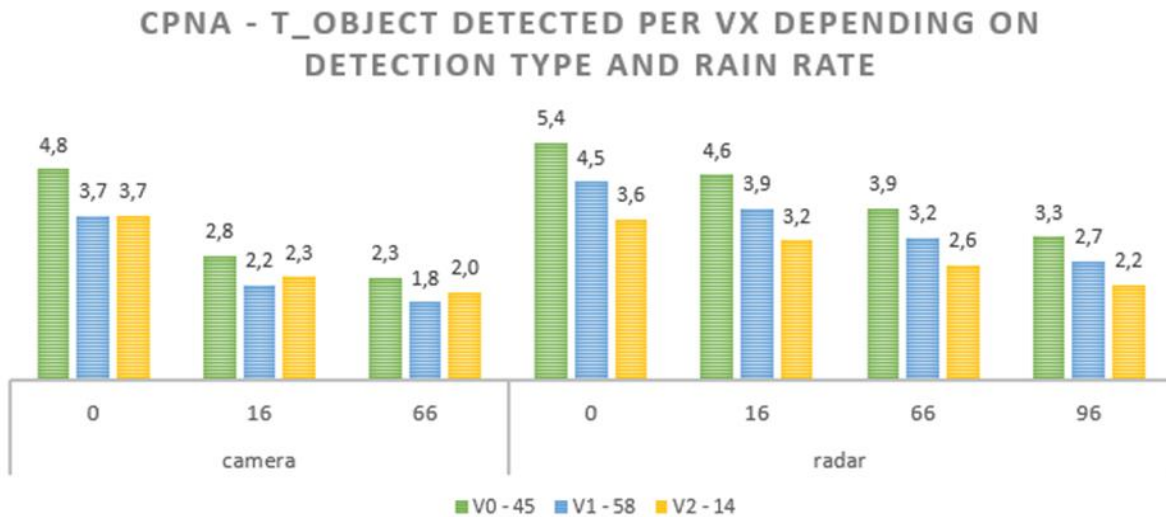


Figure 68: CPNA – $T_{detected}$ per V_x depending on detection type and rain rate.



An exception is perceivable at V2 (14km/h ego speed, 13km/h target speed, focus opening angle) and 0mm/h rain rate. Here the camera detects the pedestrian almost at the same time as the radar. This phenomenon can be explained by the fact that at high ego speeds and low target speeds (V0 - median and V1 – focus range) the target enters the detection area frontally. At low ego velocities and high target velocities, however, the target enters the lateral boundary of the FoV (see Figure 69). With frontal detection, the radar always detects the target earlier due to its longer detection range to the front. At lateral detection and 0mm/h rain rate, the FoV of the camera has almost the same width as the radar, which means that the object is detected almost simultaneously by the camera and radar. At higher rain rates, the width of the camera area decreases, especially in the area in front of the vehicle, so that the radar detects the pedestrian earlier here.

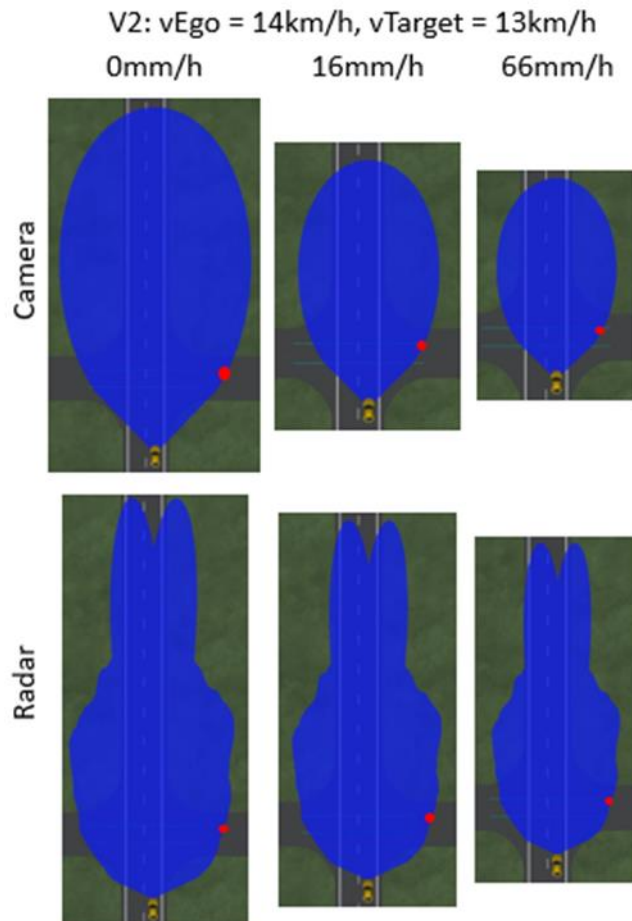


Figure 69: CPNA - FoV entering points of targets.

For frontal detection, i.e. V0 (median) and V1 (focus range), the detection time decreases with increasing ego velocity.

The influence of rain rate is evident in both camera and radar detection as the detection time decreases with increasing rain rate. A significant difference in the reduction of detection time between radar and camera is seen when the rain rates of 0 and 16mm/h are compared. Here, the camera detection time degrades by up to 40%, while the radar detection time decreases by about only 15%. When the rain rate is increased from 16 to 66mm/h, both degrade by another 15% in relation to the rain rate before.

In order to make a statement about which detection times restricted by the rain rates have an influence on the scenario in terms of a resulting collision, the detection time is compared with the shortest intervention time per ego speed (either braking or steering) as a function of the rain rate and the detection type (Figure 70). In the following, only the collisions that are caused by the influence of the rain rate are discussed. In the CPNA scenario, these are collisions at a rain rate of 66mm/h or higher.

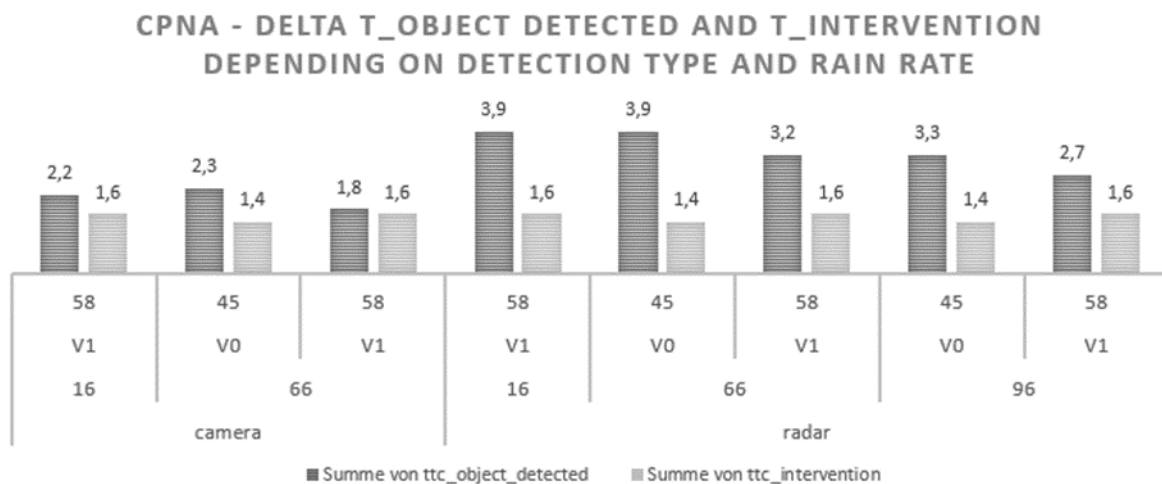


Figure 70: CPNA – Delta $T_{detected}$ and $T_{intervention}$ depending on detection type and rain rate.

The collision at 16mm/h and the ego speed of 58km/h (V1 – focus range) results from the reduced friction value compared to 0mm/h. As explained, this is not included in the calculations of the required intervention time.

If the detection time (2.2s) is higher than the intervention time (1.6s), it is possible to reduce the residual collision speed within T_{delta} by 2.2s minus 1.6s, i.e. 0.6s. In this case, the residual collision speed is 2.2km/h (Figure 71). Collision avoidance would be possible here with a delay of 8m/s². The later detection time is the cause of the collision here, but could potentially be compensated for by an earlier emergency braking. This applies to both camera and radar detection.



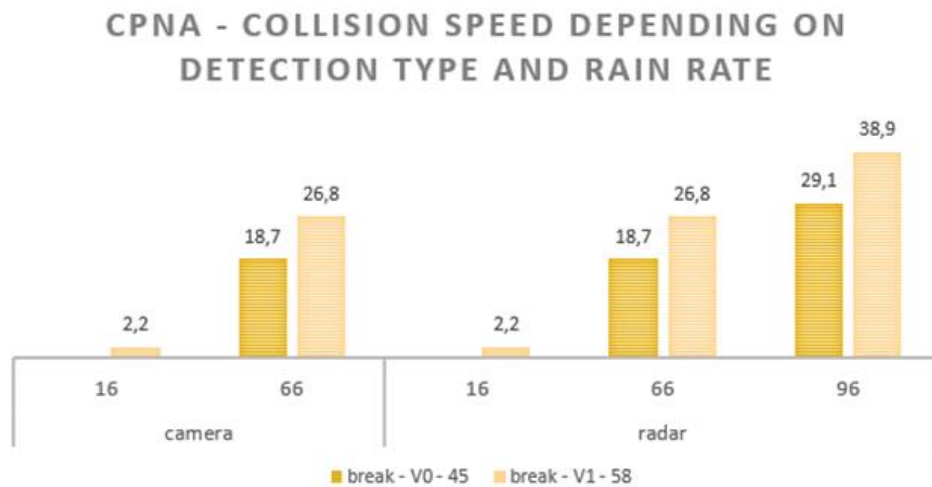


Figure 71: CPNA – Collision speed depending on detection type and rain rate.

At V1 (focus range) and 66mm/h rain rate, T_{delta} is 0.1s for camera detection and 1.6s for radar detection. The collision speed in both cases is 26.8km/h. With a deceleration of 6m/s² at 66mm/h rain rate, the collision would not have been avoidable for the camera detection. In the case of radar detection, however, it could.

At V1 (focus range) and 96mm/h rain rate, T_{delta} is 1.1s for radar detection. The collision speed here is 38.9km/h. With a deceleration of 4m/s² at 96mm/h rain rate, the collision speed could potentially be reduced by about 15.8km/h, i.e., to about 23km/h.

In the collision case V0 (median) with 45km/h ego speed, 5km/h target speed and 66mm/h rain rate, there is T_{delta} of 0.9s for camera detection and a T_{delta} of 2.5s for radar detection. The collision speed in both cases is 18.7km/h. With a delay of 6m/s² at 66mm/h rain rate, the collision would have been potentially avoidable for both camera and radar detection.

At V0 (median) and 96mm/h rain rate, T_{delta} is 1.8 s for radar detection. The collision speed here is 29.1km/h. With a delay of 4m/s² at 96mm/h rain rate, the collision speed could potentially be reduced by about 25.9km/h, i.e. to about 3km/h.

Figure 72 shows T_{delta} and the remaining velocity per detection type, precipitation intensity and ego velocity. Based on this, the cases with collision are identified, which have an avoidance or mitigation potential with an earlier emergency braking or steering, or which are limited by a late detection due to obstructions.



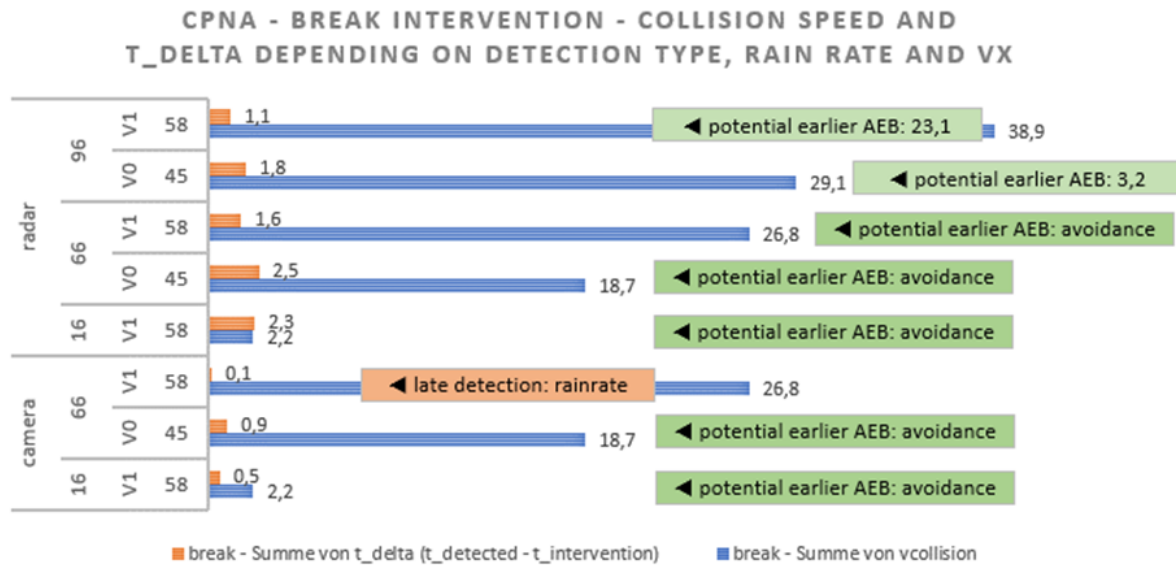


Figure 72: CPNA – Brake intervention – collision speed and T_{delta} depending on detection type, rain rate and V_x .

6.4.2.4 CPNAO

In the CPNAO scenario, no dependence of the detection type on the number of collisions is observed (Figure 73).

At 0 and 16 mm/h rain rate in 33% of the simulated cases collisions occur. The influence of 16mm/h rain rate shows no influence. Then at 66mm/h and 96mm/h (radar only) rain rate in 100% of the simulations collisions occur.



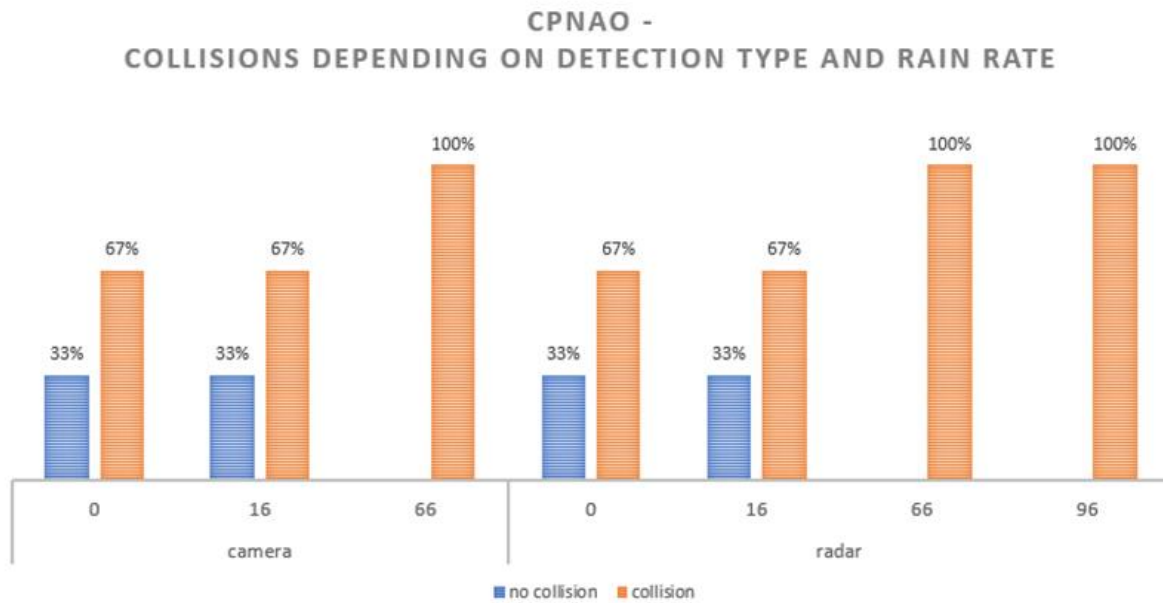


Figure 73: CPNAO – Percentage of collisions depending on detection type and rain rate.

In Figure 74 it can be seen that the time T_{steer} is independent of the speed of the vehicle. It is constant at 1.9s. The braking time varies and increases with increasing ego speed (V_x). For all three speeds (V_0 – median, V_1 – focus range, V_2 – focus opening angle), T_{brake} is smaller than T_{steer} , which is why the braking maneuver is preferred here as well.

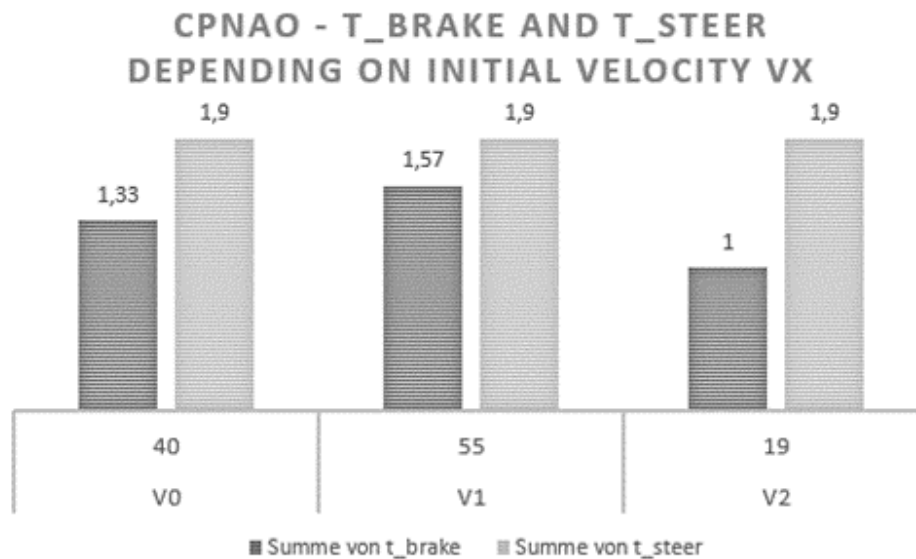


Figure 74: CPNAO – T_{brake} and T_{steer} depending on initial velocity V_x .



When comparing the detection times (Figure 75), the detection times between radar and camera are comparable for V1 (ego speed 55km/h, target speed 3km/h, focus range), V0 (ego speed 40km/h, target speed 6km/h, median) and V2 (ego speed 19km/h, target speed 15km/h, focus opening angle).

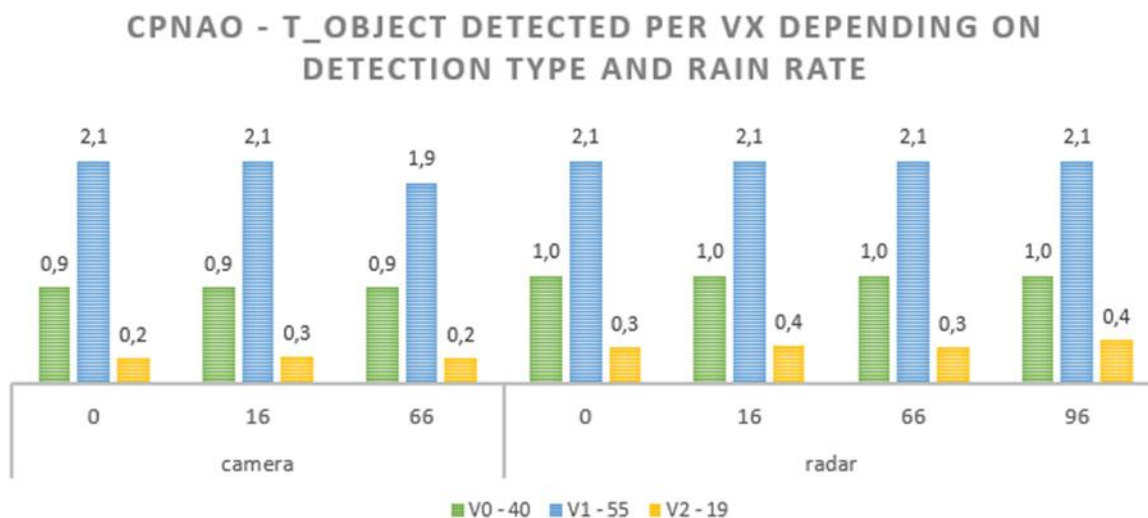


Figure 75: CPNAO – $T_{detected}$ per V_x depending on detection type and rain rate.

In general, with regard to the influence of the rain rate, it can be stated that it has almost no influence on the detection time. Only at the camera detection, V1 (focus range) and 66mm/h a delayed detection of 0.2s compared to 0mm/h is observable. The detection time is otherwise limited solely by the obstructions at all three speeds (Figure 76).

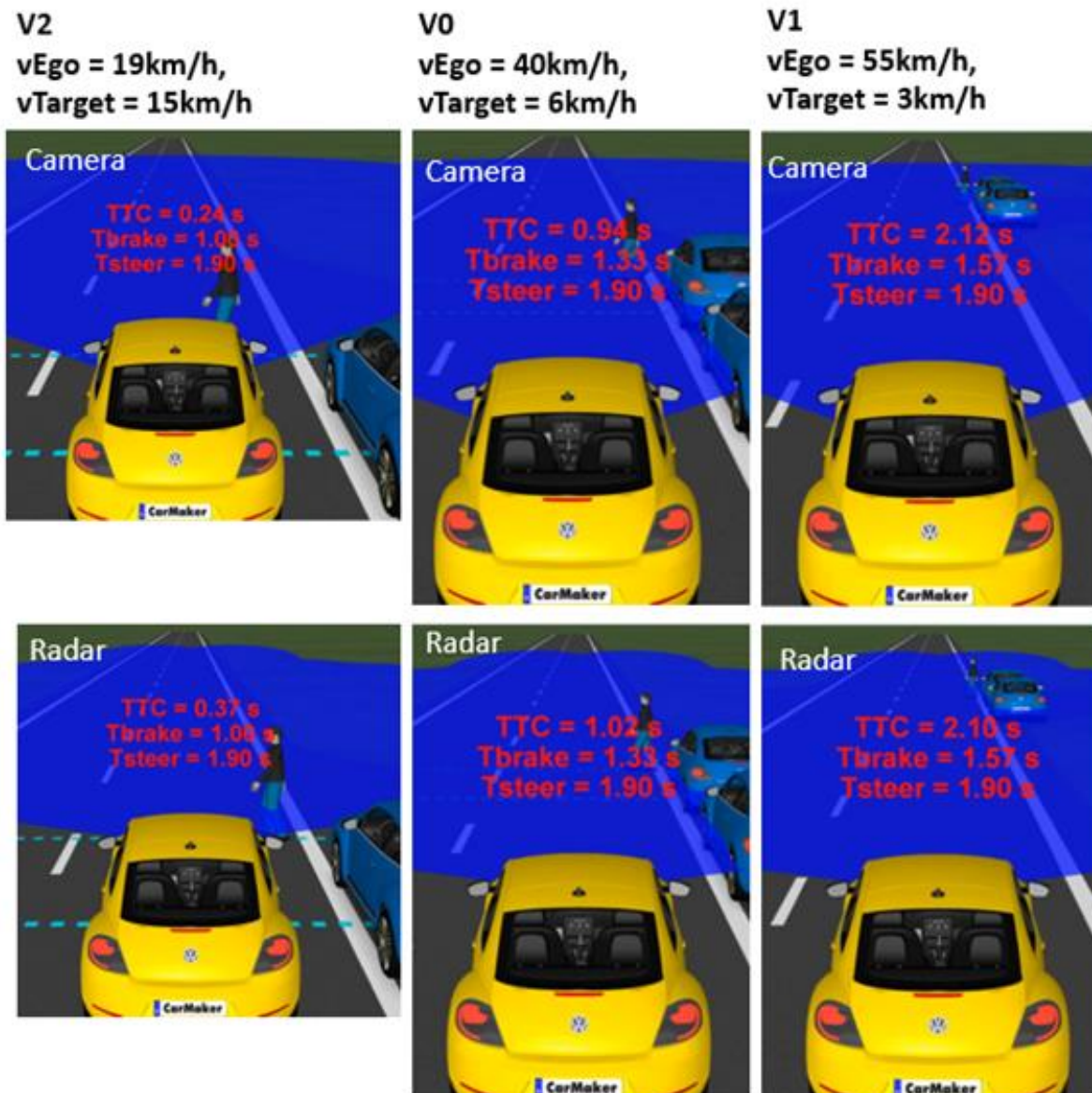


Figure 76: CPNAO – comparison $T_{detected}$ camera and radar with influencing obstruction, rain rate 0mm/h.

In order to make a statement about which detection times restricted by the rain rates have an influence on the scenario in terms of a resulting collision, the detection time is compared with the shortest intervention time per ego speed (either braking or steering) as a function of the rain rate and the detection type (Figure 77). In the following, only the collisions that are caused by the influence of the rain rate are discussed. In the case of the CPNAO scenario, these are collisions at a rain rate of 66mm/h and higher.



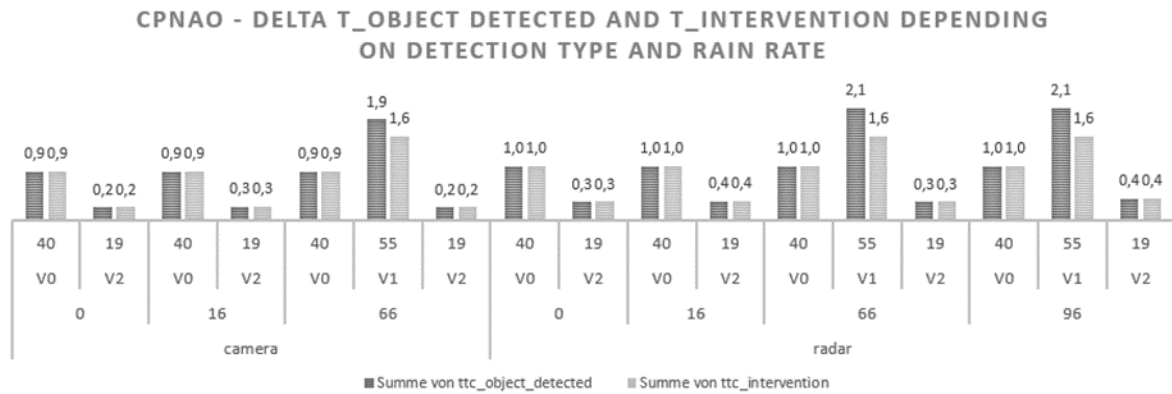


Figure 77: CPNAO – Delta $T_{detected}$ and $T_{intervention}$ depending on detection type and rain rate.

In both cases, at 66 and 96mm/h rain rate, the detection and intervention time in the case of radar and camera detection is approximately identical for V2 as well as for V0. Accordingly, here the detection is the limiting parameter. In both cases, however, as shown in Figure 77 the limiting factor is not the rain rate, but the line-of-sight coverage. Thus, there is no potential for more robust detection in the case of rain, nor for braking to intervene earlier.

At V1 (55km/h ego speed, 3km/h target speed, focus range) the intervention time of the braking is 1.57s independent of the rain rate. Camera detection is possible at 66mm/h rain rate at 1.9s and radar detection at 2.1s. The collision speed in both cases is 24.4km/h (Figure 78). With an average deceleration of 6m/s² at 66mm/h rain rate, another 6.5km/h can be reduced in the case of camera detection and 10.8km/h in the case of radar detection. In both cases, this is not enough to avoid the collision, however the collision speed can be reduced. A potential by an earlier braking intervention would be given here.

In the case of 96mm/h rain rate and radar detection, the additional time of 0.5s at a braking deceleration of 4m/s² could reduce further 7.2km/h, which would reduce the collision speed from 36.4km/h to 29.2km/h.



CPNAO - COLLISION SPEED DEPENDING ON DETECTION TYPE AND RAIN RATE



Figure 78: CPNAO – Collision speed depending on detection type and rain rate.

Figure 79 shows the respective T_{delta} and the remaining residual velocity per detection type, precipitation intensity and ego velocity. Based on this, the cases with collision are identified, which have an avoidance or mitigation potential with an earlier emergency braking or steering, or which are limited by a late detection due to obstructions.



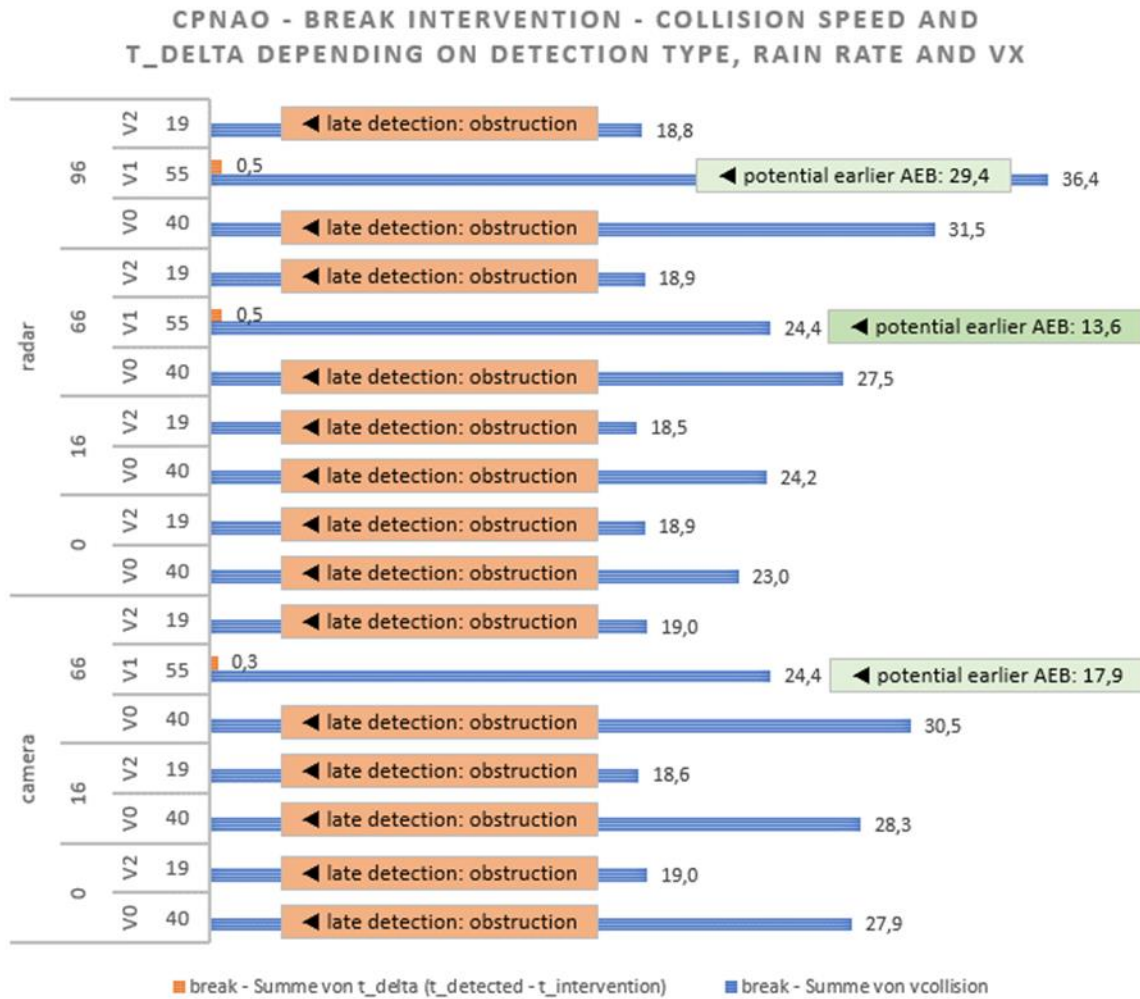


Figure 79: CPNAO – Break intervention – collision speed and T_{delta} depending on detection type, rain rate and V_x .

6.4.2.5 CPLA

In contrast to all other scenarios, a dependence of the detection type on the number of collisions can be observed in the CPLA scenario (Figure 80).

At 0 mm/h precipitation intensity, all cases are avoided for both camera and radar detection. The influence of 16mm/h precipitation intensity shows in camera detection the influence that in 33% of the performed simulations collisions occur. For radar detection, again all simulated cases are avoided. At 66mm/h rainfall intensity in 67% of the simulations collisions occur and at 96mm/h rain rate in 100% (radar only).



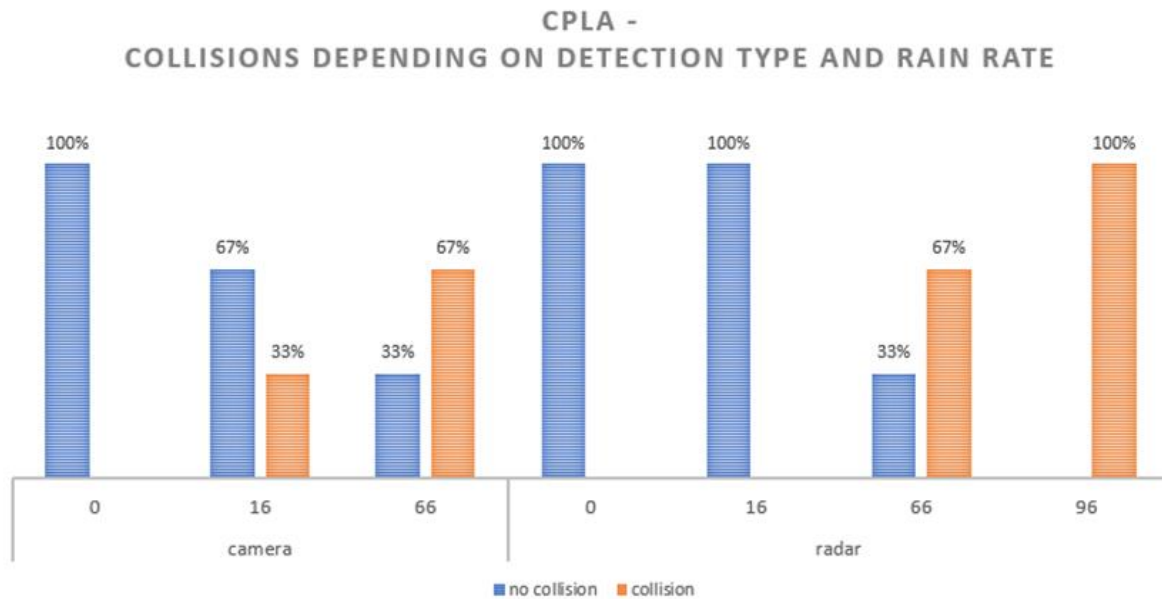


Figure 80: CPLA – Percentage of collisions depending on detection type and rain rate.

In Figure 81 it can be observed that the time T_{steer} is independent of the speed of the vehicle. It is constant at 1.9s.

The braking time varies and increases with increasing ego speed (V_x) of the vehicle. For the speed configurations V0 (median) and V2 (focus range best case), T_{brake} is smaller than T_{steer} , so the braking maneuver is preferred. For V1 (focus range worst case), T_{steer} is marginally smaller than T_{brake} , which is why the evasive maneuver is preferred for the ego speed 79km/h and target speed 6km/h (oncoming).



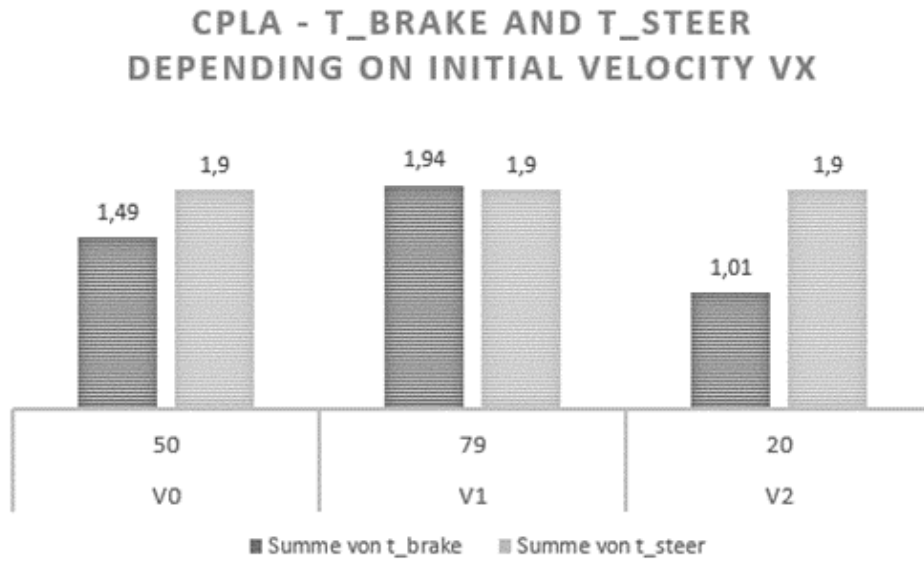


Figure 81: CPLA – T_{brake} and T_{steer} depending on initial velocity V_x .

When comparing the detection times (Figure 82), it can be seen at V0 (ego speed 50km/h, target speed 5km/h, median - same direction), at V1 (ego speed 79km/h, target speed 6km/h, focus range worst case - oncoming) and at V2 (ego speed 20km/h, target speed 2km/h, focus range best case - same direction) that the radar detects the target earlier at all rain rates.

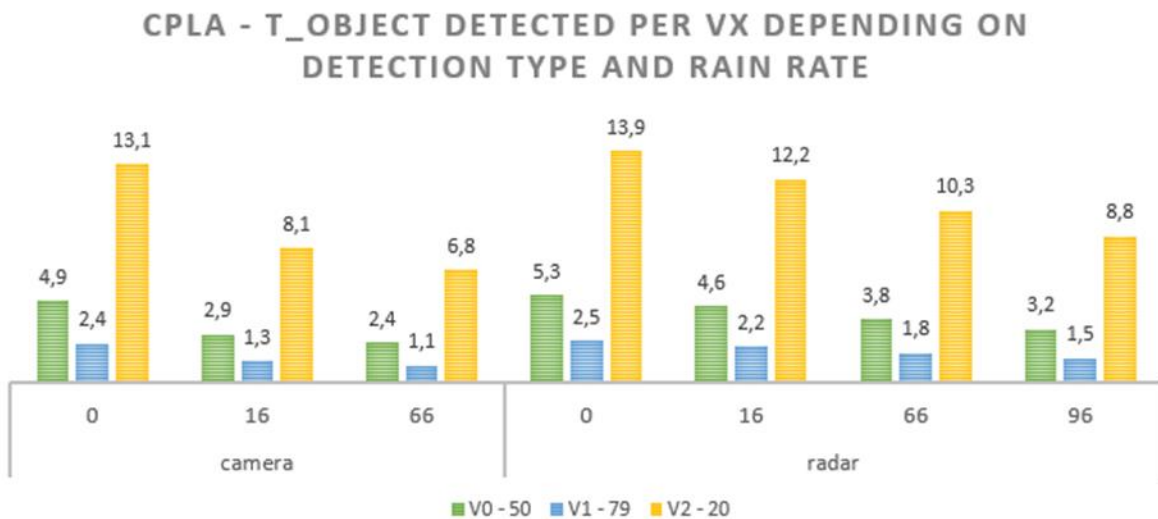


Figure 82: CPLA – $T_{detected}$ per V_x depending on detection type and rain rate.

A significant difference in the reduction of detection time between radar and camera is seen also here when the rain rates of 0 and 16mm/h are compared. The camera detection time



degrades by up to 45%, while the radar detection time degrades by only about 15%. When increasing the precipitation intensity from 16 to 66mm/h and higher, both detection types degrade by another 15-18% in relation to the precipitation intensity before.

In order to make a statement about which detection times restricted by the rain rates have an influence on the scenario in terms of a resulting collision, the detection time is compared with the shortest intervention time per ego speed (either braking or steering) as a function of the rain rate and the detection type (Figure 83). In the following, only the collisions that are caused by the influence of the rain rate are discussed.

In the CPLA scenario, these are collisions starting at rain rates of 16mm/h for camera detection and collisions starting at rain rates of 66mm/h for radar detection.

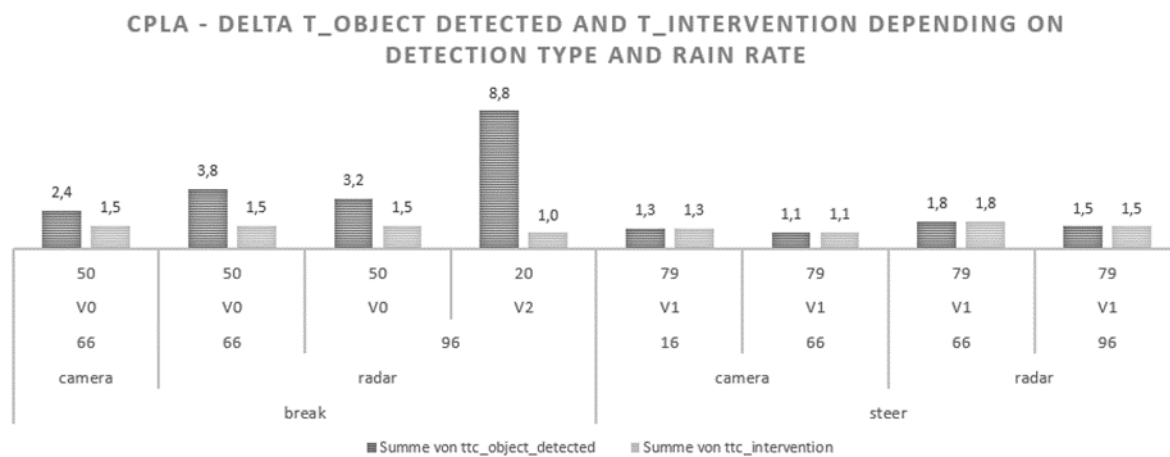


Figure 83: CPLA – Delta T_{detected} and $T_{\text{intervention}}$ depending on detection type and rain rate.

For both detection types and for all rain intensities shown of V1 (ego speed 79km/h, target speed 6km/h, focus range worst case - oncoming), there is no difference between detection and intervention times. Thus, the rain rate and the consequently limited FoV is the cause of the collision. In these V1 cases, the preferred steering intervention could not be performed in a collision-avoiding manner, resulting in a collision at 79km/h in all cases (Figure 84).

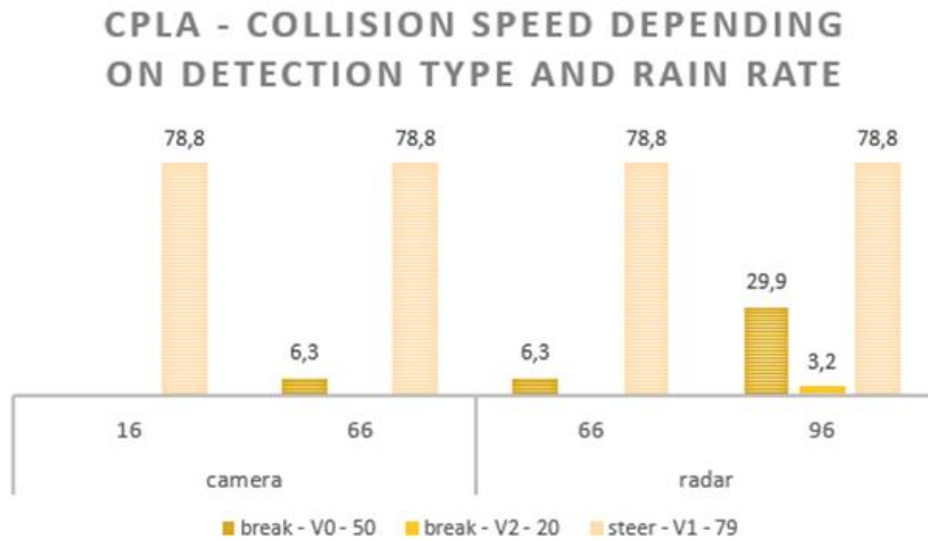


Figure 84: CPLA – Collision speed depending on detection type and rain rate.

At V0 (ego speed 50km/h, target speed 5km/h, median - same direction), the target is detected at 66mm/h with the camera at 2.4s and with the radar at 3.8s. Brake intervention starts 1.5s before collision, thus with the reduced friction it leads to a collision with 6.3km/h residual speed. Both cases could potentially be avoided using T_{delta} between detection and brake initiation with a delay of 6m/s² at 66mm/h rain rate. At 96mm/h rain rate in the case of radar detection, a T_{delta} of 1.7s and a deceleration of 4m/s², the collision speed could potentially be reduced by 24.5km/h to about 5km/h (Figure 85).

For V2 (ego speed 20km/h, target speed 2km/h, focus range best case - same direction), a collision occurs only at 96mm/h rain rate. The T_{delta} of 7.8s calculated with a deceleration of 4m/s² leads to a potential collision avoidance.

Figure 85 shows the respective T_{delta} and the remaining residual velocity per detection type, precipitation intensity and ego velocity. Based on this, the cases with collision are identified, which have an avoidance or mitigation potential with an earlier emergency braking or steering, or which are limited by a late detection due to obstructions.



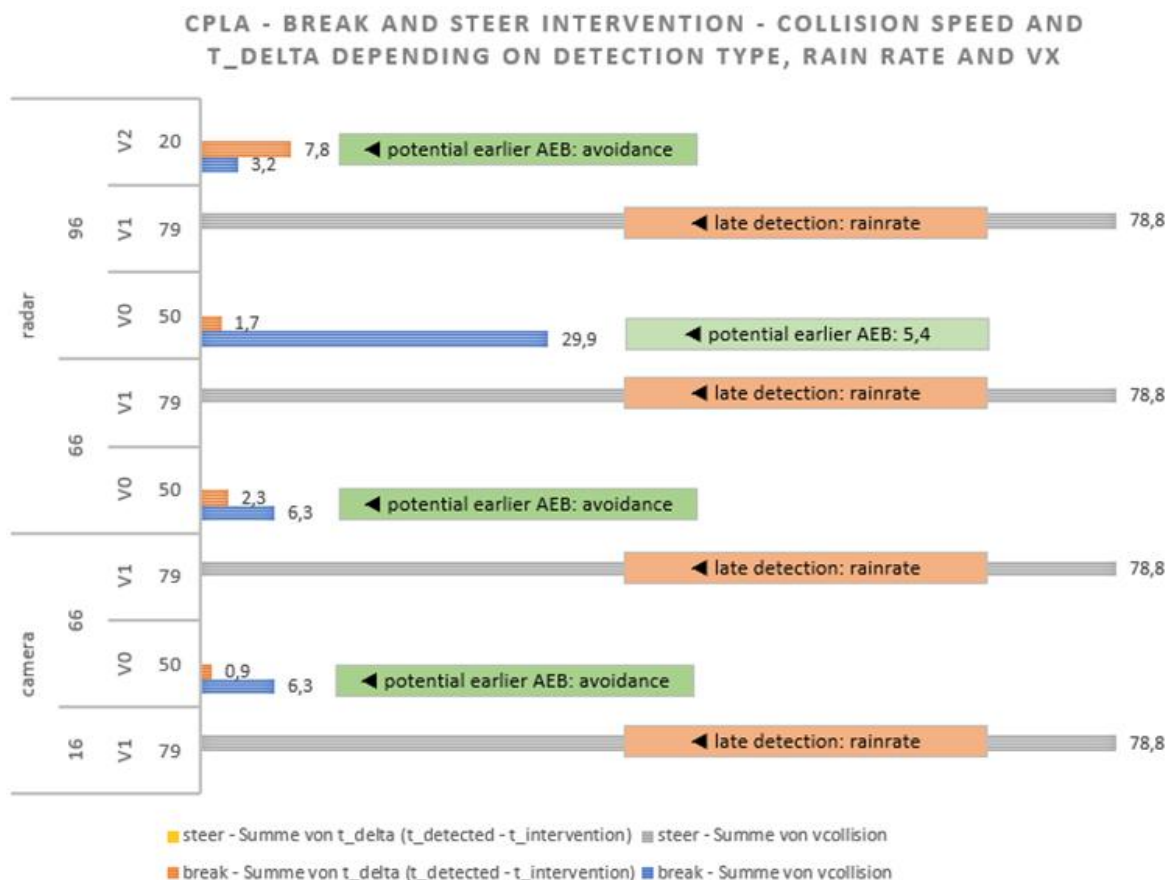


Figure 85: CPLA – Break intervention – collision speed and T_{delta} depending on detection type, rain rate and V_x .

6.4.2.6 CPTA

In the CPTA scenario, no dependence of the detection type on the number of collisions is observed (Figure 86).

From 0 to 66mm/h rain rate, all simulated cases are avoided. At 96mm/h (radar only) rain rate, in 25% of the performed simulations collisions occur.



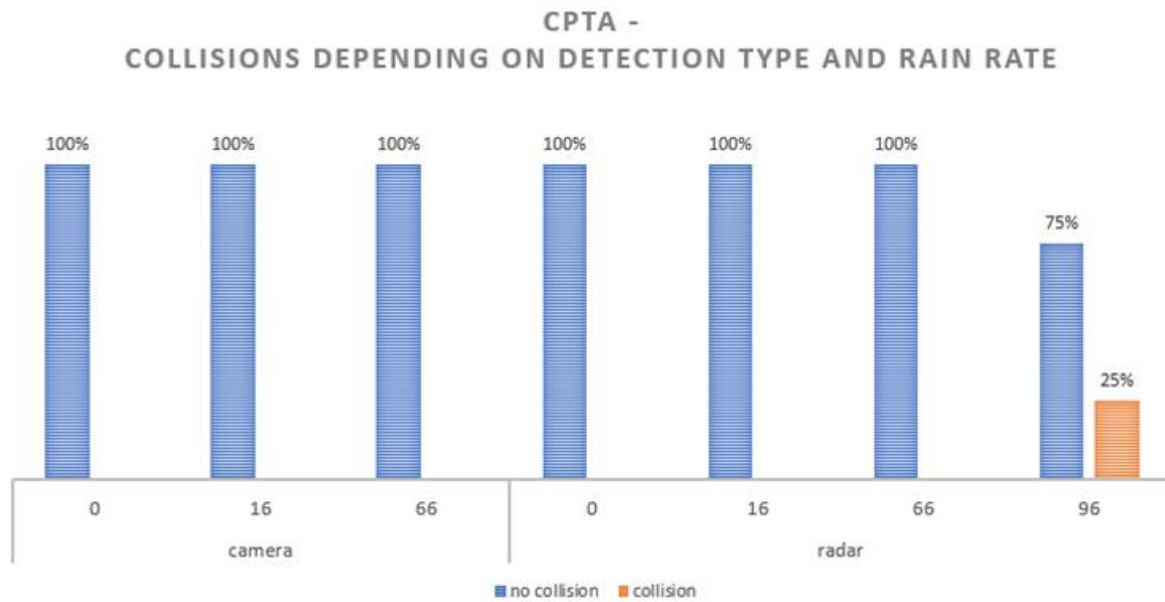


Figure 86: CPTA – Percentage of collisions depending on detection type and rain rate.

Figure 87 shows that the time T_{steer} is independent of the speed of the vehicle. It is constant at 1.9s.

The braking time varies marginally and increases with increasing ego speed (V_x) of the vehicle. Thus, for all ego speeds from 17km/h to 24km/h, the braking time is approximately 1s. For all three speeds (V_0, V_1, V_2, V_3 – median), T_{brake} is smaller than T_{steer} , which is why the braking maneuver is preferred.



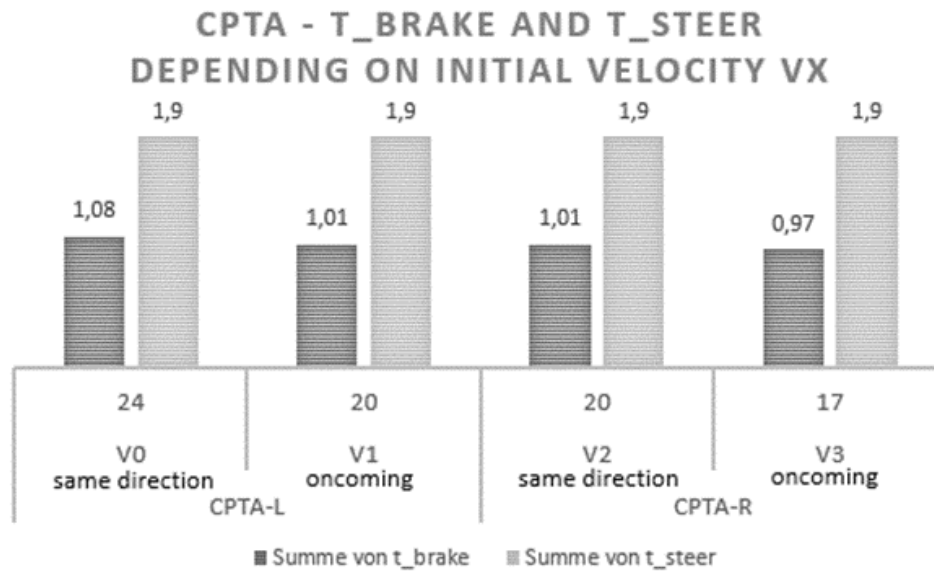


Figure 87: CPTA – T_{brake} and T_{steer} depending on initial velocity V_x and target direction.

Another influencing factor is the detection time at which the object is detected by the sensor. As shown in Figure 88, this depends on the type of detection - camera or radar - as well as on the rain rate. In the case of the turning scenarios, there is also a split into the turning direction, since when turning right (nearside) the pedestrian enters the FoV sooner than when turning left (farside) due to the smaller lateral distance to the ego vehicle. Thus, detection times are generally higher when turning right with oncoming and same-direction targets.

For both left and right turns - whether camera or radar detection - detection times decrease with increasing rain rate.

In the comparison between camera and radar detection it is noticeable that the camera detection is earlier than the radar detection only when turning to the left and 0mm/h rain rate.

A further difference can be seen when turning left at the rain rate of 66mm/h for the camera: In contrast to all other simulated cases of turning left, the detection time of V0 (ego speed 24km/h, target speed 5km/h, median - same direction) is shorter than V1 (ego speed 20km/h, target speed 5km/h, median - oncoming).



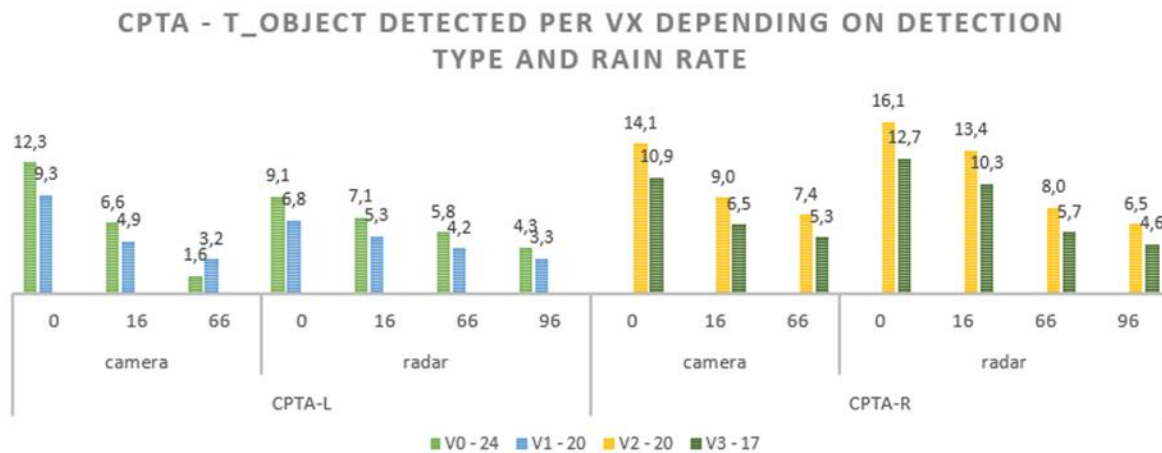


Figure 88: CPTA – $T_{detected}$ per V_x depending on detection type and rain rate.

In order to make a statement about which detection times restricted by the rain rates have an influence on the scenario in terms of a resulting collision, the detection time is compared with the shortest intervention time per ego speed (either braking or steering) as a function of the rain rate and the detection type (Figure 89). In the following, only the collisions that are caused by the influence of the rain rate are discussed. This is the case for the CPTA scenario only at 96mm/h rain rate (Figure 89).

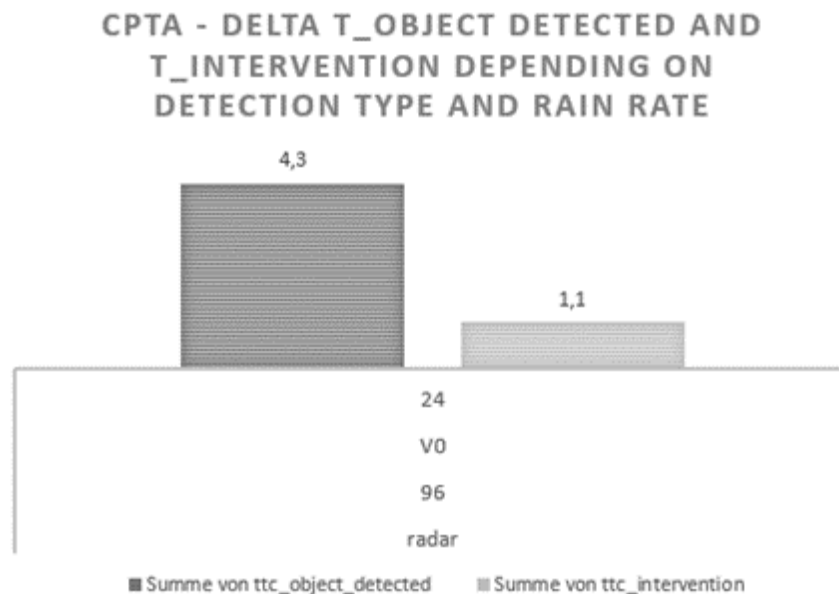


Figure 89: CPTA – Delta $T_{detected}$ and $T_{intervention}$ depending on detection type and rain rate.



At V0 (ego speed 24km/h, target speed 5km/h, median - same direction), the target is detected at 96mm/h by the radar at 4.3s. The braking intervention starts 1.1s before the collision, thus leading to a collision with 5.2km/h residual speed due to the reduced friction (Figure 90).

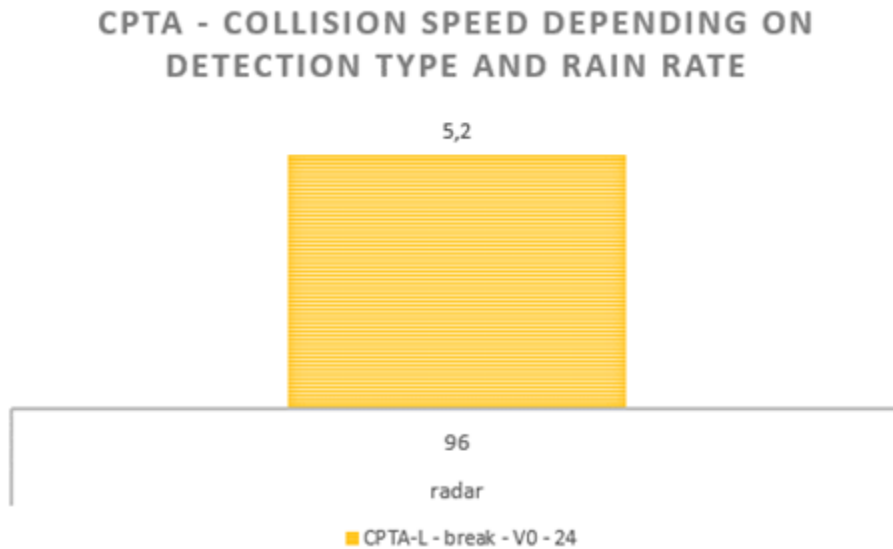


Figure 90: CPTA – Collision speed depending on detection type and rain rate.

Using T_{delta} between detection and brake initiation with a deceleration of $4m/s^2$ at 96mm/h rain rate, the collision could potentially be avoided (Figure 91).

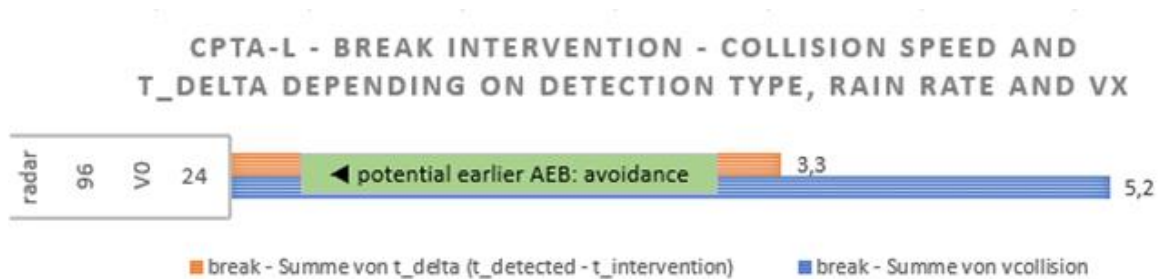


Figure 91: CPTA – Break intervention – collision speed and T_{delta} depending on detection type, rain rate and V_x .



6.4.3 Result summary

The summary of the results of the individual scenarios focuses on the rain rates 0 to 66mm/h. This is based on two factors: Firstly, rain rates lower than 16mm/h usually occur, but this was the lowest measurable value in the test hall (see (SAFE-UP, Deliverable report D2.6, 2021) for evaluation). On the other hand, the rain rate 66mm/h takes into account a coefficient of friction of 0.6, which can also occur at lower rain rates due to road irregularities caused by water accumulation. A rain rate of 96mm/h, in contrast, is to be categorized as a locally occurring and very rare phenomenon.

Figure 92 shows an overview of the simulated scenarios at the rainfall rates 0mm/h, 16mm/h and 66mm/h. For each scenario, the share of simulations with collisions, the influence of the detection type and the cause of the collision are evaluated.

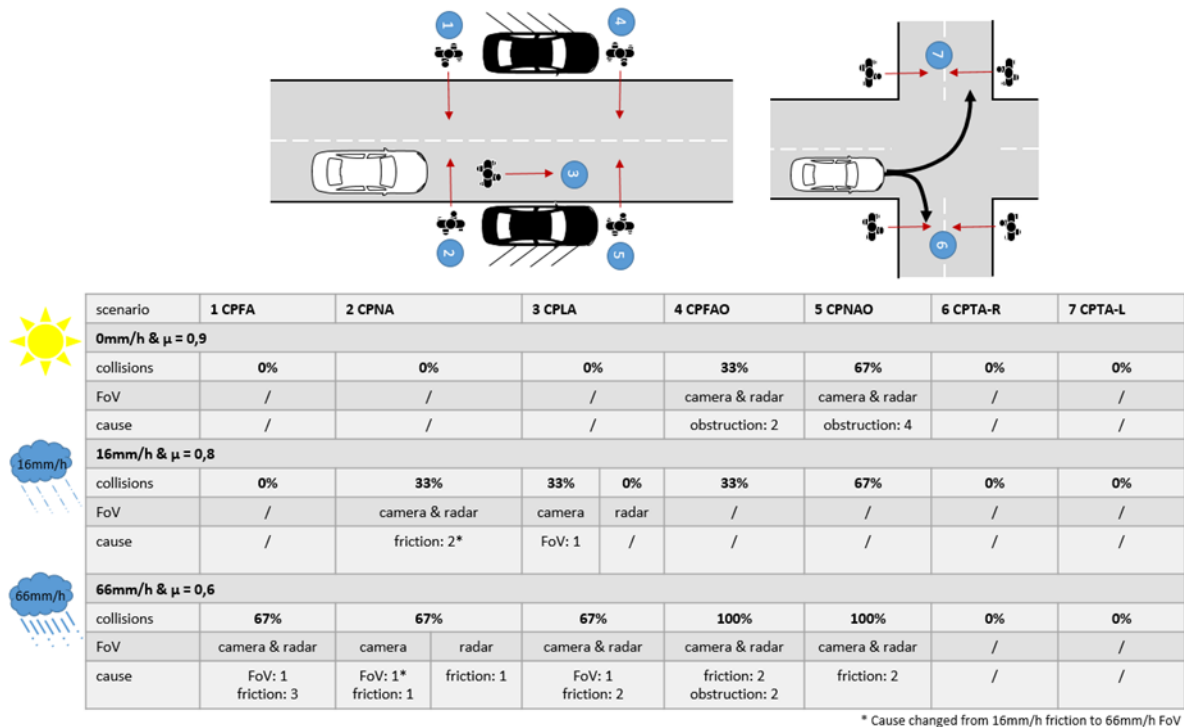


Figure 92: Scenario overview including rain rate, share of collisions, detection influence and causation (only additional causes in comparison to lower rain rates are given – except for *).

In the crossing scenario without obstruction CPNA, at 16mm/h rain rate in 33% of the simulated scenarios collisions occur compared to 0% at 0mm/h. These are due to the reduced friction. At 66mm/h rain rate, the percentage then is 67% for both crossing scenarios, CPNA and CPFA. The cause here is predominantly the reduced friction value, but also the limitation of FoV due to the rain rate.



In the longitudinal scenario (CPLA), collision occurs exclusively at the camera at 16mm/h due to the reduced FoV caused by the rain rate. At 66mm/h then 67%, but here also due to the reduced friction.

The crossing scenarios with visual obstruction, CPFAO and CPNAO, show collisions even without the influence of rain. In 33% of the simulated scenarios from CPFAO and in 67% of the simulated scenarios from CPNAO collisions occur. The reason for this is the limitation of the FoV by the visual obstruction. At 66mm/h, 100% collisions then occur in both obstructed scenarios. In contrast to the lower rain rate with the cause of visual obstruction, the reason here is also the reduced coefficient of friction and in the case of CPFAO additional two cases due to visual obstruction.

In the turning scenarios to the left and right with oncoming pedestrians as well as pedestrians moving in the same direction, no influence is visible from 0 to 66mm/h rain rate as no collisions occur.

Rain rate 0mm/h

The simulations at 0mm/h rain rate, i.e. without rain, serve as baseline and provide a possibility to compare which scenarios already show collisions without the influence of rain. This is the case for the two scenarios with visual coverage, CPFAO (33%) and CPNAO (67%).

Rain rate 16mm/h

In summary, at 16mm/h it can be concluded that the **influence of the rain rate on the FoV** is very small in the scenarios considered. Only in the scenario CPLA the limitation of the camera FoV leads to a collision. This can be explained by the higher degradation of the camera FoV from 0mm/h to 16mm/h rain rate (ca. -40%) compared to the radar FoV (ca. -15%). However, this influence is only noticeable at the high ego speed (79km/h).

The **influence of the rain rate on the friction coefficient** at 16mm/h and thus on the deceleration capabilities of the ego vehicle is evident in two cases, namely in the CPNA scenario with the high ego speed (52km/h).

The **influence of visual obstruction on the FoV** is not present in any additional scenario compared to 0mm/h.

Rain rate 66mm/h

It can be summarized that at 66mm/h the **influence of the increased rain rate on the FoV** is higher than at 16mm/h in the considered scenarios. A limited FoV due to the rain rate can be seen in further two cases in the CPFA, CPNA and CPLA scenarios. In the CPNA scenario, the cause changes from friction coefficient at 16mm/h to FoV restriction (66mm/h). All three cases involve the highest ego velocities, respectively: CPFA (63km/h), CPNA (68km/h) and CPLA (53km/h).

The **influence of rain rate on friction coefficient** at 66mm/h is evident in all crossing and longitudinal scenarios. In additional 10 out of a total of 30 simulated cases collisions occur



compared to 16mm/h. Ego speeds are in both high and medium ranges: CPFA (48km/h and 63km/h), CPNA (45km/h), CPLA (50km/h), CPFAO (52km/h), CPNAO (55km/h).

An additional **influence of visual obstruction on the FoV** at 66mm/h is present in the CPFAO scenario. Here, the lowest ego speed (19km/h) in combination with the highest target speed (16km/h) is affected.

Chosen intervention AEB or AES

Only in the **longitudinal scenarios** with a high ego velocity (79km/h) a decision was made to select an AES intervention over an AEB intervention. In this case, the difference was marginal. In all cases across nearly all rain rates (camera from 16mm/h, radar from 66mm/h), the FoV was limited by the rain rate such that a collision occurred.

6.5 Open points

The following points were not considered in these simulations, but could be explored in subsequent work:

- Impact of fusion logic between camera and radar detection with resulting limitations of FoV in terms of detection and functional performance
- Validation of theoretical results by real driving tests and quantification of a realistic avoidance and reduction potential
- Potential risk with weather-dependent design of emergency intervention in terms of type of intervention (braking, steering) and earlier intervention timing
- Generalization questionable: Confirmation of results and trends by further camera and radar sensors necessary
- More performant AEB than the one theoretically calculated here holds less potential to adapt the braking timing to it in case of reduced friction coefficient.

6.6 Trajectory analysis for passenger car conflicts with pedestrians with adverse weather conditions

This section describes the Pedestrian crossing from left without Sight Obstruction (P-CLwoSO) conflict scenario. This scenario serves as an example for the evaluation of the trajectories and the investigation of the limitation of the detection range of the sensor set in the event of precipitation. For this purpose, all accidents in the GIDAS PCM are examined using trajectory analysis and visualization (TRAVIS) with a sensor set consisting of RADAR and camera. The relevant critical time range is then determined using data from the Traffic Accident Scenario Community (TASC) of the Fraunhofer Institute for Traffic and Infrastructure Systems. The robustness of the sensor set against precipitation can be shown by bringing



together the critical time range and the proportions of pedestrians detected in the relevant time range.

Conflict Scenario Pedestrian crossing from left without Sight Obstruction (P-CLwoSO)

The Pedestrian crossing from left without sight obstruction (P-CLwoSO) scenario is used to analyze the trajectories. In this conflict, 15.3% of the n=3,420 injured pedestrians and 19.5% of the seriously or fatally injured (or killed-severely-injured, in short: KSI) pedestrians had an accident. Thus, this conflict scenario is a proxy for almost every fifth seriously injured pedestrian. Figure 93 provides an overview of this conflict. The shares of the main causer shares are equally distributed between cars (48%) and pedestrians (52%). The comparatively high proportion of conflicts at night (35.2%) and the proportion of precipitation for injured pedestrians (21.5%) as well as for seriously injured or killed pedestrians (23.1%) are striking. For this reason, this conflict is used as an example in this chapter.

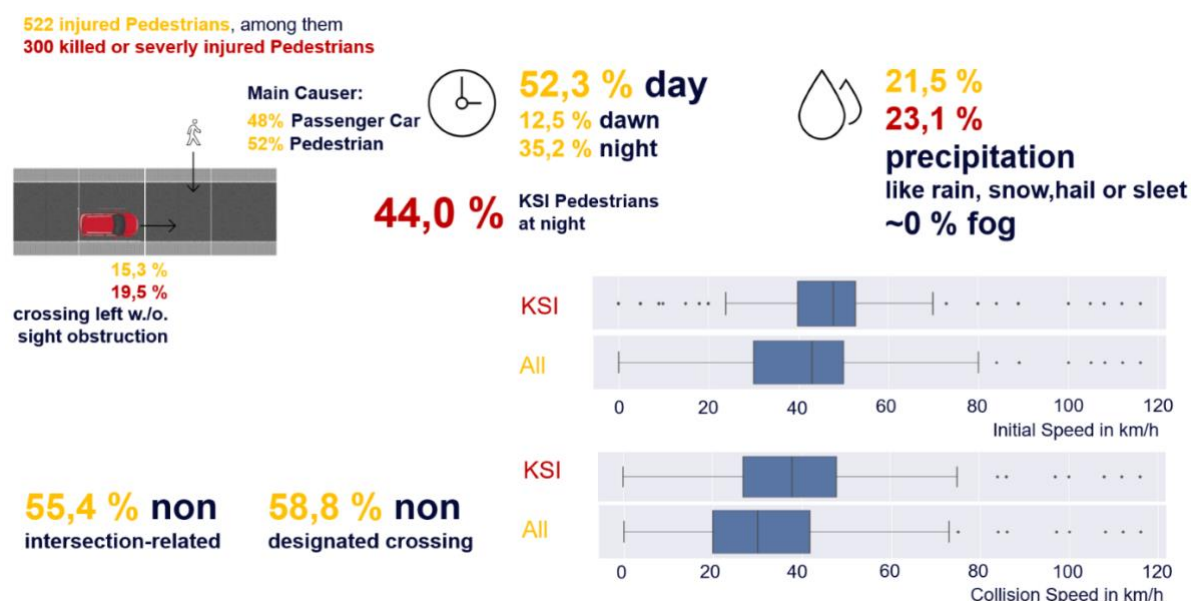


Figure 93: Conflict Scenario P-CLwoSO (SAFE-UP, Deliverable report D2.6, 2021).

Example Case for P-CLwoSO in GIDAS with the injury severity KSI

An example from the GIDAS survey is shown in Figure 94 with images of the accident site. This case corresponds to the conflict P-CLwoSO. A 70+ year old male pedestrian wanted to cross the roadway during a rainy night. From the point of view of the car, the pedestrian crossed the street from the left. According to the reconstruction, the car approached the scene of the accident at approx. 48 km/h, which corresponds to the median of the initial car speeds for KSI injured pedestrians. The driver of the car showed neither a braking nor a steering reaction before the collision. The pedestrian was hit by the vehicle in the middle-right and



subsequently fell onto the vehicle itself. The survey stated that the head had hit the vehicle in the cowl area of the window and the windscreen itself.



Figure 94: Example Case for P-CLwoSO in GIDAS.

Example Case for P-CLwoSO in TRAVIS

The accident is shown in its pre-accident phase in Figure 95 in the "Trajectory Analysis and Visualization" tool (short: TRAVIS). The information from the pre-crash matrix (PCM) of the GIDAS database is displayed here. GIDAS PCM contains surrounding objects such as houses or trees, roadsides and lane markings - as well as the trajectories with the position and speeds of those involved in the accident depending on the time from $TTC=5s$ to the time of the collision $TTC=0s$. These trajectories are highlighted in color. The lines along the trajectories each mark the position of those involved with a one-second interval. The red rectangle is the bounding box of the passenger car, the blue ellipse is the floor area of the pedestrian. The position of the participants is given at the time of the collision at $TTC=0$ s. The coordinates are given in the world coordinate system. The zero point corresponds to the zero point in the coordinate system selected for the sketch of the accident.

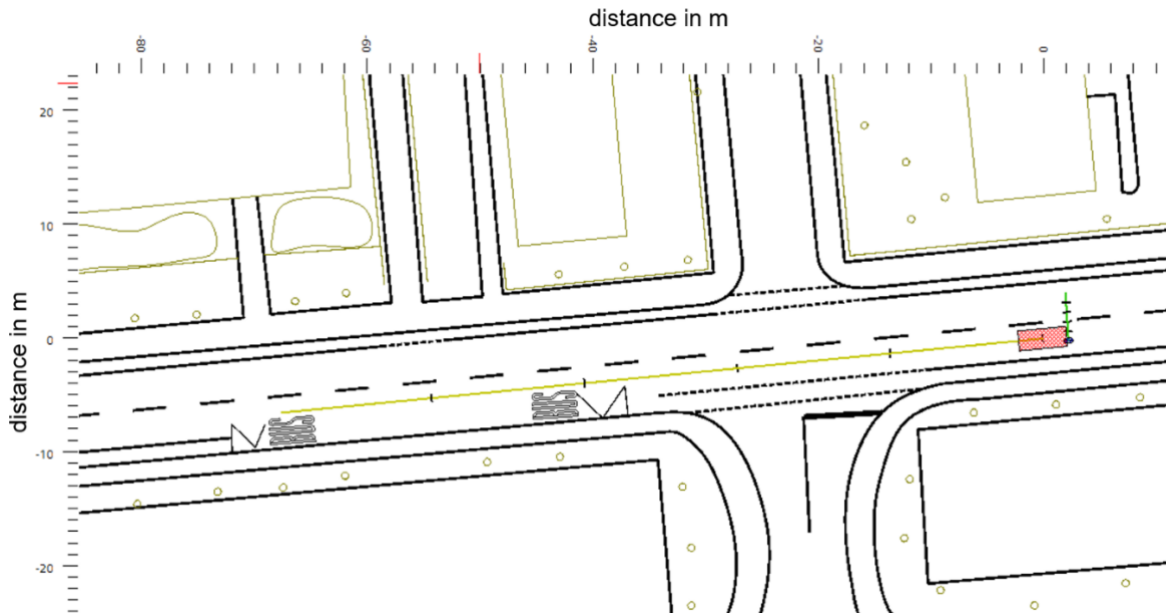


Figure 95: Example Case of P-CLwoSO out of GIDAS in TRAVIS.

All P-CLwoSO Cases in TRAVIS

All accidents that are caused by the conflict P-CLwoSO can be analyzed with TRAVIS as shown in Figure 96 with approach trajectories of pedestrians relative to the passenger car. The environment information of the accident (objects, road markings) is hidden. The cars involved in this conflict scenario are combined into a standard vehicle (length 5.00 m and width 2.20 m), the so-called ego vehicle. The center of this ego vehicle bounding box forms the new coordinate origin. The approach trajectories of the pedestrians are given for this scenario for each of the accidents ($n=298$) from the GIDAS PCM. The trajectories are colored according to the relative approach speed (green = 0 km/h to red = 120 km/h). The maximum time range of the approach is $TTC=5$ s. The longer the relative approach trajectory, the more distance is covered within the 5 seconds and the faster the relative approach of the pedestrian. The reason for this is the higher speed of the passenger car, since the walking speed of the pedestrian must be assumed to be limited. Approach trajectories that have a curved course indicate that the car was cornering before the collision. The example from GIDAS can be found with an initial distance of ~ 70 m from the pedestrian with a lateral offset of ~ 3 m at an accumulation point for this scenario P-CLwoSO.



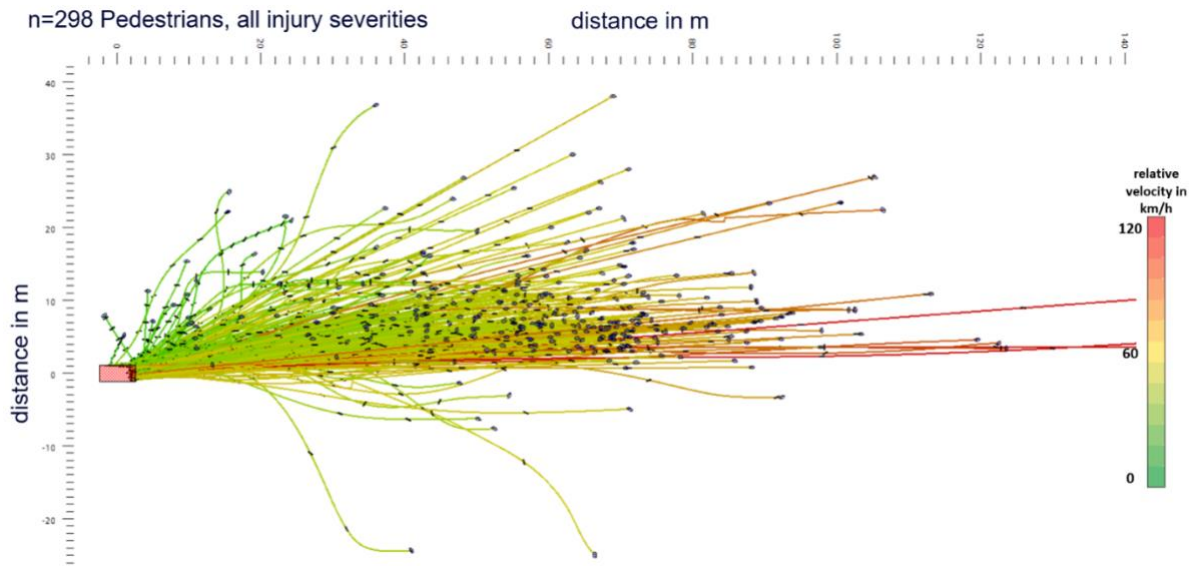


Figure 96: All cases of P-CLwoSO out of GIDAS in TRAVIS.

Analysis of Field-of-VIEWS (FoV) of all P-CLwoSO Cases using TRAVIS

Different types of sensors can be added within TRAVIS. The range of a sensor is described as a function of the opening angle. Figure 97 shows the sensor range of the radar and the camera for the trajectories according to with a precipitation rate of 16 mm/h (SAFE-UP, Deliverable report D3.5, 2022). On this basis, it can be evaluated at which TTC pedestrians involved come into the detection range of the radar or the camera. TRAVIS can be used to evaluate how high the proportion of pedestrians involved is in relation to the TTC in the detection range of the radar, the camera or the sensor set overall. A pedestrian is recognized by the sensor if half of the floor area is in the detection area. For a pedestrian to be detected in the sensor set, the pedestrian must be detected either by the camera or by the radar (or condition).



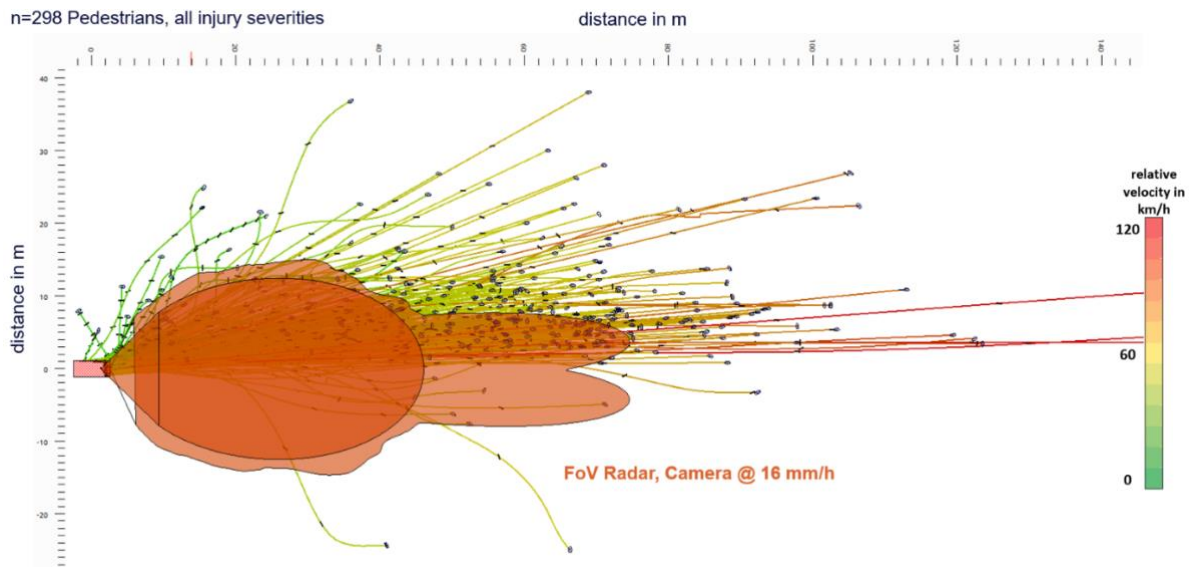


Figure 97: All cases of P-CLwoSO out of GIDAS in TRAVIS with Field of View (FoV) of Radar and Camera at 16 mm/h amount of rain.

Figure 98 shows the proportion of pedestrians in the P-CLwoSO scenario from $TTC = 5s$ to $TTC = 0s$ in the field of view of the sensor set (Figure 98 above), the radar (Figure 98 in the middle) and the camera (Figure 98 below) for 0 mm/h precipitation (blue), 16 mm/h precipitation (orange) and 66 mm/h precipitation (yellow) are indicated. There are differences between 1.6 s and 5 s TTC for detected pedestrians. As the TTC increases, the differences in detected pedestrians become larger. Up to a $TTC = 1.6 s$, 95% of the pedestrians are recognized. The remaining pedestrians above 95% represent special cases. A single case inspection revealed that these are pedestrians (sometimes drunk) who run into the side of the very slowly moving or stationary vehicle and injure themselves minimally. The trajectories of these pedestrians can be found to the left of the vehicle in Figure 99, all other pedestrians in front of the vehicle are recorded.



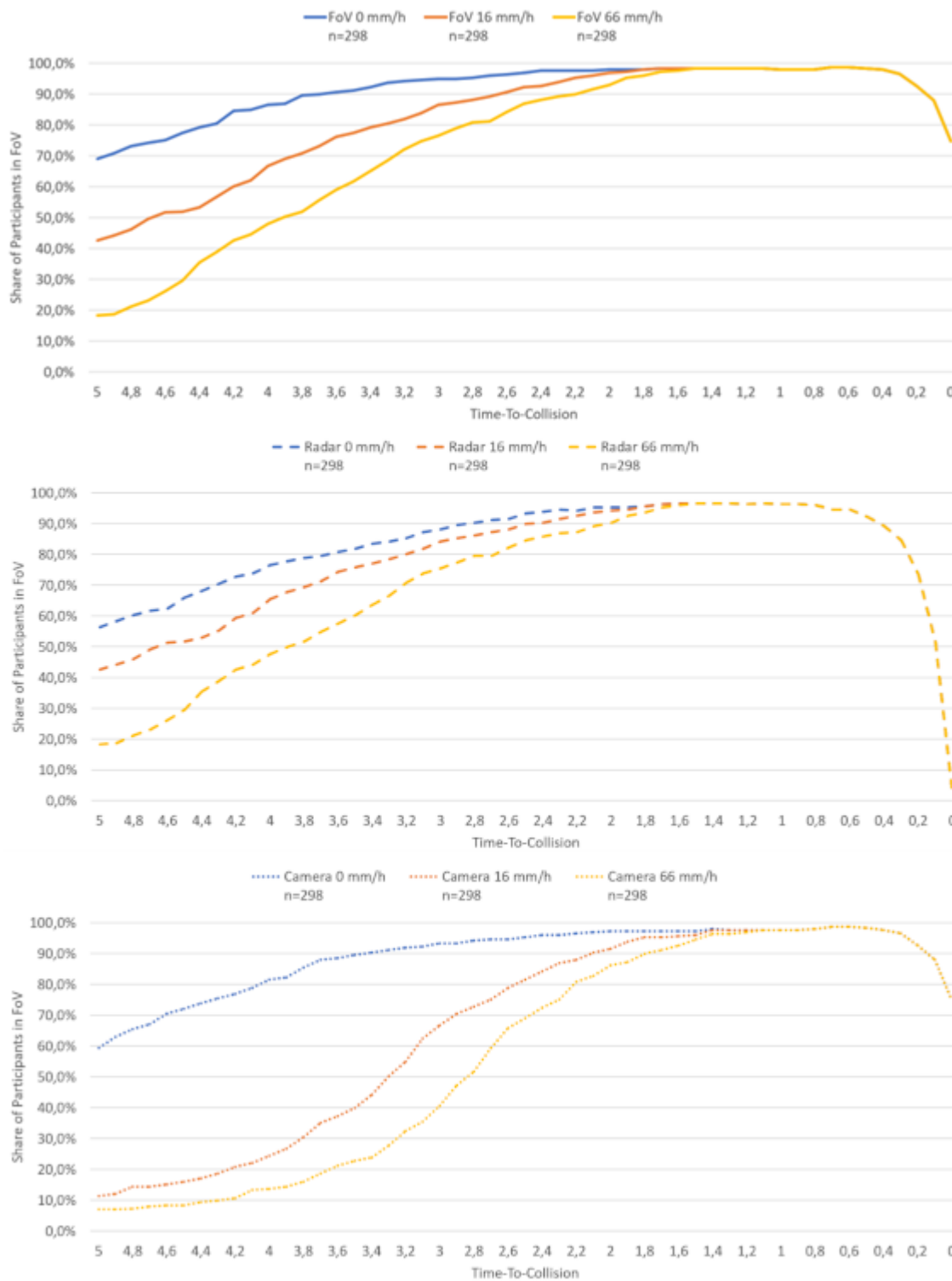


Figure 98: Proportion of Participants in FoV for Sensor Set, Radar or Camera for Scenario P-CLwoSO from TTC=5 s to TTC=0s.



Before the collision from $TTC=0.3s$ to $TTC=0s$, a sharp drop in the proportion of pedestrians can be seen in Figure 98. There are two reasons for this drop-in proportion:

1. The trajectories in the GIDAS PCM result from the movement of the centers of gravity of cars and pedestrians. The dimensions for the individual cases can be mapped according to reality using a bounding box. In the representation of all approach trajectories, however, a standard vehicle must be assumed for the bounding box and positioning of the sensors. In this case, the length is 5.00 m and the width is 2.20 m. As a result, depending on the dimensions of the vehicle in each case, the pedestrians move further into the bounding box of the standard vehicle and thus out of the detection range of the sensor out as displayed in Figure 99.
2. The drop at the radar begins before the portion at the camera starts to drop off. This is because the positioning of the radar in the area of the bumper and the positioning of the camera in the area of the windscreen were assumed. As a result, the radar is in front of the vehicle and the effect explained at point 1 occurs even with larger TTC.

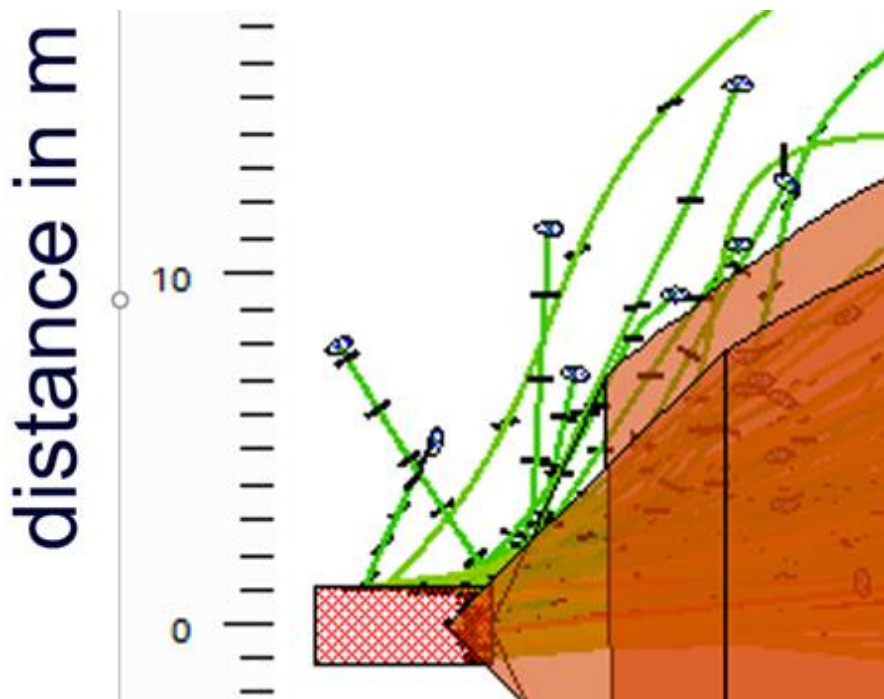


Figure 99: Detail of Passenger Car, Sensor set and Trajectories in TRAVIS.

Criticality of the situation over time based on data from the Traffic Accident Scenario Community of the Fraunhofer Institute for Transport and Infrastructure Systems

To determine the criticality of a driving situation, there is the data basis of the Traffic Accident Scenario Community (TASC) of the Fraunhofer Institute for Transport and Infrastructure Systems (IVI) (Pohle & Erbsmehl, 2021). This database contains natural driving data and accident data. Accident data is based on traffic accidents recorded by the police, which are processed the pre-crash phase of the accident and are also available in PCM format. It is thus possible to describe the pre-accident phase for many accidents and to calculate a TTC between the parties involved. Figure 100 (left) shows an example of a possible course of an accident with the P-CLwoSO scenario. Since the original case is an accident, the TTC drops to 0 s over time. This scenario is varied regarding the possible reaction of those involved to avoid the accident. If a possible reaction nevertheless leads to an accident, the TTC in the corresponding variation is also zero (see Figure 100 - right). However, if the attempt to avoid the accident is successful, then there is a minimum TTC for this variation. For each original case, a set of TTC is formed with the variations (Figure 100 - table on the right). An average minimum TTC is formed from the minimum TTC values for each accident.

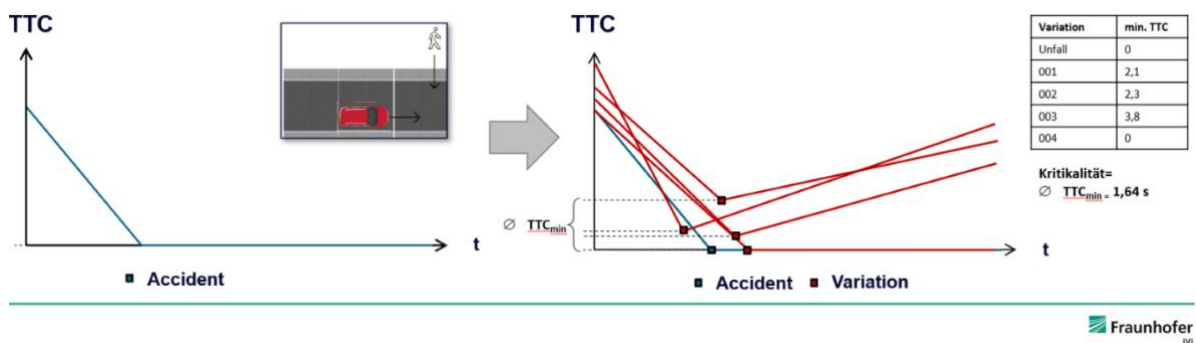


Figure 100: TTC of an accident and average minimum TTC of a maneuver.

The determined average minimum TTC can be used for a driving maneuver or summarized in a scenario and presented as a distribution as shown in Figure 101. The distribution of the minTTC can be divided into deciles and a criticality scale can be derived. Figure 101 on the right shows the violin diagram for the P-CLwoSO scenario based on n=295 cases. The distribution of the TTC shows that a large range of minimum TTC values from 0.5 s to 1.2 s can be found and that this scenario becomes critical in this time range. This shows that when accidents in this scenario are varied, the resulting critical situations reach low TTC values. Accordingly, this time range is also the field of action for safety functions, for which the pedestrians must also be recognized accordingly in this time range—plus any triggering times or reaction time for functions with a response request to the driver.



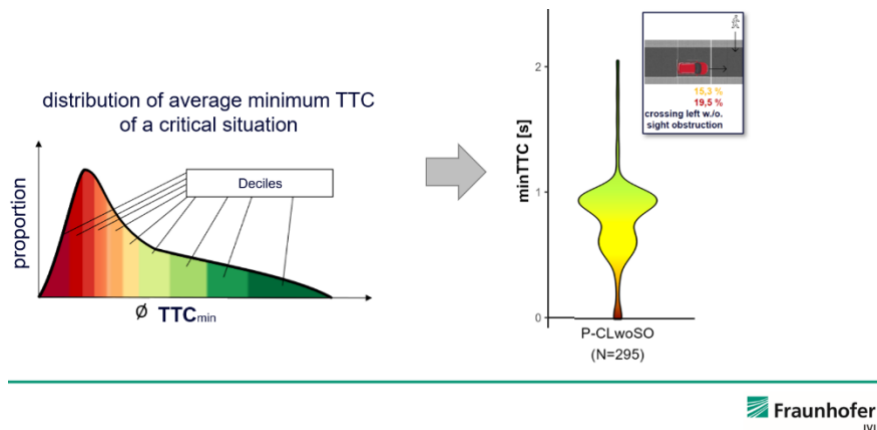


Figure 101: Distribution of average minimum TTC of a critical situation (left) and violin diagram for critical situation P-CLwoSO.

Result of Analysis of FoV in TRAVIS and TASC Data

As a result, the proportions of pedestrians detected in the P-CLwoSO scenario can be superimposed using the violin diagram from the analysis of the TASC data as given in Figure 102. The detection rates for the sensor set are very high for all levels of precipitation for the time range in which the respective minimum TTCs accumulate from the variation of the TASC cases. In this time range, a safety function has the option of avoiding the impending accident by intervening. This investigation shows the robustness of the sensor set with respect to precipitation amounts in the relevant time range of the selected scenario P-CLwoSO for the critical situation.

n=298 Pedestrians, all injury severities

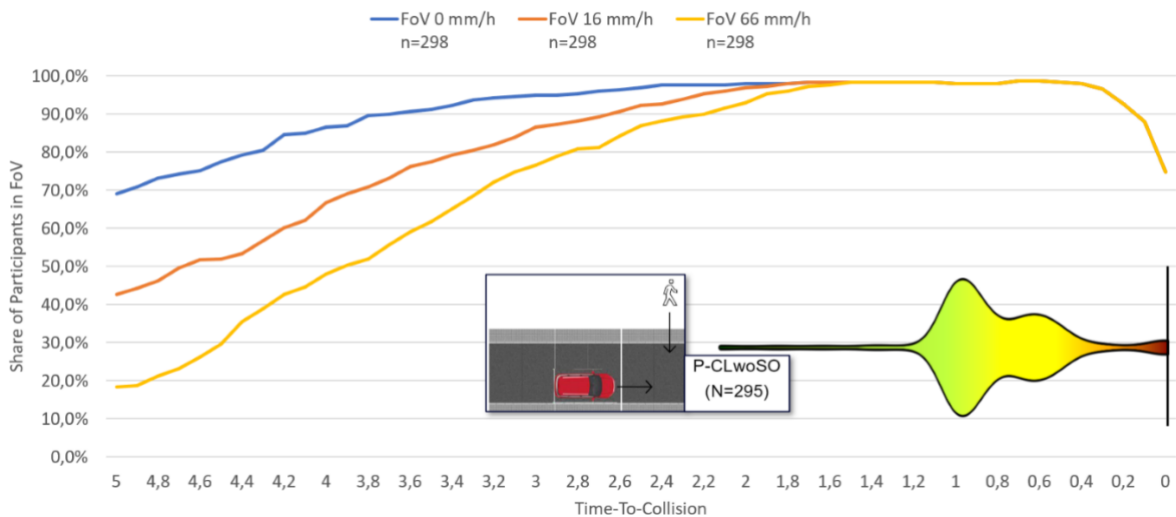


Figure 102: share of pedestrians in the FoV for different rain intensities and violin diagram of the min. TTC from accident variations.



7. Conclusions and next steps

The second phase of the Demo 3 development (subsequent to the initial phase reported in (SAFE-UP, Deliverable report D3.3, 2022)) focused on the final scenario selection for the simulative and physical testing of the developed active safety systems, the finalization of subsystem development and system integration into the demonstrator vehicle and the simulative assessment of adverse weather conditions on the intervention strategies employed by the Demo 3 system.

The determination of relevant scenarios for the Demo 3 scope has been finalized. The study results revealed only a limited avoidance share for the AES intervention for scenarios involving a frontal collision with a crossing pedestrian but a quite big avoidance share for scenarios involving a side collision. Similarly, scenarios involving frontal collisions are negligible for crossing bicyclists, whereas side collisions can be avoided in significant numbers. The study results will be used to determine the setup of the simulative safety benefit assessment of Work Package 5 and have already been used to define the scenarios of the physical testing campaign of the vehicle demonstrator that was executed at the IDIADA testing facilities. The deliverable D5.3 (SAFE-UP, Deliverable report D5.3, 2023) will report on both of these activities in the upcoming months.

The development of all major algorithms of the Demo 3 active safety function has been finalized with feature and performance updates of all subsystems. The subsystem integration and testing in the vehicle demonstrator has been completed during three integration workshops with all partners meeting at Bosch testing facilities and qualitative test results for the different subsystems are presented in this report. In a last development cycle the vehicle demonstrator will be improved by additional trajectory tracking controllers, that will also enable the demonstrator to mitigate to some extent the detrimental effects of unintended driver reactions to an emergency situation. A quantitative evaluation of both the whole system and the subsystems performance will follow in the deliverable report D3.8 (SAFE-UP, Deliverable report D3.8, 2023). The overall estimation of the safety benefit offered by the Demo 3 functionality based on both physical and simulative testing will be presented in the deliverable reports D5.3 (SAFE-UP, Deliverable report D5.3, 2023) and D5.6 (SAFE-UP, Deliverable report D5.6, 2023) of Work Package 5.

In an extensive simulation study, the effects of adverse weather conditions on the Demo 3 active safety system have been estimated. Here the analysis of real-world accident data was combined with perception models derived from measurements of the vehicle demonstrators sensor characteristics analyzing the detrimental effects of rainfall to the Demo 3 intervention strategies.



References

- Ackermann, C., Isermann, R., Min, S., & Kim, C. (2014). Design of a decision maker for an evasive or braking maneuver for collision avoidance. In M. Bargende, H. Reuss, & J. Wiedemann (Red.), *14. Internationales Stuttgarter Symposium*.
- C. van der Ploeg, R. S. (2022). Long Horizon Risk-Averse Motion Planning: A Model-Predictive Approach. *2022 IEEE 25th International Conference on Intelligent Transportation Systems (ITSC)*, (pp. 1141-1148). Macau.
- EuroNCAP. (2022). *EuroNCAP - Test protocol - AEB/LSS VRU systems - Implementation 2023*. Opgehaald van <https://cdn.euroncap.com/media/67888/euro-ncap-aeb-lss-vru-test-protocol-v41.pdf>
- Fliess, M., Lévine, J., Martin, P., & Rouchon, P. (1995). Flatness and defect of non-linear systems: introductory theory and examples. *International Journal of Control*, *61*, 1327-1361.
- Huber, P. J. (1964). Robust Estimation of a Location Parameter. *The Annals of Mathematical Statistics*, *35*(1), 73-101.
- Joos, S., Bitzer, M., Karrelmeyer, R., & Graichen, K. (2019). Constrained online trajectory planning for nonlinear flat SISO systems using a switched state variable filter. *Automatica*, *110*.
- Kühnel, W., & Hunt, B. (2006). *Differential Geometry: Curves - Surfaces - Manifolds* (Second ed., Vol. 16). American Mathematical Society - Student Mathematical Library.
- Laurène Clausmann, M. R. (2020). A Review of Motion Planning for Highway Autonomous Driving. *IEEE Transactions on Intelligent Transportation Systems*, *21*(5), 1826-1248.
- Löffler, C., Gloger, T. F., & Joos, S. (to be published). Synthesis and application of constrained flatness-based real-time trajectory planning for autonomous emergency steering.
- Muñoz Sánchez, M., Elfring, J., Silvas, E., & van de Molengraft, R. (2022). Scenario-based Evaluation of Prediction Models for Automated Vehicles. *IEEE Intelligent Transportation Systems Conference*.
- Neukum, A., & Krüger, H.-P. (2003). Fahrerreaktionen bei Lenksystemstörungen - Untersuchungsmethodik und Bewertungskriterien. *VDI-Berichte*.
- Neukum, A., Paulig, J., Frömmig, L., & Henze, R. (2010). Untersuchung zur Wahrnehmung von Lenkmomenten bei PKW. *FAT-Schriftenreihe*.
- Park, J., Jeong, H., Jang, I. G., & Hwang, S.-H. (2015). Torque Distribution Algorithm for an Independently Driven Electric Vehicle Using a Fuzzy Control Method. *Energies*, *8*, 8537-8561.



- R. Smit, C. v. (2022). Informed sampling-based trajectory planner for automated driving in dynamic urban environments. *2022 IEEE 25th International Conference on Intelligent Transportation Systems (ITSC)*, (pp. 1690-1697). Macau.
- S. I. (2018). Taxonomy and Definitions for Terms Related to Driving Automation Systems for On-Road Motor Vehicles. Opgeroepen op 2020, van <https://www.synopsys.com/automotive/autonomous-driving-levels.html>
- SAFE-UP. (2021). *Deliverable report D2.6*.
- SAFE-UP. (2021). *Deliverable report D3.1*.
- SAFE-UP. (2022). *Deliverable report D3.3*.
- SAFE-UP. (2022). *Deliverable report D3.5*.
- SAFE-UP. (2022). *Deliverable report D3.9*.
- SAFE-UP. (2022). *Deliverable report D5.8*.
- SAFE-UP. (2023). *Deliverable report D3.8*.
- SAFE-UP. (2023). *Deliverable report D5.3*.
- SAFE-UP. (2023). *Deliverable report D5.6*.
- Schneider, N. (2018). Einfluss der haptischen Rückmeldung am Lenkrad auf das Fahrerverhalten bei automatischen Eingriffen in die Querführung. *Dissertation*. Universität Würzburg, Fakultät für Humanwissenschaften.
- Schöllner, C., Aravantinos, V., Lay, F., & Knoll, A. (2020). What the Constant Velocity Model Can Teach Us About Pedestrian Motion Prediction. *IEEE Robotics and Automation Letters*, 5(2), 1696-1703.
- Schramm, D., Hiller, M., & Bardini, R. (2018). *Vehicle Dynamics* (Second ed.). Berlin, Heidelberg: Springer.
- Schubert, A., Liers, H., & Petzold, M. (2016). The GIDAS pre-crash-matrix 2016. Innovations for standardized pre-crash-scenarios on the basis of the VUFO simulation model VAST. ESAR.
- Tolksdorf, L., Tejada, A., van de Wouw, N., & Birkner, C. (to be published). *Risk in Stochastic and Robust Predictive Path-Following Control for Vehicular Motion Planning*.
- UNECE. (2018). Regulation No 79 of the Economic Commission for Europe of the United Nations (UN/ECE) — Uniform provisions concerning the approval of vehicles with regard to steering equipment [2018/1947]. *UN/ECE Regulation*. Opgehaald van <http://data.europa.eu/eli/reg/2018/1947/oj>
- Wang, J., Wu, J., Zheng, X., Ni, D., & Li, K. (2016). Driving-safety field theory modeling and its application in pre-collision warning system. *Transportation Research Part C: Emerging Technologies*, 72, 306-324. doi:10.1016/j.trc.2016.10.003



- Wilson, B., Qi, W., Agrawal, T., Lambert, J., Singh, J., Khandelwal, S., . . . Hays, J. (2021). Argoverse 2: Next Generation Datasets for Self-Driving Perception and Forecasting. *Thirty-fifth Conference on Neural Information Processing Systems Datasets and Benchmarks Track*.
- Y. Li, Z. L. (2014). Asymptotically optimal sampling-based kinodynamic planning. *The Int. Journal of Robotics Research*.

